# AN ULTRASONIC INSTRUMENTATION SYSTEM FOR THE STUDY OF VAPOUR BUBBLE FORMATION AND COLLAPSE IN SODIUM

by

MEHDI HASSAN-KAZEMEINI

Submitted for the Degree of Doctor of Philosophy
at
The University of Aston in Birmingham
June 1976

SUMMARY

An ultrasonic pulse-echo system has been developed for the study of the rapid growth and collapse of a single vapour bubble in a sodium pool under superheating and subcooling conditions up to 900°C. It is also capable of measuring the liquid level and detecting bulk boiling.

The system controls the sequential operation of a cavitation device, which initiates bubble growth at a known site within the liquid body, and a specially-designed high-speed valve, which produces a high-pressure pulse to collapse the bubble.

The ultrasound source is a pulse-excited 5 MHz piezoelectric transducer operating at a high p.r.f.; rapid electronic processing of the change in transit time of the bubble echoes follows the bubble growth.

The transducer is coupled to the containment vessel through a steel diaphragm and a cooled liquid-filled tube; the former is part of the wall of the vessel and the latter limits the upper working temperature of the transducer to 280°C.

Experiments with Woods metal at 400°C and liquid tin at 900°C encountered all the high-temperature problems anticipated with the sodium pool, and revealed that, provided the cooling tube is vertical, the controlled temperature gradient within it does not degrade the echo signal; distortion of the pulses by the diaphragm was avoided by choosing optimum thicknesses of odd multiples of the quarter wavelength, and by using a suitably-shaped excitation pulse.

The accuracy of bubble size measurement was verified by direct visual observation of air bubbles in a water-filled chamber identical to the sodium pool. Using high-speed ciné photography, the ultrasonic output was simultaneously superimposed on the film for direct comparison. The

results revealed that the system can give at least five observations of the bubble in 1 msec.

A sodium pool has been built at A.E.R.E. Harwell. Specifications based on the results of the experiments described here have been applied to the pool.

## ACKNOWLEDGEMENTS

I wish to thank my supervisor, Mr A.E. Noble for his guidance and encouragement throughout the course of work. I also thank Dr J.F.W. Bell, Reader, for the help he has given me and for the enthusiasm he has shown in the project. Thanks are due, too, to Professor Flood, Head of Department of Electrical Engineering, for providing the facilities necessary for the early stages of my research.

I am very grateful to the United Kingdom Atomic Energy Authority for allowing me to carry out the bulk of my work at the Atomic Energy Research Establishment, Harwell. Special thanks are due to Dr P. Hawtin and Mr J.C. Ralph of the Chemical Engineering Division for their professional help and personal encouragement. Finally, I wish to thank the laboratory staff for their help.

CONTENTS

# CHAPTER 1

## INTRODUCTION

Investigation into the boiling behaviour of liquid metals has been intensified with the increasing concern for fast reactor safety. The sodium coolant in a fast reactor is intended to sustain temperatures only as high as 600°C to 700°C ie a good 200°C below its boiling point at the prevailing pressure. It is realised, however, that hot-spots could occur where local boiling commences, and the resulting rapid vapour bubble growth and collapse could generate transient stresses, possibly causing damage to the reactor core assembly[1,2]. In order to approach the problem with more understanding, knowledge of the growth and collapse rates of bubbles under a range of physical conditions is essential.

Theories about single bubble dynamics in liquids have been put forward in the past; particular attention has been paid to a spherical vapour bubble in an infinite sea of liquid[3, 4, 5, 6, 7, 8, 9, 10]. No experimental results have been obtained in a mass of sodium due to the high temperature involved and the impossibility of visual observation. Any conclusions reached were the results of experiments in water using high-speed cine photography[7].

In establishing a programme of research into direct measurement with sodium, it has been necessary to develop a technique capable of measuring the rapid change in the size of a spherical vapour bubble initiated at a known position in a bulk of liquid sodium at 900°C. It has thus also been necessary to develop a system to control the nucleation and collapse of the bubble.

In the past, an X-ray technique has been used for the measurement of void dynamics in a narrow tube[11]. Considerable expense and difficulties, however, would be involved in developing the method for a vessel as large as the sodium pool. Neither is the use of electric resistance probes[13], developed for void detection in liquid metals, an efficient technique for the measurement required here, due to the slow response speed of the probes and to the physical interference with the bubble interface.

There is a real possibility, however, of detecting a vapour bubble in liquid sodium by ultrasonic means, since the bubble acts as a good reflector of ultrasound; this is because of the large acoustic impedance mismatch at the bubble boundary. Transmission of the ultrasound into the hot liquid sodium, however, gives rise to many difficulties. It must also be remembered that, since change in bubble radius (from 1mm to 10mm) has to be detected within a few milliseconds, the technique chosen must have a good resolution and response time.

Among the large number of ultrasonic techniques for detection of objects in liquids, the pulse echo system comes closest to satisfying the above requirements. Information about the bubble size can be obtained from the amplitude, the transit time of the echo from the bubble interface, and the shadow behind the bubble. The transit time of the echo has been used in the past[4] for measurement of the rapid change in the thickness of a vapour layer at a flat heated surface in water.

The ultrasonic pulse echo system developed for the sodium pool consists of transmitting a series of pulses, with a high pulse repetition frequency, into the liquid, receiving the echoes from the bubble interface, and measuring the change in transit time of the bubble echoes. Several problems associated with the high temperature must first be solved.

An adequate resolution for detecting small bubbles can be achieved by

employing a piezoelectric transducer sufficiently sensitive in the MHz range. The piezoelectric materials available are subject to chemical attack by liquid metals, and some means of isolation is necessary. The transducer is therefore protected from the corrosive liquid sodium by a stainless steel diaphragm. It is shown in Chapter 4 that the diaphragm has an adverse effect on the amplitude and the duration of the echo pulse passing through it, thereby reducing the resolution of the entire system. A further consequence of employing a diaphragm is that the liquid may not wet the diaphragm completely, due to metal oxide or impurities at the diaphragm surface. Considerable attention has been given to these problems in Chapters 4 and 7, and solutions have been found.

Since piezoelectric materials cannot be used at temperatures higher than the Curie temperature, it is also necessary to position the transducer at the end of a cooled temperature buffer. In the past, solid rods and wires have been used in liquid metals as cooled transmission lines for sound pulses[16, 17, 18] and as waveguides in the detection of boiling noise[19]. For the pulse echo technique required here, however, the need to transmit high frequency pulses at high sampling rates, and to detect very small echoes from small spherical bubbles against the background noise, excludes the possibility of using a solid rod as a temperature buffer. As will be shown in Chapters 2 and 7, a suitable buffer is a liquid-filled tube with a controlled and stable temperature gradient from the hot bubble region to the relatively cool transducer region, through which sound pulses are readily transmitted, although some effects from temperature fluctuation are expected.

Experiments have been carried out in Woods metal at 400°C and liquid tin at 900°C (Chapter 7) in order to investigate the problems associated with this type of cooled transmission line, and to discover the most satisfactory arrangement for a sodium pool. It is worth noting that the

cooling tube has also been used for sound velocity measurement in Woods metal up to 400°C and tin up to 900°C (Chapter 7).

The system of cooling and protecting the transducer enables tests at high temperature in liquid metals to be carried out quite easily.

# CHAPTER 2

# VAPOUR BUBBLE SIZE MEASUREMENT IN SODIUM

## 2.1 INTRODUCTION

Consideration of safety aspects of liquid metal cooled fast reactors involves the study of the boiling behaviour of sodium. Experimental evidence[17] indicates that liquid sodium, in common with many other liquids, has the ability, in some circumstances, to superheat well above the liquid-vapour saturation line defined by thermodynamic equilibrium. In a superheated liquid, boiling commences when vapour bubbles begin to grow at nucleation sites such as very small gas bubbles in the bulk liquid or vapour cavities trapped at the solid surfaces. Superheat in a volume of liquid is a function of the radius of the nucleation site and the ambient pressure[9] In Table 2.1 Judd compares sodium with water.

TABLE 2.1: Superheat and Critical Bubble Radius (Boiling at 1.7 atm.)

| Critical bubble radius (cm) | | $10^{-1}$ | $10^{-2}$ | $10^{-3}$ | $10^{-4}$ | $10^{-5}$ | $10^{-6}$ |
|---|---|---|---|---|---|---|---|
| Superheat (°C) | Sodium | 0.15 | 1.5 | 14 | 99 | 352 | 730 |
| | Water | 0.02 | 0.2 | 2.0 | 15 | 65 | 146 |

It is expected that the events following nucleation of a vapour bubble in sodium will be different from those in non-metallic systems[10]. In the case of sodium the formation of the first bubble deactivates the surrounding nucleation sites, and so boiling occurs with a few large bubbles, whereas many small bubbles occur in water[18]. It has been shown that a single vapour bubble growing in a boiling sodium system empties the coolant channel by ejecting the liquid above it. The bubble also acts as a plug,

preventing any further liquid from entering the channel. In a reactor system, if the vapour bubble reaches regions in which the temperature is less than the local saturation temperature (sub-cooling), the vapour bubble pressure inside the bubble decreases, causing it to collapse. A high pressure pulse of short duration results which may cause local damage.

Over the past twenty years, a number of authors[3,4,5,6,7,8] have investigated the growth and collapse mechanism of a vapour bubble, using, for the most part, a spherical bubble in an infinite sea of liquid. The equation of motion of an empty spherical cavity has been solved analytically (Lord Rayleigh, 1917 ) by considering the liquid pressure and the surface tension forces at the cavity interface. In the case of a vapour bubble the dynamics are also affected by the vapour pressure inside the bubble. The vapour pressure is controlled by heat transfer from or to the bulk of the surrounding liquid. This leads to a complex thermo-hydrodynamic problem. The problem has been studied both theoretically and experimentally in water, and possible solutions to the combined equations of motion and heat transfer have been sought.

Predictions for sodium have been made by some authors[7,9,10] who have again considered the growth of a single spherical bubble in an infinite sea. Board[7] has compared his predictions with those of others; this comparison is shown in Figs. 2.1a and b which give the variation of the bubble radius with time for various superheats at 1.7 atm. It can be seen that at higher degrees of superheat the heat transfer from the surrounding liquid to the volume of the bubble takes place more easily and thus the bubble grows to a larger size. Donne and Ferranti (1975)[10] have obtained theoretical results for sodium with superheat up to 380°C, using a method to integrate the differential equations by numerical computation. Fig. 2.22 shows the results at 1 atm. It relates the variation of R and $\frac{dR}{dt}$ (the radius and the growth rate of the expanding bubble) to time for nucleation

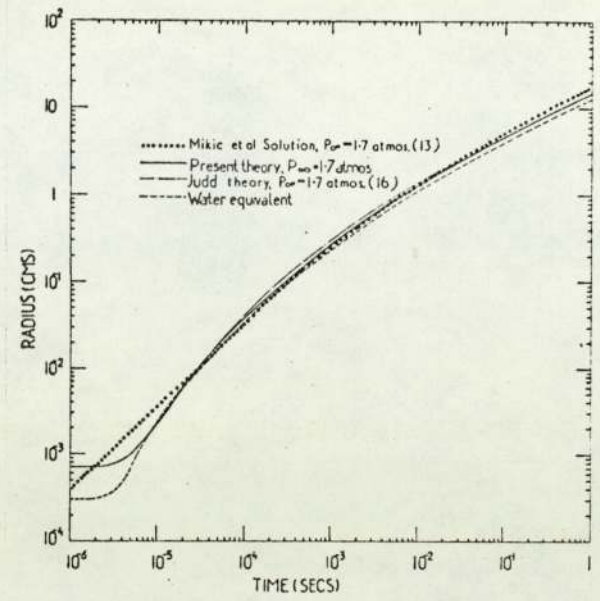


(a) Sodium vapour bubble growth, 20°C superheat

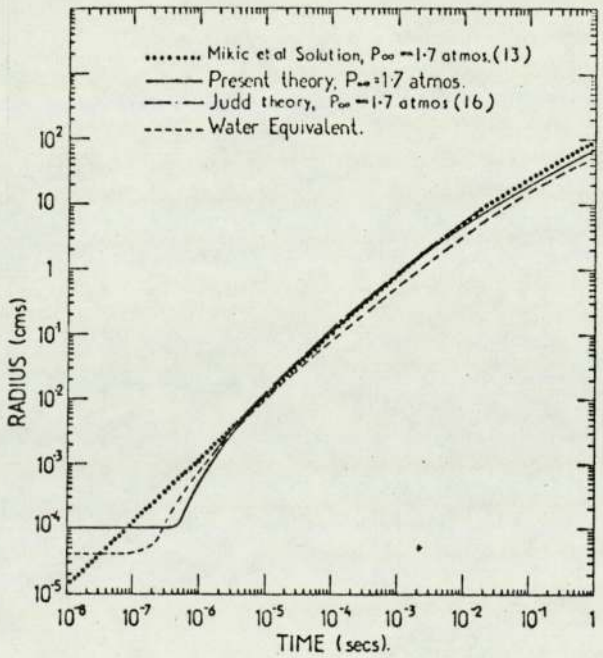


(b) Sodium vapour bubble growth, 100°C superheat

Fig. 2.1 Theoretical predictions for growth rate of a spherical vapour bubble in liquid sodium. (Copied from Figs. 2 and 3 of Board[7]).

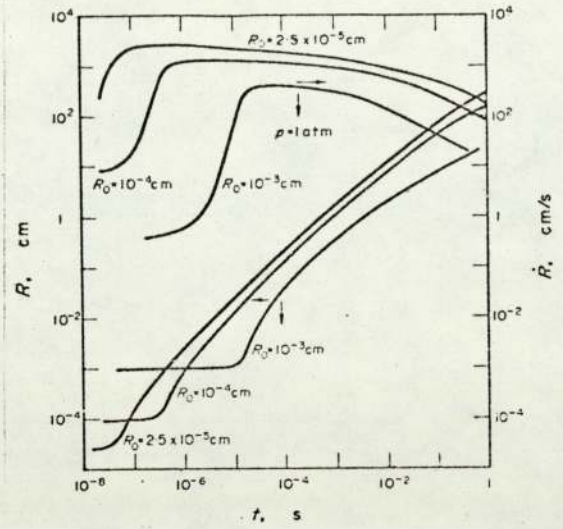


(a) R, $\frac{dR}{dt}$ versus time for 1 atm pressure, and critical radii of 2.5 x $10^{-5}$, $10^{-4}$, $10^{-3}$cm.

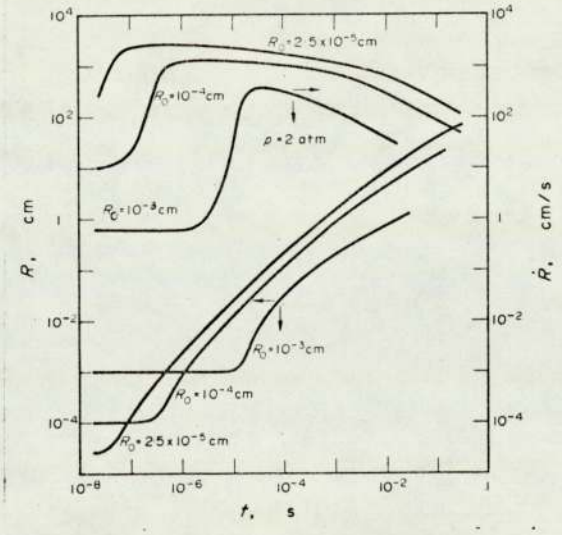


(b) R, $\frac{dR}{dt}$ versus time for 2 atm pressure and critical radii of 2.5 x $10^{-5}$, $10^{-4}$, $10^{-3}$cm.

Fig. 2.2. Theoretical predictions for growth rate of a spherical vapour bubble in liquid sodium. (Copied from Figs. 5 and 7 of Donne and Ferranti[10] 1975).

sites with radii of $2.5 \times 10^{-5}$cm, $10^{-4}$cm and $10^{-3}$cm. In the presence of large degrees of superheat, $\frac{dR}{dt}$ remains relatively constant for quite a long period of time.

Experimental and theoretical results have also been achieved for spherical bubble collapse. Tests were actually carried out in water, and again predictions have been made for sodium[19,20]. The following table shows the approximate collapse time as a function of subcooling, as predicted by Judd[21] for an initial radius $R_o$ = .1cm.

Table 2.2

| Subcooling (°C) | Collapse time (msec) |
|---|---|
| 10 | 70 |
| 20 | 20 |
| 50 | 2.5 |
| 100 | 1.2 |

However, in order to verify theoretical predictions, direct measurement of vapour bubble growth and collapse in liquid sodium is required.

## 2.2 BUBBLE NUCLEATION AND COLLAPSE IN SODIUM POOL

In order to study the dynamics of a single vapour bubble in liquid sodium, a mechanism is required to initiate a single bubble at a known position within a volume of sodium. Since the measurements should not be obscured by spurious bubble formation, the containing vessel and the superheated sodium are required to be free from active nucleation sites, which implies that the vessel walls should be smooth and that purified sodium should be used.

The mechanism should then initiate, when required, a cavity of critical size somewhere near the centre of the vessel. The methods available for non-metal liquids, such as production of an underwater spark[22], discharging

a capacitor across a fine resistance wire[7] and optical cavitation by focusing giant pulses of a ruby laser[23], are unsuitable for liquid metals.

A cavitation method for nucleation of a single vapour bubble, suitable for a sodium pool, has been introduced by Ralph[24]. The nucleation device consists of a coaxial rod and tube, the rod protruding a small amount from the tube and the whole immersed in the liquid pool. Rapid withdrawal of the rod into the tube creates a local cavity at the end of the tube, which is then the nucleation site. The device has been tested in superheated water and has proved capable of initiating a spherical vapour bubble (Fig. 2.3). The bubble growth is arrested at a predetermined size by a sudden release of a small volume of high pressure inert gas into the gas space of the pool, thus changing the conditions in the liquid from superheat to subcooling. The vapour bubble in the subcooled liquid then collapses at a rate which depends on the degree of subcooling.

For direct measurement of vapour bubble growth and collapse rates in the sodium pool it was considered that the ultrasonic pulse echo system must be capable of giving a measuring rate of at least 5 observations per millisecond.

## 2.3 ULTRASONIC TECHNIQUE

Bubble size can be determined by the pulse-echo technique more conveniently if the bubble is in the geometrical region (ie when the bubble diameter d is much larger than the incident wavelength $\lambda$, $d>2.6\lambda$)[25]. For small bubbles ranging from 1mm in liquid sodium, for example, the corresponding minimum frequency is 5MHz. However, there is a limit to the use of higher frequencies as the bulk attenuation of a liquid increases rapidly with frequency[26]. At the 5MHz frequency chosen the attenuation coefficient in sodium[27] is of the order of $3.75 \times 10^{-3}$ neper/cm at 250°C, which is lower

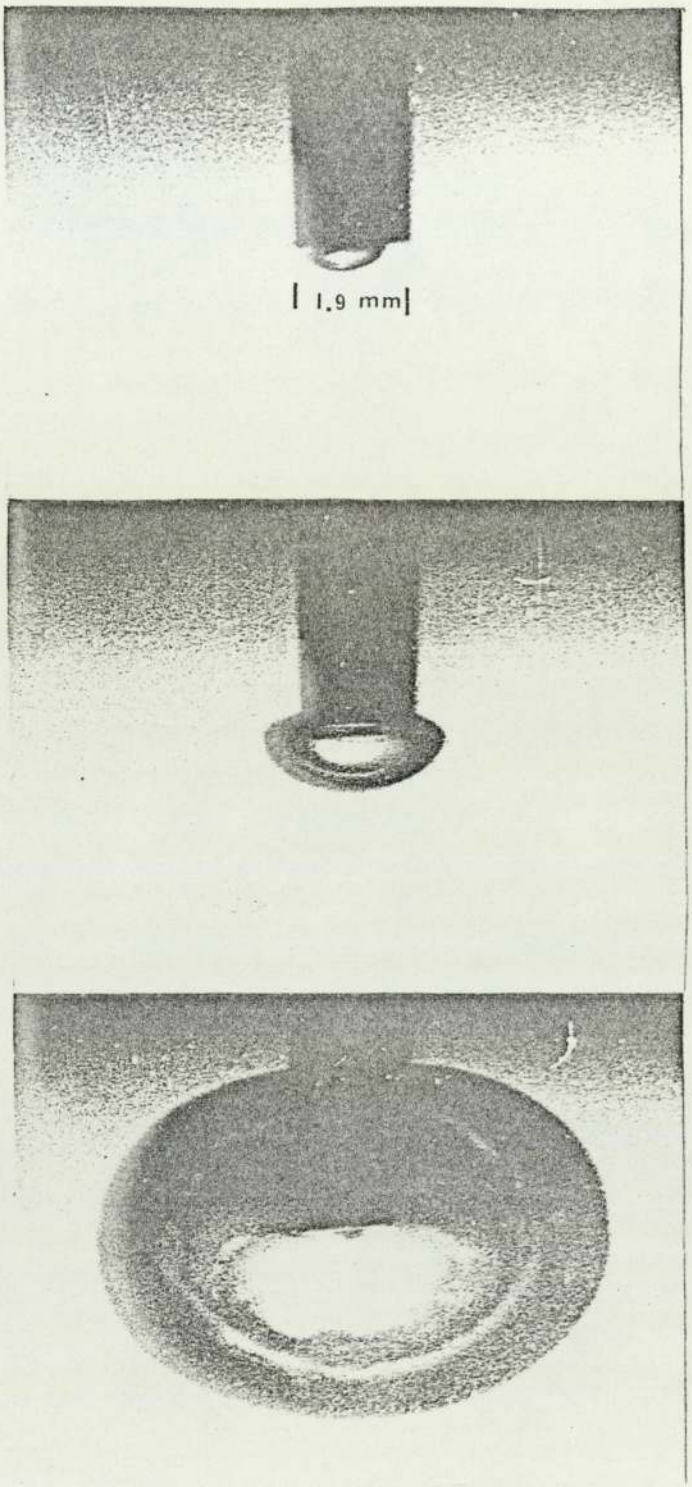


At 0.5 msec from nucleation.

At 2 msec from nucleation.

At 16 msec from nucleation.

Fig. 2.3. Vapour bubble nucleation by rod withdrawal technique in water at 5°C superheat at 0.3 atm (Ralph[24]). (Non-spherical appearance due to optical distortion through circular containment walls).

than that in pure water[51] ($5.25 \times 10^{-3}$ neper/cm).

Fig. 2.4 shows the basic arrangement of the pulse-echo system employed. A disc transducer, acting as both transmitter and receiver, generates a series of ultrasonic pulses, each consisting of a small number of waves corresponding to a predominant frequency of 5MHz (Fig. 2.4a). These pulses are propagated into the liquid towards the bubble nucleation site. The site is the end face of the cavitation rod, which is at a distance L from the transducer and fixed along the axis of the sound beam.

Theoretical results, using a piston source model for the transducer (Chapter 3), indicate that the incident intensity across the beam is not uniform; it falls away from the axis. However, if the bubble is spherical and positioned on the beam axis at large distances, a relationship can be found between the echo signal amplitude and the bubble size. The transit time of the bubble echo also enables the position of the front phase boundary of the bubble to be determined; an estimate of bubble size can be made by reference to the nucleation rod. Another possible way is to measure the reduction of the echo amplitude from a large, flat target situated some distance behind the bubble; this is dependent on the size of the bubble shadow, and is a measure of the bubble cross-sectional area during growth.

The suitability of the three proposed methods based on (i) the amplitude of the bubble echo (ii) the amplitude of the back target echo (iii) the time delay of the bubble echo, for measuring the size of a growing bubble, is discussed below.

### 2.3.1 Echo Amplitude Method

When a spherical bubble is situated on the beam axis at a large distance the incident energy is scattered in all directions by the bubble face. Theoretical predictions verified by experiments (Chapter 3) indicate that the

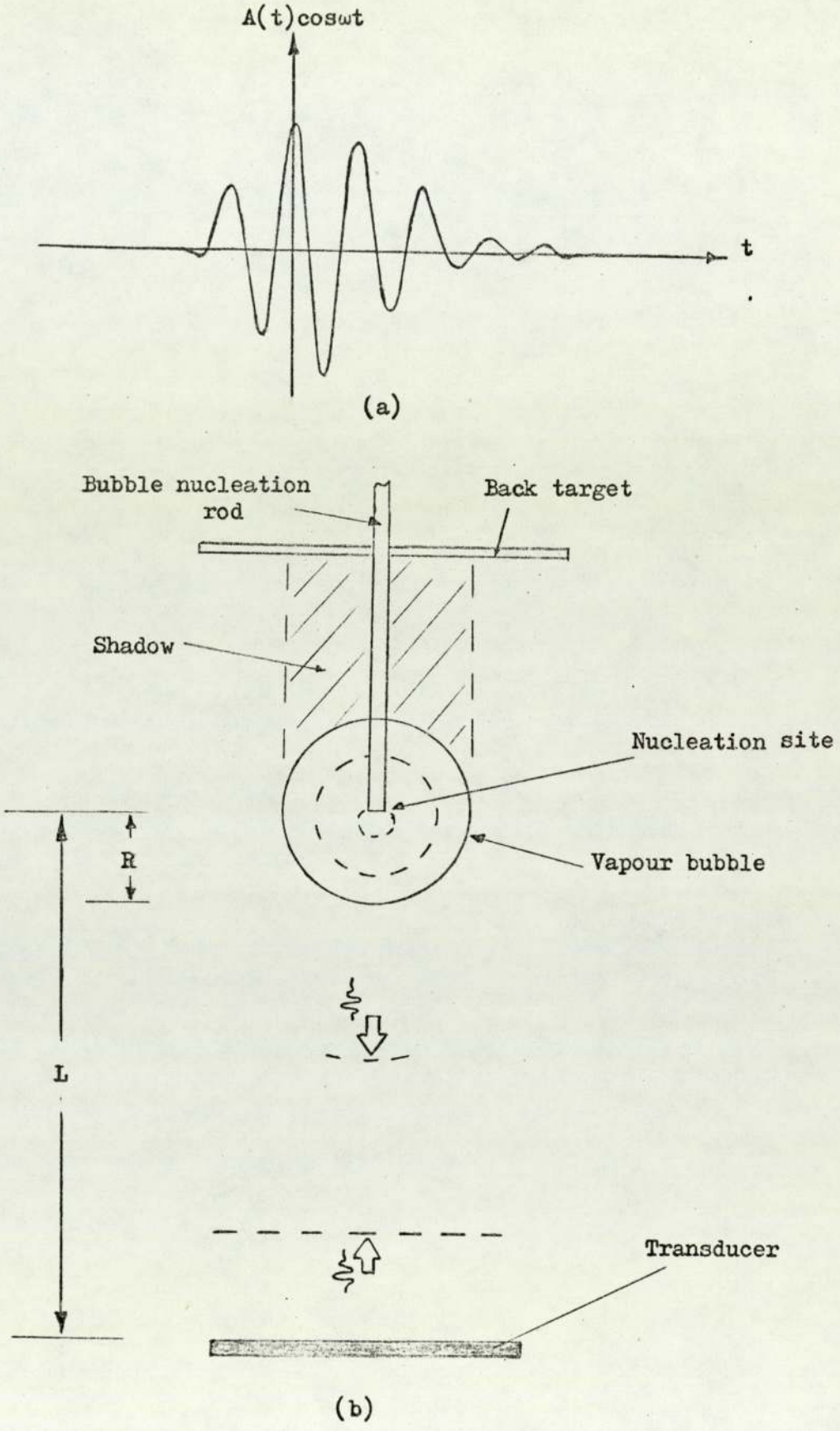


Fig. 2.4. Basic principles of the pulse-echo system for bubble size measurement.

echo received back by the transducer is that reflected from only a small area of the bubble surface at the centre of the beam. This area is a function of bubble radius (or the curvature of the bubble at the centre of the beam) and the incident wavelength.

However, the echo amplitude is proportional to the bubble radius even if the bubble cross-sectional area exceeds that of the beam. For example, for a bubble at 30cm distance from a 5MHz transducer of 10mm diameter, the linear relationship extends to a radius as large as 10cm. Thus the difference between the amplitudes of any two successive echoes is proportional to the change in the bubble size during each time period.

For calibration of the system a reference echo amplitude in sodium is required. The flat end of the nucleation rod (Fig. 2.4) can be used as a reference target and the echo amplitude from the spherical bubble estimated. The approximated theoretical relationship between a flat circular target and a spherical target (Chapter 3) in the geometrical region for the same received echo amplitude is

$$T^2 = a' \frac{\lambda}{2\pi}$$

where T is the radius of the circular target, a' the sphere radius and $\lambda$ is the incident wavelength calculated from the average frequency of the pulse.

Measuring the size of a fast-growing bubble by the echo amplitude method, however, is quite difficult: (i) it is necessary to design an electronic system capable of sampling the amplitude of the successive echoes during rapid changes in bubble size (ii) the accuracy of the system relies on the reference amplitude and the assumption that the bubble shape remains perfectly spherical during growth and collapse.

### 2.3.2 Back Target Echo Method

This is based on measuring the change in amplitude of the successive echoes from a flat target behind the bubble.

As is shown in Fig. 2.4, before bubble growth commencement, two echoes are received: one from the rod end and the other from the back target. At the initial stage of growth no change in the echo amplitude from the back target is detected until the bubble cross-sectional area exceeds the rod end area. It is worth noting that, at this stage, the reduction in the echo amplitude from the rod end itself is detectable and could be used for measurement of this initial growth.

When the bubble becomes larger than the rod end the rod echo disappears and reduction in the echo amplitude of the back target becomes a measure of the bubble size.

In the geometrical region (where the bubble is much larger than the incident wave length) the total energy scattered by the bubble face is proportional to the bubble cross-section if the incident intensity is uniform. However, in the sound field of a disc transducer the intensity in the far field decreases off axis. Thus the echo amplitude from the back target does not decrease linearly with the bubble size, although the system is still highly sensitive for small bubbles.

Using the rod end as a reference it may be possible to obtain, using the ideal piston theory for the transducer, an approximate calibration curve. But since the diameter of the transducer chosen for the sodium pool is 10mm the system is not capable of measuring the diameter of large bubbles. However, it will be shown that the system is valuable for determining small moving particles and bubbles in liquids.

### 2.3.3 Echo Delay Method

This method is based on the measurement of the change in transit time

between each two successive echoes reflected from the moving interface of the bubble. With the aid of Fig. 2.4 the technique is described as follows.

Before bubble growth commences each pulse reflected from the nucleation site (the rod end) returns after a time T to the transducer which now acts as a receiver. Once the return time T has been measured, of course, it is possible to calculate with a high degree of accuracy the distance L, provided that the sound velocity c of the liquid is known:

$$L = \frac{c}{2} T$$

The simple linear relationship between distance and echo delay is the basis of the method for measuring the bubble size.

As soon as a small vapour bubble appears around the nucleation site, the echo pulse received is no longer from the end but from the bubble interface. Observations have shown[24] that the centre of the bubble remains at the end of the rod and one may therefore consider this as the change in radius. If the bubble grows to radius R, the transit time will reduce from T to $(T-\Delta t)$ where $\Delta t = \frac{2R}{c}$. The change in the return time of the echo from the bubble interface is therefore proportional to the change in the bubble radius. It must be noted that at the initial stage of growth the bubble is not quite spherical due to the interference of the rod and thus the change in $\Delta t$ can only be related to an estimated average radius. The value of $\Delta t$ can be measured accurately by means of an electronic system.

Due to the simple linear relationship between $\Delta t$ and R, calibration of the system is relatively simple. The conversion factor between the bubble radius and the change in the transit time is 0.75 mm/μsec in water at 20°C and 1.05mm/μsec in sodium at 900°C. The velocity of sound in most liquids varies with temperature. Figs. 2.5 and 2.6 show the variation of

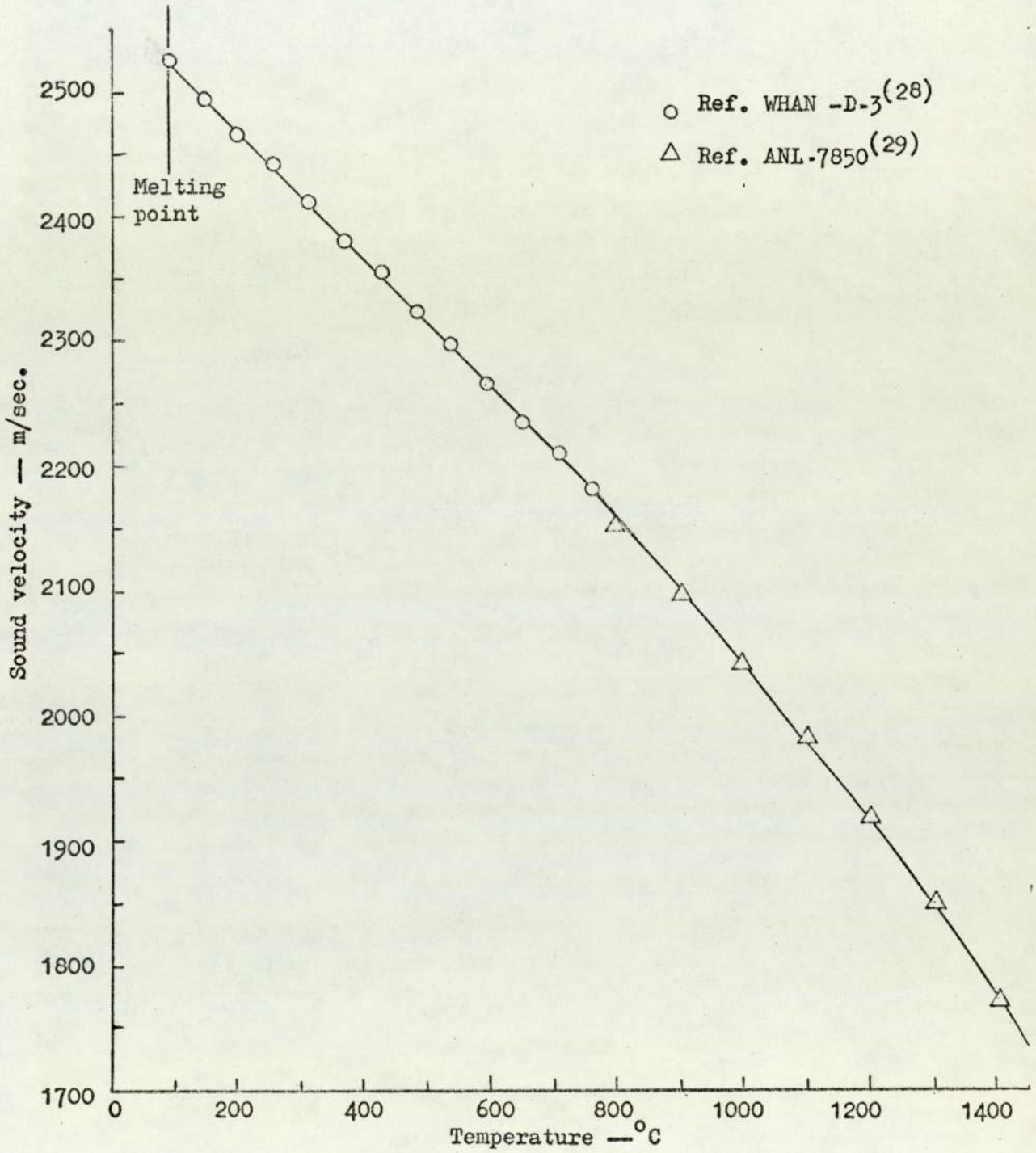


Fig. 2.5. Variation of sound velocity with temperature in liquid sodium.

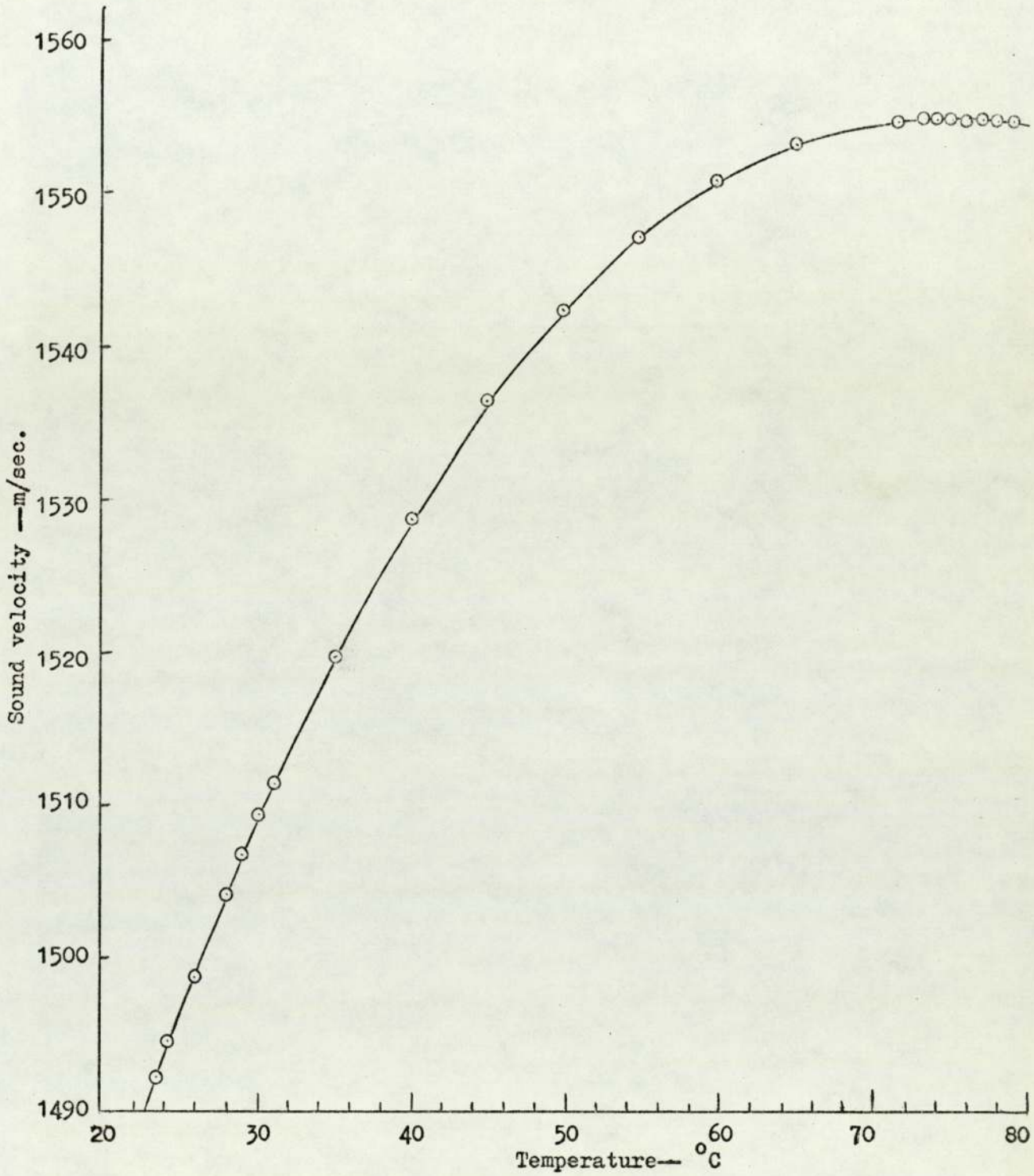


Fig. 2.6. Variation in sound velocity with temperature in water[30].

sound velocity with temperature in sodium[28] and water[30].

The resolution of the measurement system depends on the number of echo pulses received by the transducer during the fast movement of the bubble interface.

If one supposes that a bubble growth takes a time $t_B$ to reach a radius R, and that the number of pulses during $t_B$ is n, n observations for the change in bubble radius will be made and the time period between every two successive measured points will be $\tau = \frac{t_B}{n}$. The value of $(\tau)^{-1}$ is the repetition rate of the ultrasonic pulse transmitter and is known as the pulse repetition frequency (PRF) of the system. The resolution of the system in measuring the change in radius $\Delta R$ between each two successive pulses depends on $\tau$ and $\frac{dR}{dt}$, the bubble growth rate:

$$\Delta R = \frac{dR}{dt} \cdot \tau = (\frac{dR}{dt})/(PRF)$$

Theoretical predictions indicate that the value of $\frac{dR}{dt}$ is a function of R and the degree of superheat of the liquid. Thus, the PRF should be chosen according to the resolution required during those parts of the bubble life where $\frac{dR}{dt}$ is greatest. For example, at 50°C superheat in liquid sodium a bubble grows to 1cm radius within 2 msec. In order to obtain 10 measured points the sampling rate must be 5kHz. This PRF provides 25 observations for the same bubble growth at 20°C superheat.

The resolution and accuracy with which the initial growth of a bubble (from 0.5mm) can be measured depend on the magnitude of the echo signal which should be greater than the background noise level, the latter caused mostly by the spurious echoes received and partly by electrical noise.

Unfortunately, the echo signals from spherical bubbles (0.5mm to 10mm diameter) in comparison with those from flat reflectors are very weak.

Special effort must therefore be made to reduce the background noise level. When the system is used in a container with restricted dimensions, such as a compact sodium pool, the reverberation signals from the liquid surface or the walls can increase the background spurious signals significantly. This limits the PRF and thus the resolution of the system.

If the system is used for measuring the transient movements of a vapour layer at a flat surface away from the container walls[13,35], the above difficulties are not experienced. This is because the back-scattering cross-section of a reflector depends on its curvature and area. A comparison between a sphere of for example 1mm radius and a fairly flat circular reflector of the same radius, both placed in water at 10cm distance from a 5MHz transducer of 5mm radius, reveals that the amplitude of the echo from the sphere is only 5% of that of the flat reflector. The same sphere produces an echo amplitude of approximately 1% of the echo amplitude received from a circular reflector of 5mm radius.

Careful consideration must also be given to the echo signal shape which affects the dynamic range of the transducer. Transducers immersed in water can generate quite short pulses which are desirable for the system. The dynamic range of the transducer designed to work in the sodium pool is controlled by a number of factors. The principal limitation arises in the mounting of the transducer. A metal diaphragm, which isolates the transducer from the sodium, causes the transducer to ring for some time after the main pulse has been generated. This effect has been minimised significantly, as will be described later.

It will be shown that the straightforward echo delay method is capable of giving accurate, detailed information about bubble size in the sodium pool outlined in the report by Bevir/Kazemeini/Ralph[31]. In order to obtain maximum information about bubble growth, a second transducer sighted at

right angles to the first is used.

## 2.4 THE ULTRASONIC TRANSDUCER

In order to apply the ultrasonic transducer pulse echo technique in liquid sodium, it is necessary to introduce a mechanism to launch ultrasonic pulses into the sodium which is expected to be at temperatures up to 900°C. Furthermore, the ultrasonic pulse has to be in the megahertz range of frequencies because of the required resolution of the system. With the chosen frequency, 5MHz, the pulse rise time is not more than 50nsec; this gives a resolution better than 0.1mm in liquid sodium at 900°C. Among the transducers commonly used for longitudinal waves piezoelectric materials have the greatest sensitivity in the megahertz range[32,33]. Magnetostrictive transducers do not work well at such high frequencies. Some of the more common piezoelectric materials are given in Table 1 with their principal characteristics (Blitz).

TABLE 1

| Substance | d coefficient ($CN^{-1} \times 10^{12}$) | Electro-mechanical coupling coefficient, k (%) | Upper Curie temperature $T_c$ (°C) |
|---|---|---|---|
| Quartz (X-cut) | 2.3 | 11 | 550 |
| Barium titanate | 60 - 190 | 20 - 50 | 120 - 140 |
| Lead zirconate titanate (PZT) | 80 - 320 | 23 - 76 | 350 - 490 |
| Lead meta-niobate | 85 | 42 | 550 |
| Sodium meta-niobate | 80 - 160 | 51 - 53 | 290 - 420 |
| Lithium niobate | 6 | 18 | 1210 |
| Lithium tantalate | 8 | 31 | 660 |

As the table shows, all the materials except lithium niobate have a low Curie temperature, thus making it impossible for them to be used at 900°C. Even if these materials could be kept at a temperature below their Curie

points, there would still be a major problem in that they have to be protected by a stainless-steel diaphragm from chemical attack by the hot, reactive sodium. This leads to an acoustical matching problem between the transducer and the liquid since the acoustic impedance of steel is approximately fifteen times greater than that of liquid sodium. Achieving good acoustical contact between the piezoelectric material and the steel poses yet another problem. The widely-used coupling film, solid or liquid, limits the maximum operating temperature of the transducer. The protective steel diaphragm is also one of the main sources of loss and distortion in echo signals and also increases the background noise level of a pulse-echo system (as will be described in Chapter 4).

Among the materials in Table 1, the PZT ceramics are more common, since they are highly efficient and more sensitive as transducers. Their Curie temperatures range from 350°C to 490°C. Lithium niobate has the highest curie temperature although it is less efficient than PZT. In order to use lithium niobate in this situation, a good bonding able to withstand high temperatures is needed between the crystal and the protective steel diaphragm. Some of the techniques developed for bonding ceramics to metals have been applied for this purpose at the Karlsruhe Nuclear Research Centre[16] and at A.E.R.E. Harwell[34]. Among them, braze bonding with a non-oxidizing alloy has been fairly successful. However, although the brazed lithium niobate crystals can be used up to a maximum of 600°C, in practice their characteristics often change after short use at a high temperature (see Chapter 4). It was therefore decided to use PZT and by design avoid its direct exposure to the high temperature. This also enables the conventional ultrasonic paste to be used.

The high-temperature problem with PZT can be avoided by using a suitable temperature buffer, a cooled delay line, between the transducer and the hot liquid sodium, although that in itself poses problems. The buffer has to

be made of stainless steel in order to avoid corrosion. A solid rod is not suitable since, for each ultrasonic pulse transmitted into it, the echo signal received back from the target in the liquid consists of multiple trailing pulses[16] which are due to shear waves reflected across the rod. The spurious signals and the large bulk attenuation are not acceptable for the system. Since longitudinal/shear conversions do not occur significantly in liquid metals, and since bulk absorption in liquid metals is very small, a column of liquid metal of low melting point seemed the most promising solution. A suitable temperature buffer, therefore, as shown in Fig. 2.7 , is a liquid-sodium-filled tube which has at one end a stainless steel diaphragm forming an ultrasonic window between the transducer and the liquid. The buffer tube must also include an efficient cooler to keep the transducer below the maximum operating temperature. Thus, a negative temperature gradient will exist between the sodium pool and the transducer. This may present convection problems associated with refraction.

The piezoelectric material chosen for the measurement is a PZT5A disc of 10mm diameter and 0.4mm thickness (5MHz natural frequency). The Curie temperature of PZT5A is 350°C. As shown in Fig. 2.7 the transducer is attached by a film of coupling paste to the protective diaphragm at the base of the buffer tube. The beam from the transducer is slightly convergent to a distance of about 5.5cm (the near field), thereafter diverging to form the characteristic diffraction beam. Experimental results (Chapter 3) reveal that the axial sensitivity (determining the echo amplitude) is a maximum at distance N, the end of the near field (5.5cm in sodium) and falls to 50% of the maximum at 2N (11cm), to 25% at 3N (16.5cm), to 15% at 4N (22cm) and to 9% at 5N (27cm). Although a short tube is therefore desirable, in order to create a stable temperature gradient for a temperature range of 250°C to 900°C and to reduce the

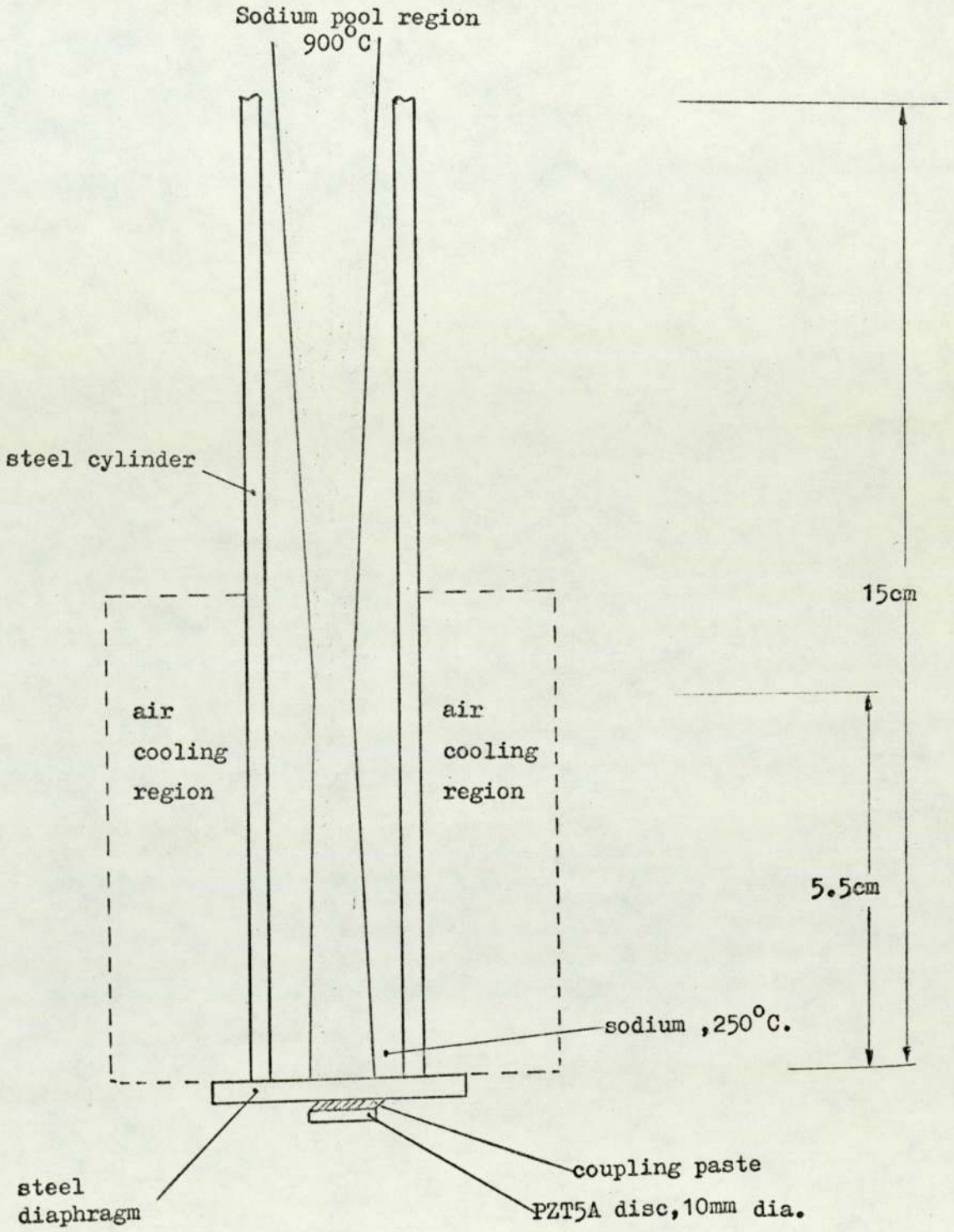


Fig. 2.7. Beam spread of 5 MHz PZT disc transducer along the cooling tube.

cooling requirements, the minimum possible length of the tube, using an efficient cooler, is about 15cm. In the design, the diameter of the tube must be about 2cm, slightly larger than the beam diameter at 15cm, so that the diverged beam does not hit the side of the tube. Taking 2400 m/sec as the average velocity of sound in sodium along the passage in the cooling tube, the return time of the echo for a distance of 15cm is 125μsec which corresponds to 8kHz pulse repetition frequency. However, the PRF can be increased to higher rates , provided that no serious interference from spurious echo signals is met. For PRFs higher than 8kHz the target echo will appear after a later transmission signal and not directly after the signal which has produced it. Thus, the apparent echo time-delay (the time between each transmission pulse and the target echo) becomes much less than 125μsec. Since the bubble must be nucleated in the middle of the main vessel (the sodium pool), the total length between the transducer and the bubble will be even more than 15cm. The total distance for the compact design of the sodium pool[31] is approximately 27cm. However, the measurement for this distance at a sampling rate of at least 5kHz is completely successful if the cooling tube is vertical, since the liquid at the top is the hottest thus suppressing convection. A convection problem arises when the tube is fixed in other orientations, although, as will be noted the bubble measurement is not seriously affected by it.

## 2.5 CONDITIONS IN THE SODIUM POOL

The sodium pool (constructed at A.E.R.E. Harwell), shown in Fig. 2.8 , has a main containment vessel in which the temperature reaches about 900°C. The vessel, made of Incoloy 800, is vertical, cylindrical and has an inside diameter of 12cm. As shown in Fig. 2.9 , the vessel has two openings leading into two cylindrical tubes used as temperature buffers for the two ultrasonic transducers. One tube, mounted at the base, is vertical and the other, mounted at the side of the vessel, is horizontal. The transducers are located at the end of these temperature buffer tubes; cooling is

provided in order to limit the temperature of the transducer to below 250°C.

The bubble nucleation rod is fixed vertically through the top lid of the vessel so that the end of the rod is situated in the middle of the vessel. The sound beam transmitted from the base transducer is therefore on the same axis as the rod.

In order to reduce the background reverberation level of the unwanted echoes received from the liquid surface by the base transducer, a signal deflector is placed near the liquid level. The deflector is a metal cone concentric with the bubble nucleation rod, as shown in Fig. 2.9. The improvement in the background reverberation in the pulse echo system is described in Chapter 5.

In order to obtain superheated liquid sodium, the pool is filled with sodium to a certain level, above which there extends to the top lid an approximate 100cc blanket of argon gas. The pool is heated to a steady controlled temperature somewhat below the saturation temperature corresponding to the cover gas overpressure. The overpressure is then slowly lowered until a superheated liquid condition results [31].

Thus a technique is required for the precise adjustment of the liquid level and for detection of accidental bulk boiling of the sodium. It was discovered that the pulse echo system employed in the pool can also be used for the above purposes. The liquid level can be adjusted with an accuracy of a fraction of a millimetre using the base transducer. Because there is a temperature gradient along the sound beam, the nucleation rod, which is fixed at a known distance in the isothermal region, is used as a reference for liquid level measurement. Furthermore, the back target echo method can be applied for bulk boiling detection, since the vapour bubbles nucleated within the beam change the amplitude of the echoes from the rod and from the liquid surface.

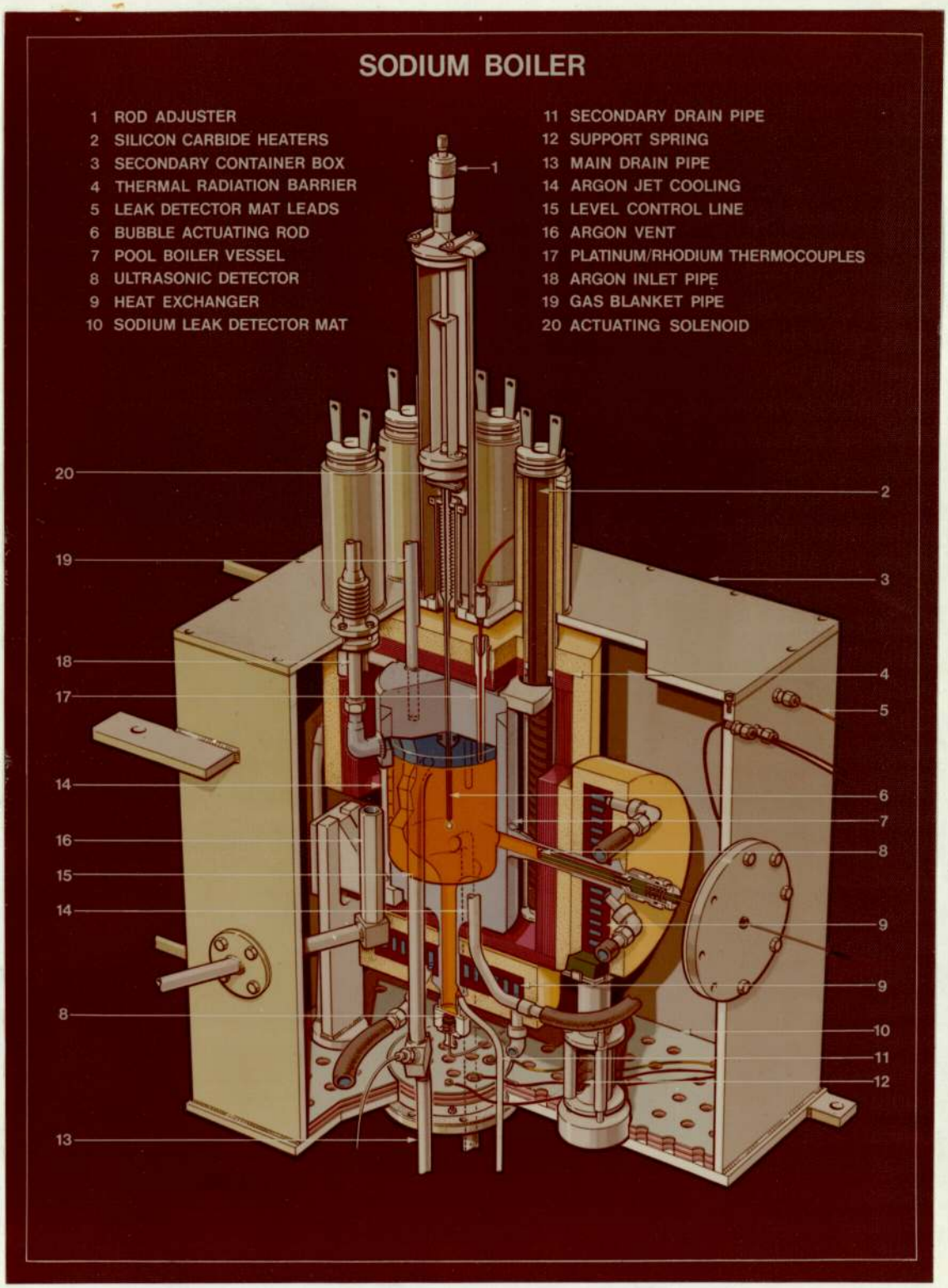


Fig. 2.8. The sodium pool boiler constructed at A.E.R.E. Harwell.

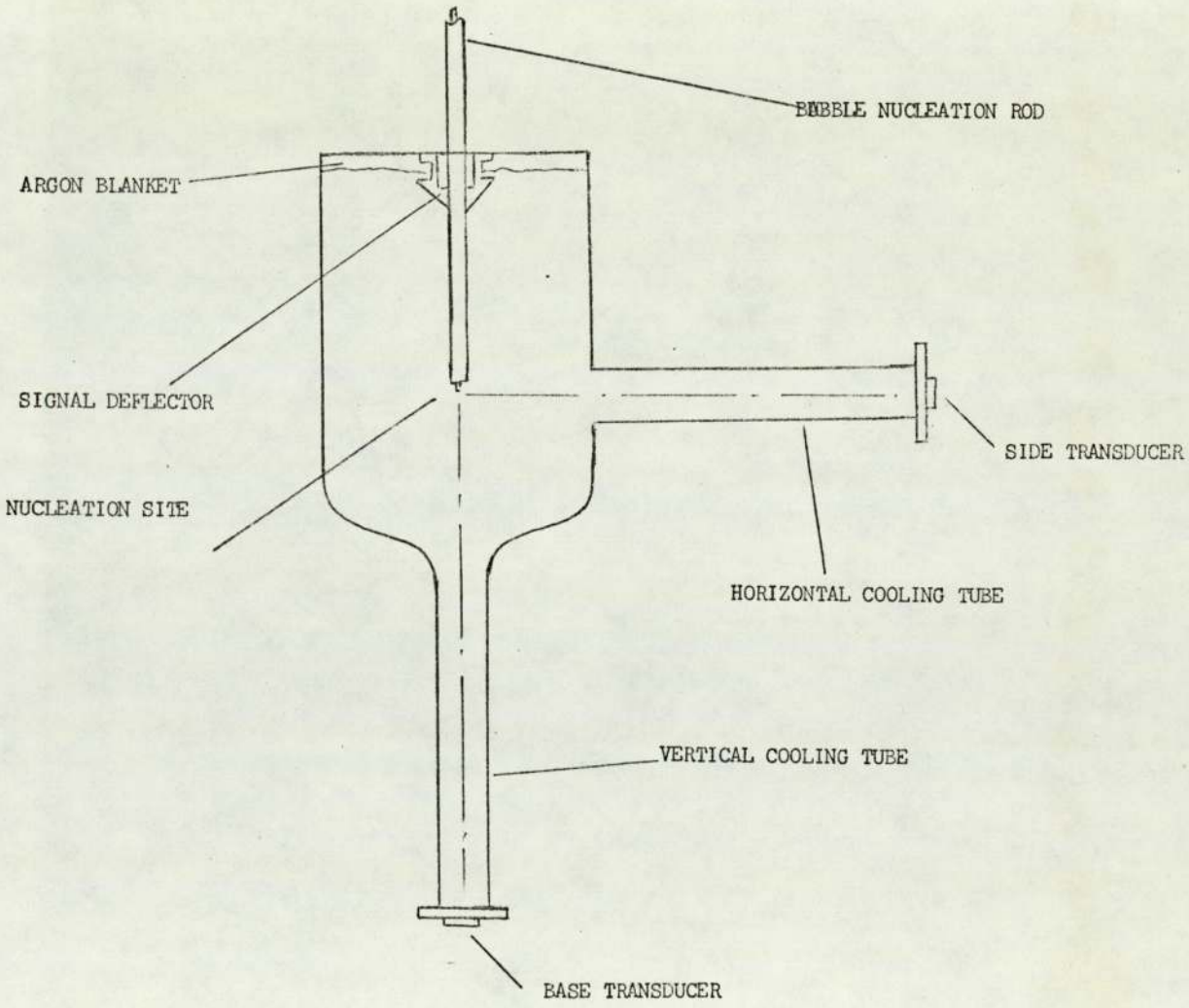


Fig. 2.9. Position of the ultrasonic transducers and the nucleation device in the pool.

# CHAPTER 3

## SOUND REFLECTIONS FROM A SPHERICAL TARGET

### 3.1 SOUND BEAM OF A PIEZOELECTRIC DISC

The spacial energy distribution from a real disc source can be described in terms of an ideal, rigid, circular piston source set in an infinite baffle. The function of the baffle is to prevent radiation from the rear of the piston travelling round to the front and interfering with forward-radiated energy. Every point on the piston surface moves in unison, though in an actual disc transducer this may not be the case. Quartz transducers, for example, may vibrate in a complex manner with several modes in evidence [57], and a pulse-excited piezoelectric disc may suffer larger displacements near the middle than at the edges. Nevertheless, the ideal piston serves as a useful basis for studies with real sources with continuous excitation and even, to some extent, with pulsed excitation; this is especially true when Piezoelectric ceramic PZT is used.

The sound pressure at any point in front of the piston varies with position in a complex manner due to the effect of what is essentially an infinite number of sources on the piston face, with varying path lengths to the point in question. The intensity on the piston axis is given by Beyer [36] as

$$I = 2\rho c u^2 \sin^2 \left[\frac{k}{2}(z_a - z)\right]; \quad z_a^2 = z^2 + a^2 \qquad (3.1)$$

where $\rho$ is the density of the medium, c the sound velocity, u the maximum velocity of the piston face, $k(=2\pi/\lambda)$ the wave number, a the piston radius and z the distance. This variation in intensity is shown in Fig. 3.1 as a function of $\frac{a^2}{\lambda}$. For large distances, the relationship simplifies to

$$I \simeq 2\rho cu^2 \, \mathrm{Sin}^2 \left[ \frac{ka^2}{4z} \right] \qquad (3.2)$$

The presence of several peaks and zeros is due to the successive reinforcement and destructive interference of waves at each point along the axis. The region up to the last peak (where $z = \frac{a^2}{\lambda}$) is known as the Fresnel zone or the near field, and that beyond it as the Fraunhofer zone or the far field.

In the far field the intensity decreases monotonically with the inverse square of distance ie.,as viewed from the far field, the piston is a simple source. Off axis, interference effects reduce the intensity; Morse[37]:

$$I = \frac{1}{4} \rho cu^2 (ka)^2 \left(\frac{a}{r}\right)^2 \left[ \frac{2J_1(x)}{x} \right]^2 \qquad (3.3)$$

where $x = ka \, \mathrm{Sin}\theta$, r is the distance of a point from the centre of the piston, $\theta$ the angle from the normal to the piston and $J_1$ a first order Bessel function. The term $2J_1(x)/x$ in the square brackets is known as the directivity function. Its first root specifies the angular width $2\theta_1$ of the main beam, and occurs where

$$ka \, \mathrm{Sin}\theta_1 = 3.832$$

or

$$\mathrm{Sin}\theta_1 = 0.610\lambda/a$$

When $\lambda/a$ is small, the main beam is strongly directional since $\theta_1$ is small; increasing $\theta$ from 0 to $90^o$ forces the directivity term through a number of maxima and minima the amplitudes of which decrease rapidly. These maxima and minima identify several minor lobes. When $\lambda/a$ is made large, however, the Fresnel zone is much shortened and the directivity function becomes far more dependent on the value of ka than upon $\theta$; in

fact, even where $\theta = 90^{o}$ (ie along the baffle surface) the value of $2J_1(ka)/(ka)$ may be little different from its initial value of unity. This, of course, is tantamount to saying that the source radiates equally in all forward directions, which is indeed expected for long wavelengths and small radiators. The corresponding equation for pressure is

$$p = \frac{1}{2} \rho c u k \left(\frac{a}{r}^2\right) \left[\frac{2J_1(x)}{x}\right] \qquad (3.4)$$

where p and I are related by $I = \frac{|p|^2}{\rho c}$. In the region where $\theta$ is small,

$$\text{Sin}\theta = \theta = \frac{h}{r}$$

where h is the distance of a point from the beam axis. Thus equation (3.4) can be given in cartesian co-ordinates as

$$p = \frac{1}{2} \rho c u k \left(\frac{a}{r}^2\right) \left[\frac{2J_1(kah/r)}{kah/r}\right] \qquad (3.5)$$

Equation (3.4) for points on the beam axis reduces to

$$p = \frac{1}{2} \rho c u k \frac{a^2}{r} \qquad (3.6)$$

In practice, the rim of a pulse-excited piezoelectric disc-transducer vibrates with a smaller amplitude than that of the centre part[38]. The multiple-path reinforcements and interferences are not therefore so pronounced as in the mathematical model, and the on-axis pressure fluctuations in the Fresnel zone are smaller. In addition, for short pulses of oscillations, the interferences diminish when the path length differences are large. The pressure-distance relationship is more usually like Fig. 3.2b, but the exact pattern depends on the type and the size of the transducer and its mounting. In this figure there is only one large

maximum, near where $r = a^2/\lambda$, indicating a concentration of power in this region. In a practical situation this could be considered as the near field-far field boundary.

A simplified model is often adopted[39] in which the sound beam is imagined to converge cone-like from the transducer face to the end of the near field, and thence to diverge conically into the far field (Fig. 3.3). At the boundary of the two cones the sound intensity on axis is again, therefore, a maximum which complies with the theoretical model. The first root of the directivity function gives a suitable measure of the angular divergence $2\theta_1$ of the far field cone.

## 3.2 ECHO AMPLITUDE

When a sound wave in one medium meets a boundary with another medium of different acoustic impedance, part of the wave energy is transmitted through the boundary and the remainder is reflected back into the primary medium. The cases of plane waves meeting plane and small-curvature boundaries are well known, for there are close optical analogies.

Plane waves which meet non-planar objects with large curvatures or irregularities give rise to complex patterns of reflection, and their spacial distributions depend not only on the properties of the media and the reflector shapes but also on the relative size of the reflector and the wavelength.

Morse (op. cit.), among others, has directed his attention to the case of a plane wave striking an acoustically-hard sphere. In this context he used the term 'scattered wave', where scattering has a specific meaning within this subject. The actual disturbance at any point in the medium is imagined to be the sum of two waves: the first one is the original or primary wave which would have been present if the target

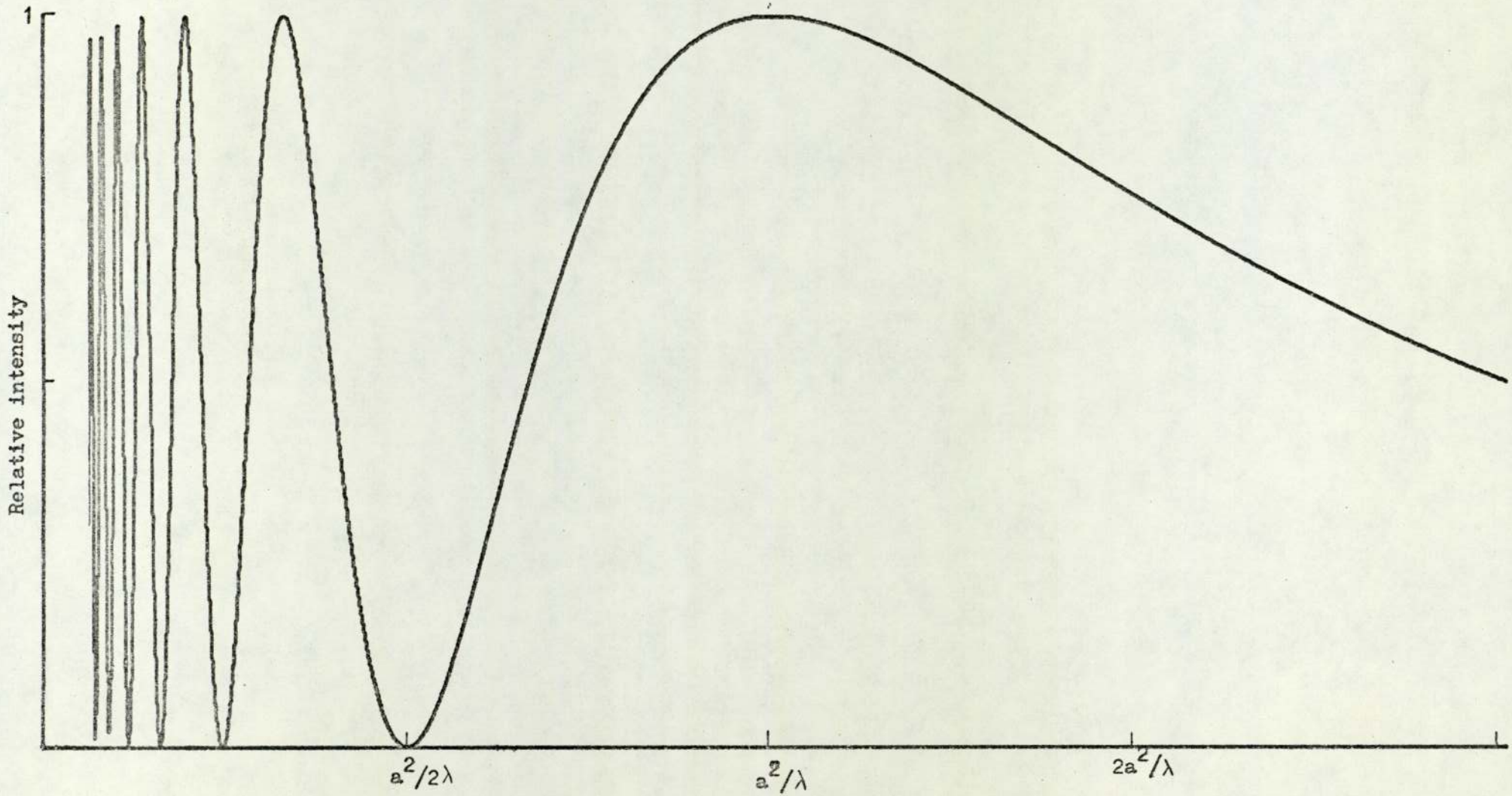


Fig. 3.1. Variation in intensity on axis of piston oscillator .

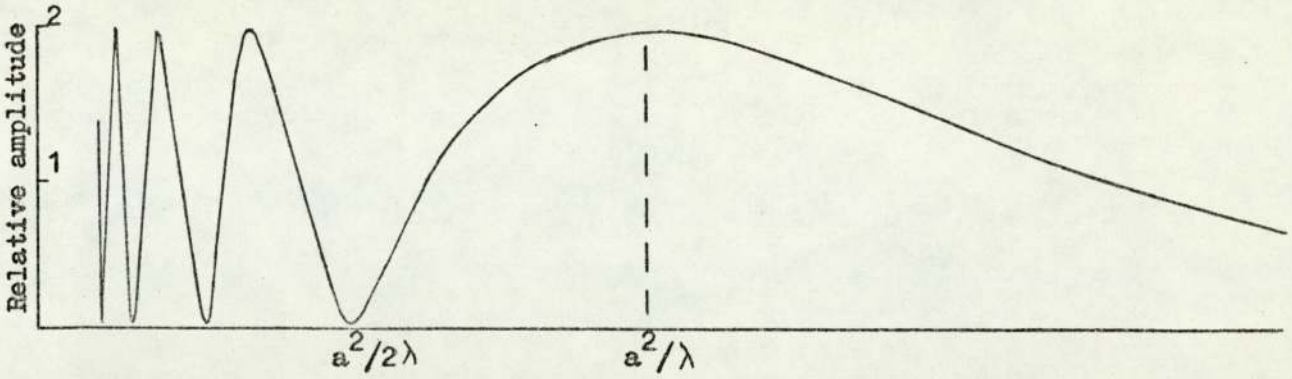


Fig. 3.2a Acoustic pressure on the axis of an ideal piston oscillator.

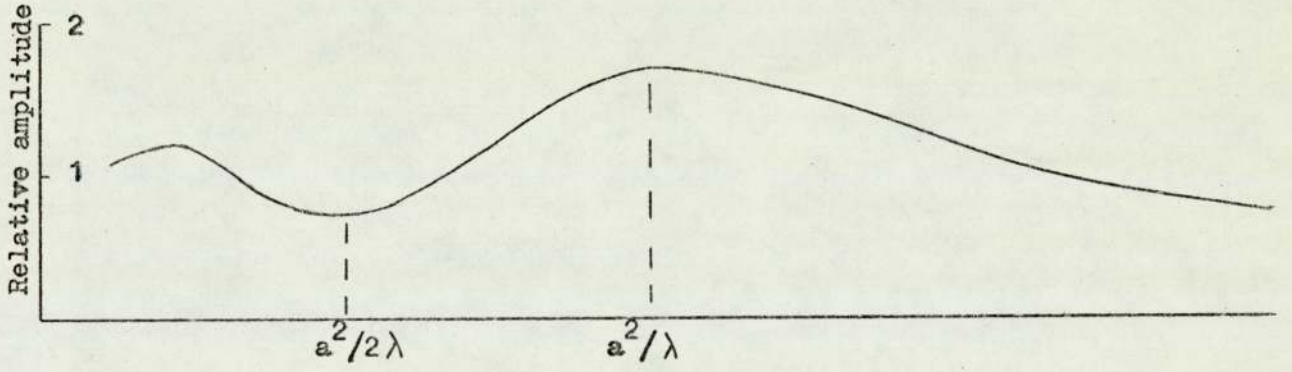


Fig. 3.2b Acoustic pressure on the axis of an ordinary disc oscillator.

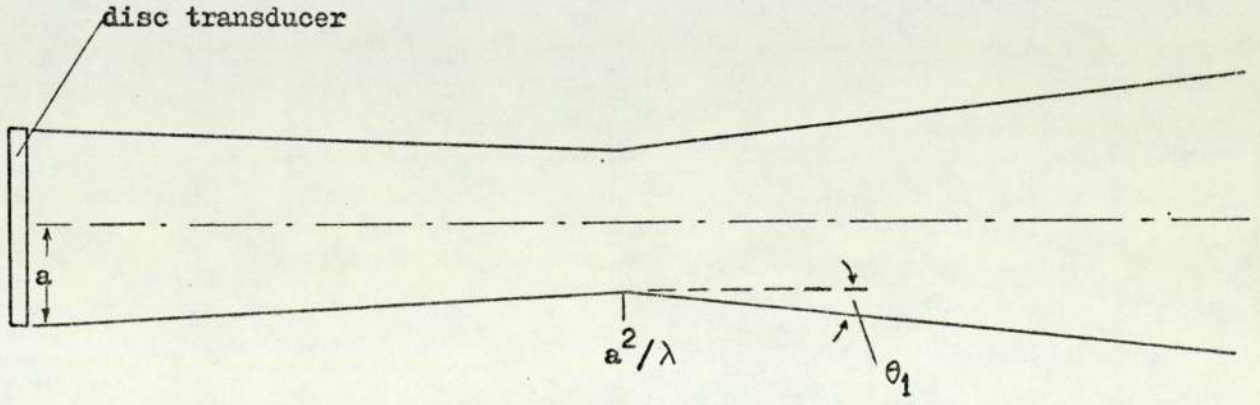


Fig. 3.3. Simplified presentation of the sound field.

sphere were not there, and the second is a 'conceptual wave', which is the scattered wave. Thus, an evaluation of the scattered wave leads to the actual wave by a superposition. Morse confined his work to continuous waves, but it may be applied with acceptable results to the case of a short pulse of waves.

The intensity of the wave can be expressed conveniently only for the extreme cases where $ka'<<1$ and $ka'>>1$ where $a'$ is the sphere radius. A solution for the region where the wavelength and the radius are of the same order is intractable.

At a large distance r from a hard sphere the intensity $I_s$ and total power $\Pi_s$ of the scattered wave are

$$I_s \simeq \begin{cases} 4/9\ (ka')^4 (a'/2r)^2\ I_o\ (1-3\mathrm{Cos}\theta)^2; & ka'<<1 \\ (a'/2r)^2\ I_o\ [1 + \cot^2(\frac{\theta}{2}) J_1{}^2 ka'\mathrm{Sin}\theta]; & ka'>>1 \end{cases} \tag{3.7}$$

$$\Pi_s \simeq \begin{cases} \frac{16}{9}\ \pi a'^2 (ka')^4\ I_o; & ka'<<1 \\ 2\pi a'^2\ I_o \quad ; & ka'>>1 \end{cases} \tag{3.8}$$

where $k = \frac{2\pi}{\lambda}$, $I_o$ = incident intensity. The centre of the sphere is taken as the origin of the polar co-ordinates, and the angle $\theta$ is measured from the polar axis in the direction of the incident beam. Equation (3.7) shows that when $ka'>>1$, the scattered intensity off the face of the sphere is uniform; only behind the sphere (where $\theta \simeq 0^o$) is the term within the square brackets other than about unity. The second term within these brackets represents very large diffraction lobes behind the target. When one adds together the scattered wave and the primary wave behind the target in order to determine the actual wave, one finds that the waves interfere destructively with each other

to produce large regions of shadow; although the effect is complex, it is not unexpected, since the condition $ka' \gg 1$ is similar to the geometrical-optical case where strong shadows are cast.

The scattered power, $\Pi_s$, is obtained by integrating $I_s$ over a closed surface about the sphere. Considering again the case where $ka' \gg 1$, $\Pi_s$ is seen to be twice the power contained within a beam which embraces the cross-section of the sphere, $\pi a'^2$. This apparent paradox is resolved when one realises again that the actual total power behind the beam is zero, so that the actual power reflected off the target is half of the scattered power.

The intensity in front of the target, as already noted, is widely distributed when $ka' \gg 1$. At the other extreme, when $ka' \ll 1$, the polar diagram of intensity is double-lobed, according to the $(1-3\cos\theta)^2$ term; a smaller lobe is directed along the axis behind the target, showing the presence of a small shadow, and a larger one is directed back towards the source. The scattered intensity in this case is greatly dependent on the target size, relating to $(a')^6$. This, in the optical analogy, corresponds to Rayleigh scattering.

### 3.2.1 Back-Scattering Cross-Section

A parameter often used in radar to describe the effectiveness of a target as a reflector is the radar or back-scattering cross-section[25], $\sigma$, having dimensions of area. The definition of $\sigma$ is based on the concept that the reflected power detected at a receiver is part of an isotropic re-radiation from the target (although this is usually far from true with real targets, in radar as in acoustics). Nevertheless, one then computes the plane target area which would have intercepted all of this retransmitted power; this target area is $\sigma$.

A similar concept may be applied in acoustics, and is, in effect, a

restatement of the scattering principles discussed in the previous section.

If $I_o$ is the intensity incident on the target and $I_s$ that at the receiver, which is at distance r from the target, then

$$I_s = \frac{\sigma I_o}{4\pi r^2} \qquad \text{or} \quad \sigma = 4\pi r^2 \frac{I_s}{I_o} \tag{3.9}$$

For a given radar or sonar situation (fixed r and $I_o$) $\sigma$ is therefore a useful measure of the strength of the echo. It depends on the shape, dimensions and orientation of the target, and also on the incident wavelength. It should be noted that, in reality, $\sigma$ is nothing more than a convenient mathematical term, since, for most practical targets, it cannot be assigned a unique numerical value.

The back scattering cross-sections of a few simply-shaped targets in acoustics have been calculated using radar analogies[40]. A rigid sphere in acoustics has similar reflecting properties to those of a perfectly-conducting sphere in the electromagnetic case. Its cross-section $\sigma$ is calculated as follows. According to the definition of $\sigma$ the intensity of the back-scattered wave $I_s$ at distance r must be determined. The intensity, given by equation (3.5) is uniform in all directions when $ka' \gg 1$, but has a maximum value in the opposite direction to that of the incident wave ($\theta = 180$) for the case $ka' \ll 1$:

$$I_s = I_o \left(\frac{a'}{2r}\right)^2 ; \qquad ka' \gg 1$$

$$I_s = \frac{64}{9} I_o \left(\frac{a'}{2r}\right)^2 (ka')^4 ; \quad ka' \ll 1$$

Thus, the back-scattering cross-section becomes

$$\sigma = \pi a'^2 ; \qquad ka' \gg 1 \tag{3.10}$$

$$\sigma = \pi a'^2 \left(\frac{64}{9} (ka')^4\right); \qquad ka' \lesssim 1 \tag{3.11}$$

Equations (3.10) & (3.11) agree with Fig. 3.4, which shows the radar cross-section for a perfectly-conducting sphere. The initial rise, where $ka' \ll 1$, occurs in the Rayleigh region. The remarkable region which follows, where a' is of the same order as $\lambda$, shows large fluctuations in effective area as ka' changes. Algebraic solutions for these conditions are not available in a simple form; Morse has not revealed them, and the reader is normally directed to the solutions obtained by King and Wu[41] for the radar analogy.

For larger values of ka' the fluctuations diminish, and $\sigma$ approaches the geometric cross-section of the sphere, and is independent of frequency. These are the conditions to which geometric optical concepts apply. For a gas bubble in a liquid, the back-scattering cross section in the geometrical region (where $ka' \gg 1$) is similar to that of a rigid sphere, ie it is equal to the physical cross-section $\pi a'^2$. In the region where a' is of the same order as $\lambda$ the natural bubble oscillations, however, have an effect on the back-scattering cross-section. At the resonant frequency $\sigma$ goes to a maximum (46). Below resonance, $\sigma$ falls rapidly with decreasing radius. Gas bubbles of resonance size suspended in water reduce considerably the echo amplitude in sonar systems.

### 3.2.2 Effective Reflecting Area

A spherical acoustical reflector which is subject to the condition $ka' > 8$ (see Fig. 3.4) behaves in a manner analogous to the geometrical optical case. The energy received by a small receiver by reflection off the sphere at a large distance is that which strikes actually only a small area of the sphere concentric with the beam axis. This small area (PMQ in Fig. 3.5a) is the effective reflecting area of the sphere and is considered here as a flat circular reflector PQ which re-radiates along the axis

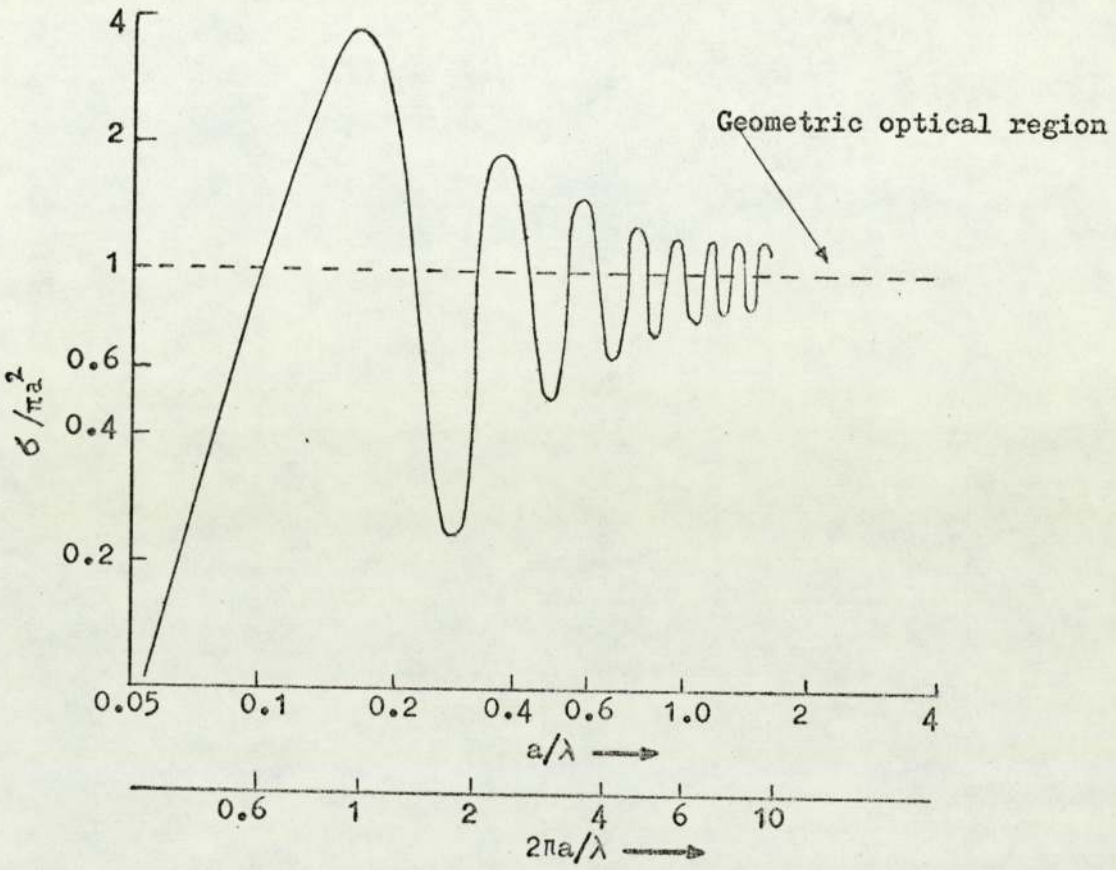


Fig. 3.4. Ratio of back-scattering cross-section to geometrical cross-section as a function of radius to wavelength for a sphere with infinite conductivity. (Copied from 'Propagation of Short Radio Waves' by D.E. Kerr).

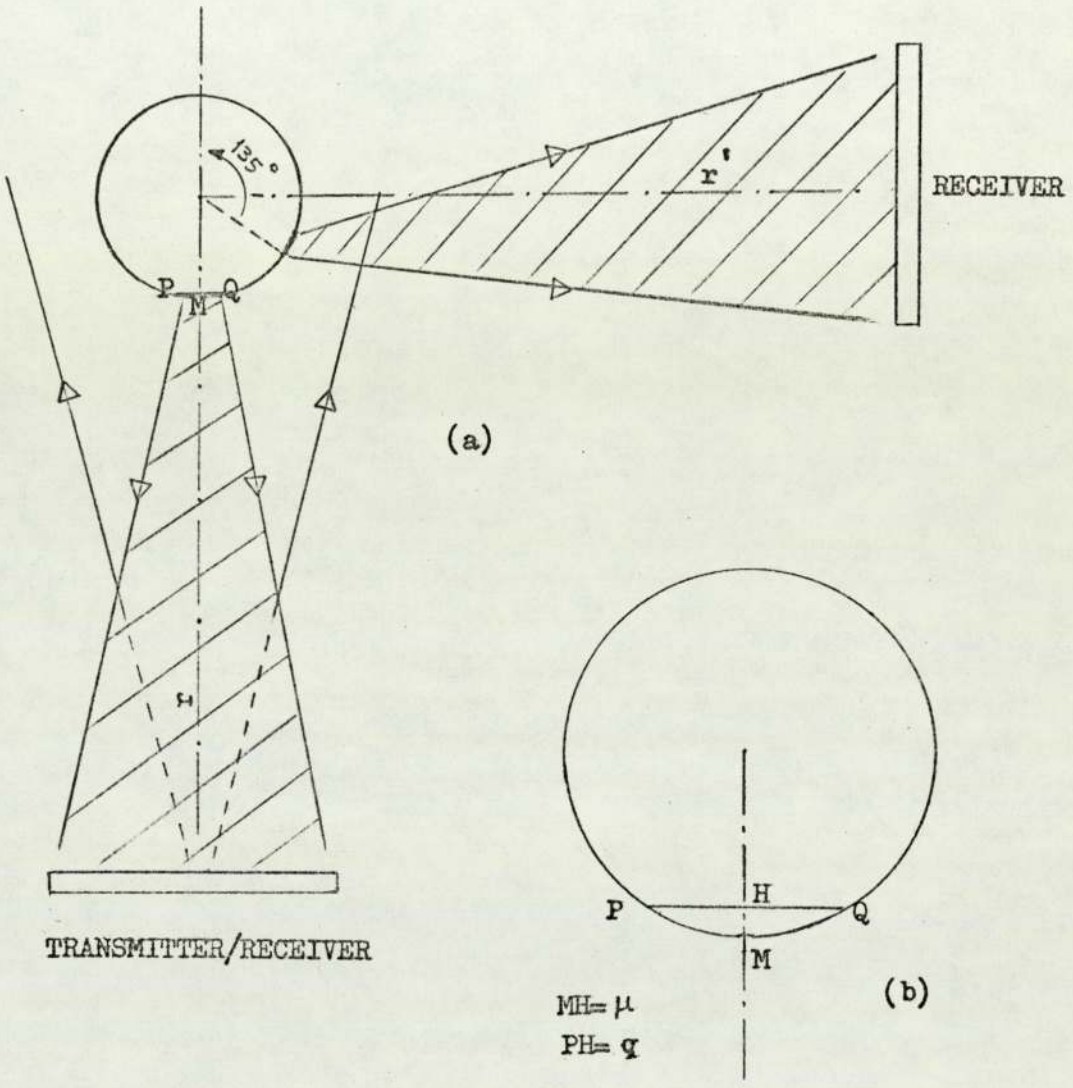


Fig. 3.5. Echoes from a spherical object; (a) on the axes of the two disc transducers at right angles; (b) effective reflecting area.

and produces the echo observed from the sphere. In other words, both the circular reflector PQ and the sphere have an equal back-scattering cross-section.

According to equation (3.7), for an incident plane wave the back-scattered intensity from a sphere (at $\theta = 180^{o}$) is

$$I_s = I_o \left(\frac{a'}{2r}\right)^2 \tag{3.12}$$

where $I_o$ is the uniform incident intensity over the small circular area PQ. A flat circular reflector perpendicular to a plane wave re-radiates as a piston source[56,43]. For a perfect reflector, the re-radiated intensity close to the reflector is equal to the incident intensity $I_o$. Similarly, by assuming that the PQ area acts as a piston source the reflected intensity at distance r on the axis is obtained from equation (3.3) as

$$I = \frac{1}{4} I_o k^2 q^4 / r^2 \tag{3.13}$$

where q is the radius of the circular area PQ. A comparison of equations (3.12) and (3.13) results in

$$q^2 = \frac{1}{k} a' \quad \text{or} \quad q^2 = \frac{\lambda}{2\pi} a' \tag{3.14}$$

which shows $q \ll a'$ if $\lambda \ll 2\pi a'$. For a given sphere, as the incident wavelength increases, the value of q increases too and thus a larger area of the sphere is responsible for the echo amplitude.

Small spheres are often used[42] for determining the pattern of the incident intensity across the sound field of a disc transducer. This method is accurate since the effective reflecting area receives in effect a uniform intensity $I_o$ although the intensity over the sphere face could be non-uniform.

The simple geometric construction in Fig. 3.5b shows that

$$q^2 = 2\mu a' - \mu^2$$

In the geometrical region $q \ll a'$ the term $\mu^2$ can be ignored and the value of $\mu$, shown in Fig 3.5b, becomes

$$\mu = \frac{1}{2k} = \frac{\lambda}{4\pi}$$

which is the maximum possible error in determining the exact position of the sphere face on the axis from the measured value of the echo transit time.

### 3.2.3 Back-scattered Echo

When a sphere is situated on the beam axis in the far field of a piezoelectric disc transducer (see Fig 3.5a), the incident intensity over the sphere face may not be uniform. It decreases away from the axis, according to equation (3.5). But as long as the incident intensity over the effective reflecting area is uniform the intensity received at the transducer will be uniform too. The echo energy, therefore is proportional to $\sigma(=\pi a'^2)$ or the square of the sphere radius.

In the case where the incident intensity over the effective reflecting area is non-uniform the receiving transducer face is also subject to a non-uniform intensity. This is more noticeable for flat targets, since the whole area is responsible for the back-scattered echo. For a flat circular disc the echo amplitude was calculated by Rumsey[43] who used equation (3.5) and took the average incident energy over the area of the disc and of the transducer. He assumed that the disc re-radiates as a piston source with a maximum velocity proportional to the average incident energy, and achieved a satisfactory equation. Using $A_o$, the amplitude of the echo received from a large flat plate parallel and close to the trans-

ducer, as a reference signal, the equation is given by

$$A = 2A_o\, e^{-2\alpha r} \int_0^{kaT/r} [J_1(x)]^2/x\, dx \qquad (3.15)$$

where $x = kah/r$, T is the disc radius and $\alpha$ is the bulk attentuation of the liquid. The equation is more accurate for smaller x, since the incident intensity over the disc is more regular. For $kaT/r < 0.5$, $J_1(x) \simeq x/2$, it therefore reduces to

$$A = \frac{1}{4} A_o (e^{-2\alpha r}) \; (kaT/r)^2 \qquad (3.16)$$

At given distance r the relative echo amplitude can be written as

$$H = A/2A_o\, e^{-2\alpha r} = \int_0^{kaT/r} [J_1(x)]^2/x dx \qquad (3.17)$$

Fig. 3.6 shows the variations of H versus kT for a disc placed at different distances (10cm, 20cm, and 30cm) when a = 5mm.

By substituting q (the radius of the effective reflecting area of a sphere) for T, equation (3.17) gives the relative echo amplitude from a sphere as:

$$H = A/2A_o\, e^{-2\alpha r} = \int_0^{kaq/r} [J_1(x)]^2/x dx;\; q^2 = a'/k \qquad (3.18)$$

Fig. 3.7 shows the variation of H versus ka' for spheres placed on the beam axis at distances 10, 20 and 30cm when a = 5mm. For $a/r(ka')^{-\frac{1}{2}} < 0.5$ the value of H is almost a linear function of ka':

$$H = \frac{1}{8} (ka')\; a^2/r^2 \qquad (3.19)$$

As Fig. 3.7 shows, the linear region extends to larger ka' at greater distances. The linear region is related to the spheres whose effective reflecting area receives uniform incident intensity.

FIG. 3.6 VARIATION OF ECHO AMPLITUDE WITH KI

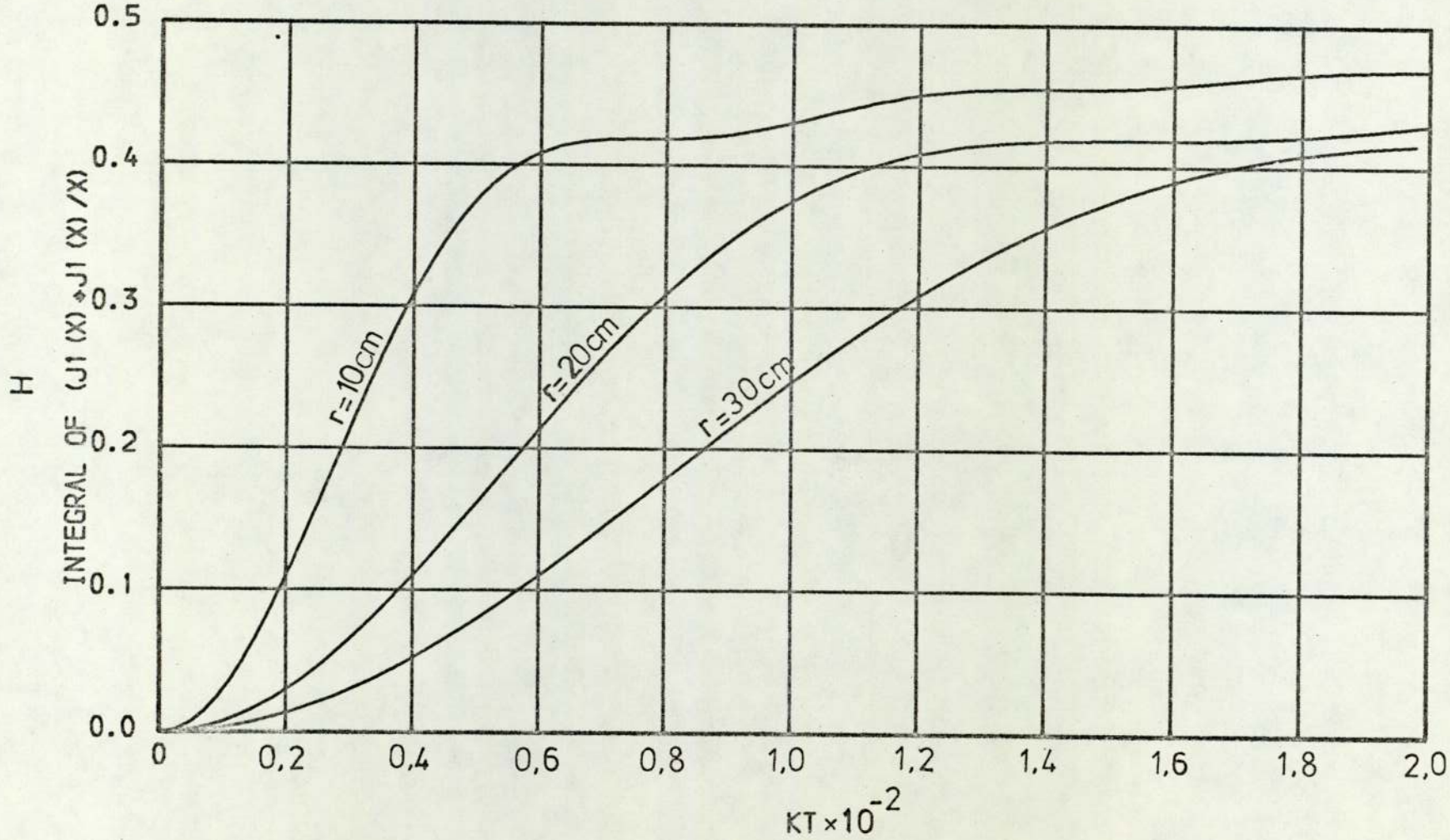

FIG. 3.7 VARIATION OF ECHO AMPLITUDE WITH Ka'

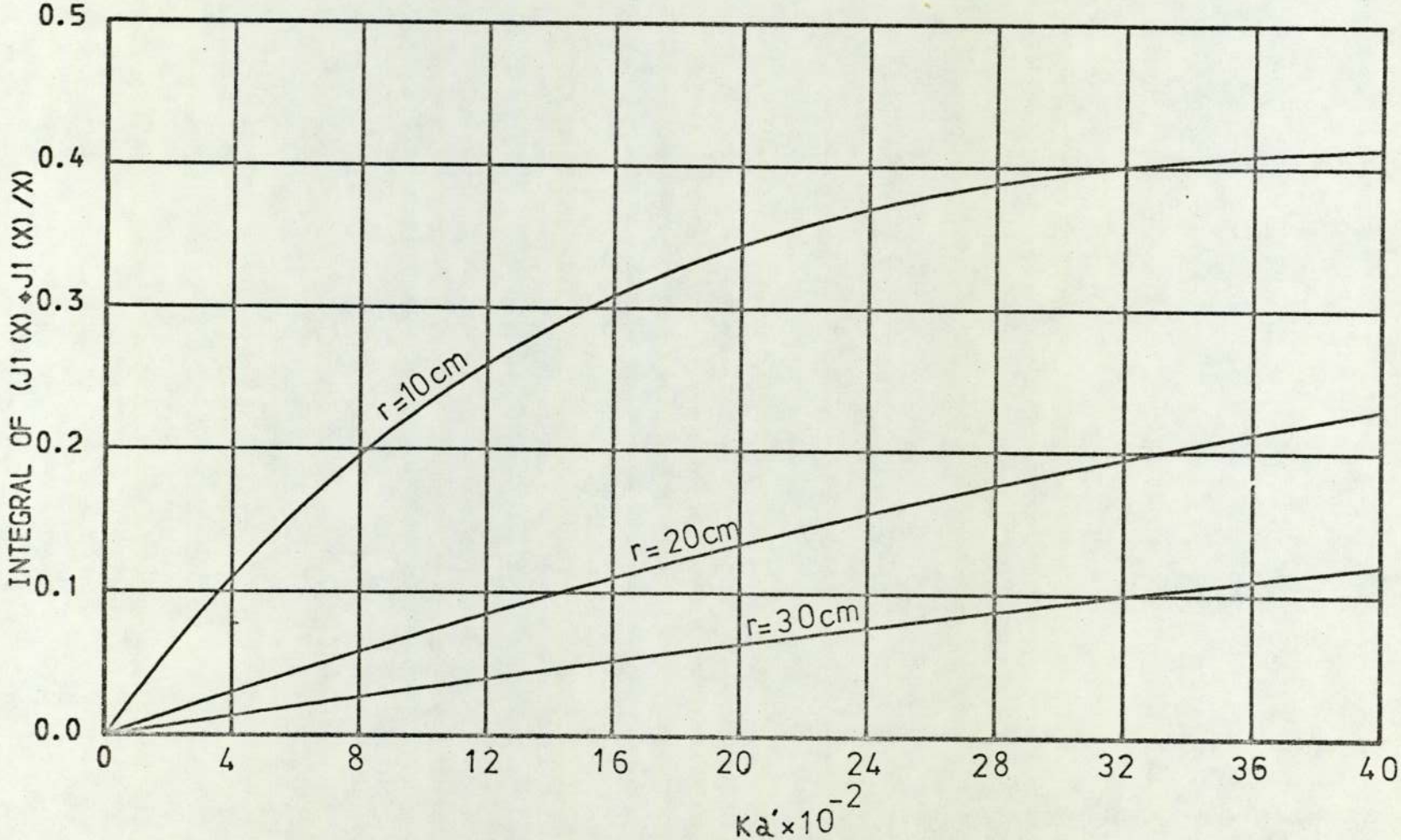

### 3.2.4 Echo Scattered at Right Angles

If a second receiving transducer is placed at a large distance r' from the sphere and in a direction which makes an angle $90^o$ to the incident beam (see Fig. 3.5a), the intensity received, according to equation (3.7), is

$$I_s = I_o(a'/2r')^2; \qquad ka' >> 1 \tag{3.20}$$

Simple geometrical-optical concepts show that the energy of the echo received at $\theta = 90^o$ is the energy reflected from a small area at $\theta \approx 135^o$ on the sphere face, as shown in Fig. 3.5a. The distance from the centre of this area to the axis of the incident beam is given approximately by $h \simeq a'/\sqrt{2}$.

Since the incident beam is the far field of a piston source (the first transducer), the incident intensity $I_o$ decreases off axis; at a point with distance h from the axis it is given by equation (3.3). Equation (3.20), therefore, changes to

$$I_s \simeq \frac{1}{2} \rho c u^2 (a/r')^2 \, J_I^{\,2}(x) \tag{3.21}$$

The echo amplitude becomes

$$A \simeq \frac{1}{\sqrt{2}} A_o(a/r') \left| J_1(x) \right| \tag{3.22}$$

where $x = kah/r$. For $x < 0.5$ the echo amplitude is approximately a linear function of radius and for $x = 3.8$ the amplitude becomes zero.

The change in transit time of the echo reflected from a growing bubble at $\theta = 90^o$, therefore, has the following approximate relationship with the bubble radius:

$$\Delta t \simeq \sqrt{2}\, a'/c \tag{3.23}$$

## 3.3 EXPERIMENTAL VERIFICATION

In order to compare the echo amplitudes from spherical and circular targets, and verify the theoretical predictions, some measurements were carried out in a container filled with water. Three piezoelectric disc transducers, type PZT5A, of 10mm diameter and of 1, 2.5 and 5MHz frequencies were employed.

For each measurement the transducer was used as a combined transmitter/receiver and was immersed in the water. The PZT disc was mounted on the end of a metal tube (40cm long) and backed with araldite. Its electrodes were electrically connected to a socket fixed at the other end of the tube. The tube enabled the transducer to be adjusted in two directions: along the axis and perpendicular to the axis. The transducer was driven by an excitation voltage pulse and generated a short pulse with few oscillations. It was observed that the predominant frequency of the echo signals received was considerably less than the natural frequency of the PZT disc. This was attributed mainly to the araldite backing (Kossoff)[45] and partly to the attenuation of the high-frequency components of the pulse in the liquid. Thus, what is known as the "average frequency" was applied for analysis of the experimental results. This can be measured by counting the centre group of individual cycles. The measured average frequencies for the three transducers were as follows: PZT, nominal 5 MHz: 4.1 MHz; PZT, nominal 2.5 MHz: 2.0 MHz; PZT nominal 1 MHz: 0.9 MHz.

The targets chosen were a series of steel ball-bearings of various diameters ranging from 1.6mm to 22.2mm, and a series of steel rods with flat ends; these had diameters ranging from 0.5 to 9.5mm and acted as circular reflectors. For each measurement, the target was fixed in the container and the transducer axis was aligned with the target. To ensure that the beam axis was perpendicular to the target face and passed through

the target centre, the transducer was adjusted to a position where a maximum echo amplitude could be obtained.

In order to show the variation of the echo amplitude when the target was placed at points off the beam axis, a steel ball of 3.9mm diameter was chosen. The 5MHz transducer was moved perpendicular to the axis and passed over the target at different distances; the variation of the echo amplitude (peak-to-peak amplitude of the first cycle) was recorded (Fig. 3.8 ). Since the 3.9mm sphere has a small effective reflecting area, Fig. 3.8 represents the incident intensity at points within the incident beam.

Using the natural frequency of the PZT disc (ie 5MHz) the near field length in water is approximately 8cm. This becomes 6.6cm if the average frequency (4.1 MHz) of the echo pulse is assumed.

As Fig. 3.8 shows, the echo amplitude across the beam in the near field fluctuates and decreases sharply near the edge of the beam. These fluctuations almost disappeared in a similar measurement when a 1.6mm rod end was used, indicating that the effective reflecting area of the 3.9mm sphere was even smaller than a circular area of 1.6mm diameter.

Fig. 3.8 also shows that the incident intensity in the near field region becomes greater on the axis as the distance increases. At 8cm the sharpness of the curve is due in fact to the focusing of the incident beam on the axis. As Fig. 3.8 shows, at distances beyond 10cm the echo amplitude (or the incident intensity) in general drops with distance but becomes more uniform over the centre of the beam; this was predicted in Fig. 3.7. The linearity of the graph in Fig. 3.7, which is related to the uniform incident intensity over the effective reflecting area, extends to larger spheres at larger distances. The approximate radius of the uniform area at the centre of the beam can be calculated from

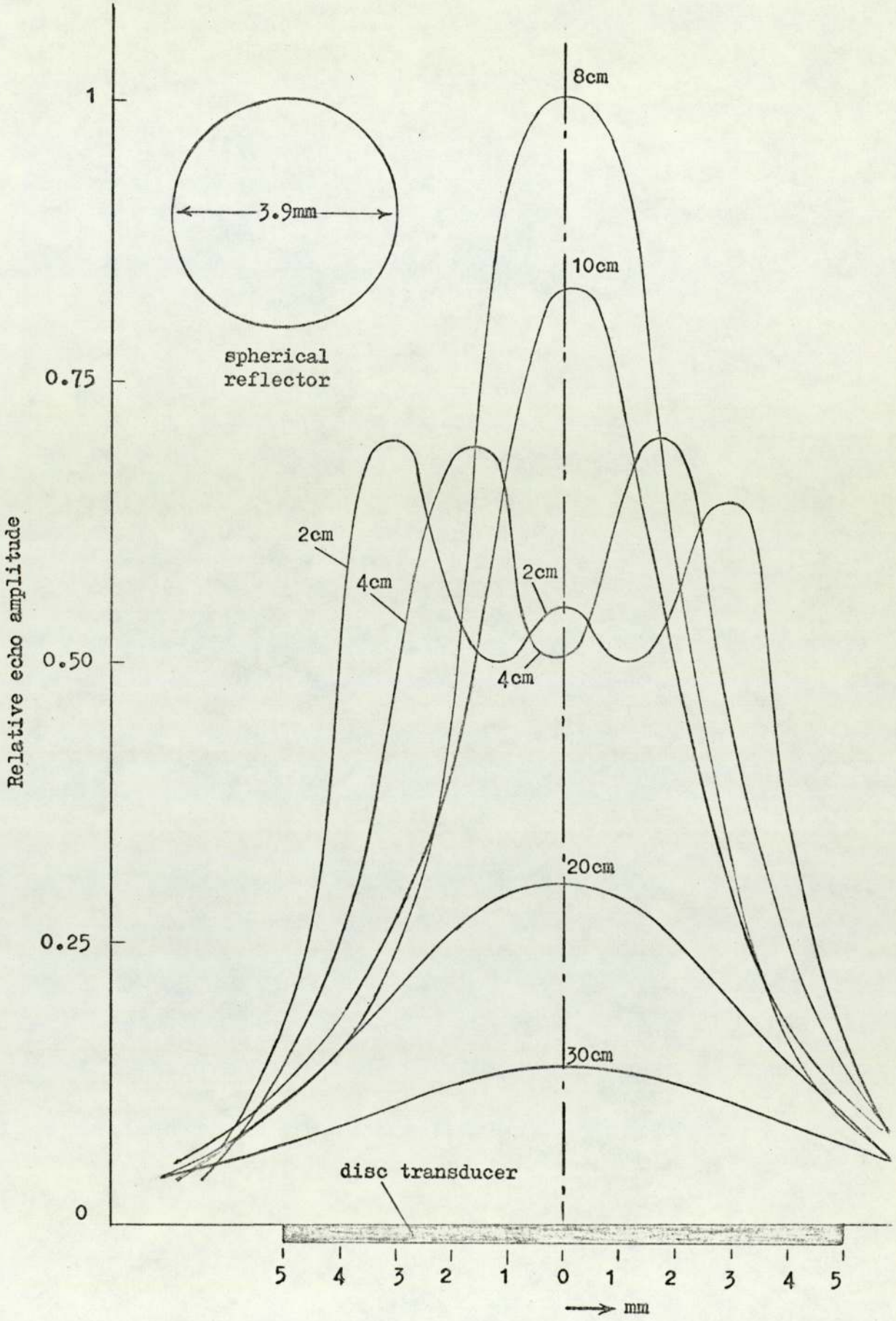


Fig. 3.8. Echo amplitude distribution of ball bearing (3.95mm) scanned by 5 MHz PZT disc of 10mm.

$kaq/r = 0.5$; at r = 10cm, r = 20cm and r = 30cm the values of q are 0.5mm, 1mm and 1.5mm respectively.

The variation of the echo amplitude with distance along the axis for various targets was also measured and plotted in a logarithmic scale similar to the AVG diagrams (Krautkrämer)[56]. The echo amplitude from a large flat plate fixed at 1cm parallel to the transducer face was chosen as reference amplitude $A_o$. Figs 3.9, 10 and 11 show the results for the three transducers (of 1, 2.5 and 5MHz). These figures show that in the near field the echo amplitude from the flat plate decreases slightly with distance, mostly due to liquid bulk attenuation. The rate of decrease with distance becomes much greater in the far field; the curve becomes a straight line with a gradient of almost one.

Comparison of the results obtained for spheres and those for rod ends (Figs. 3.9, 10 and 11) indicates that they have a similar pattern over the whole range of distance (in the far field and near field). This agrees with the assumption that a sphere has a small effective reflecting area which acts as a flat circular reflector with a constant area at any distance from the transducer.

It is also observed in Fig. 3.9 that the echo amplitude from the 12.7mm sphere, for example, is even smaller than that for a 1.6mm flat circular reflector for the whole range of distance, showing that the effective reflecting area of the sphere is smaller than the area of the 1.6mm rod.

Comparisons of Figs. 3.9, 10 and 11 shows that for a given sphere the effective reflecting area increases as the frequency decreases. For example, in Fig. 3.9 (using the 5MHz transducer, 4.1MHz average frequency), the echo from the 22.2mm sphere is smaller than that from the 2.4mm rod end while this situation is reversed in Figs. 3.10 and 3.11 (2.0 and 0.9MHz respectively).

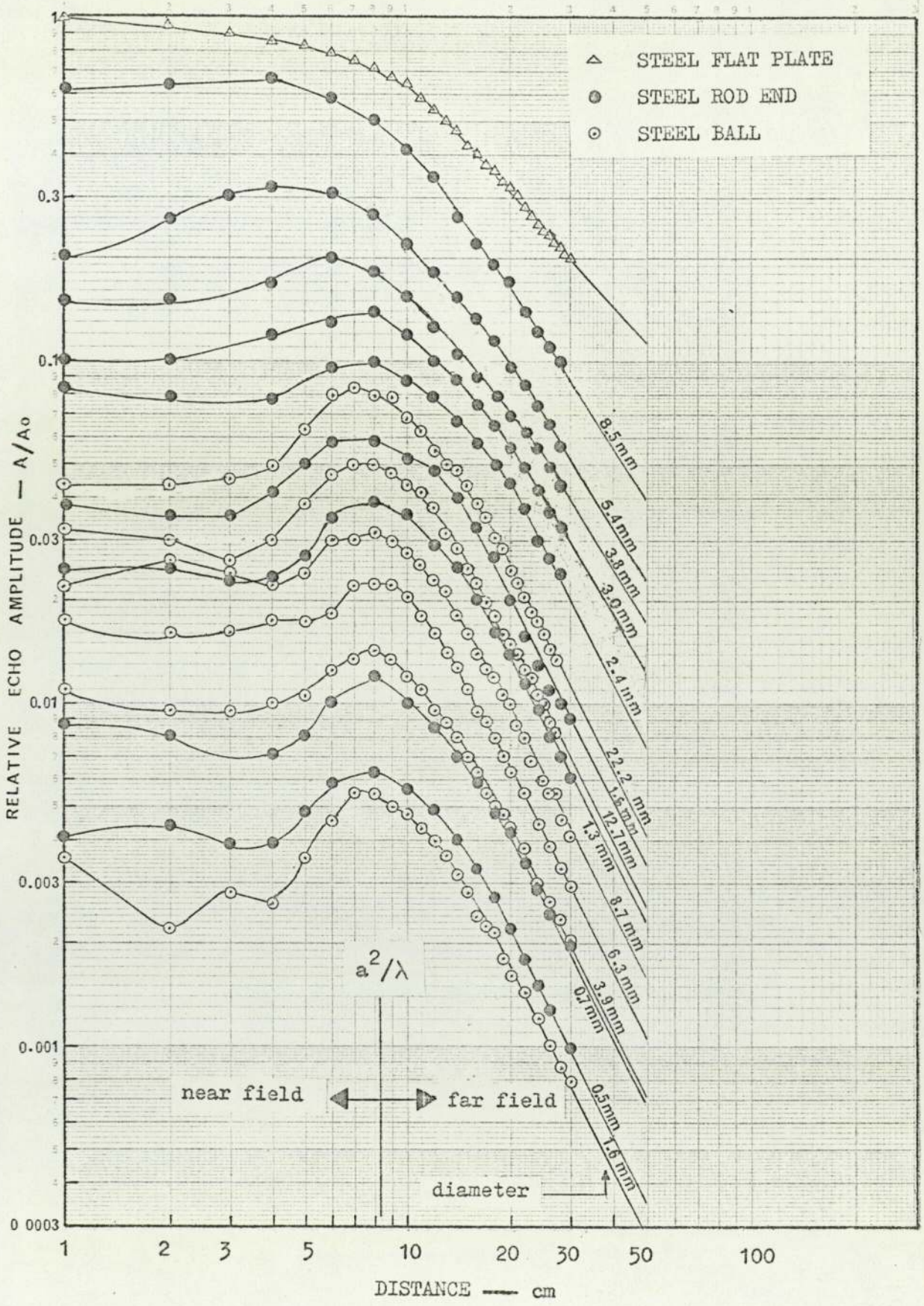


Fig. 3.9. Relative echo amplitude versus distance for spherical, circular and large flat targets - measured in water on the axis of a 5 MHz transducer of 10mm diameter.

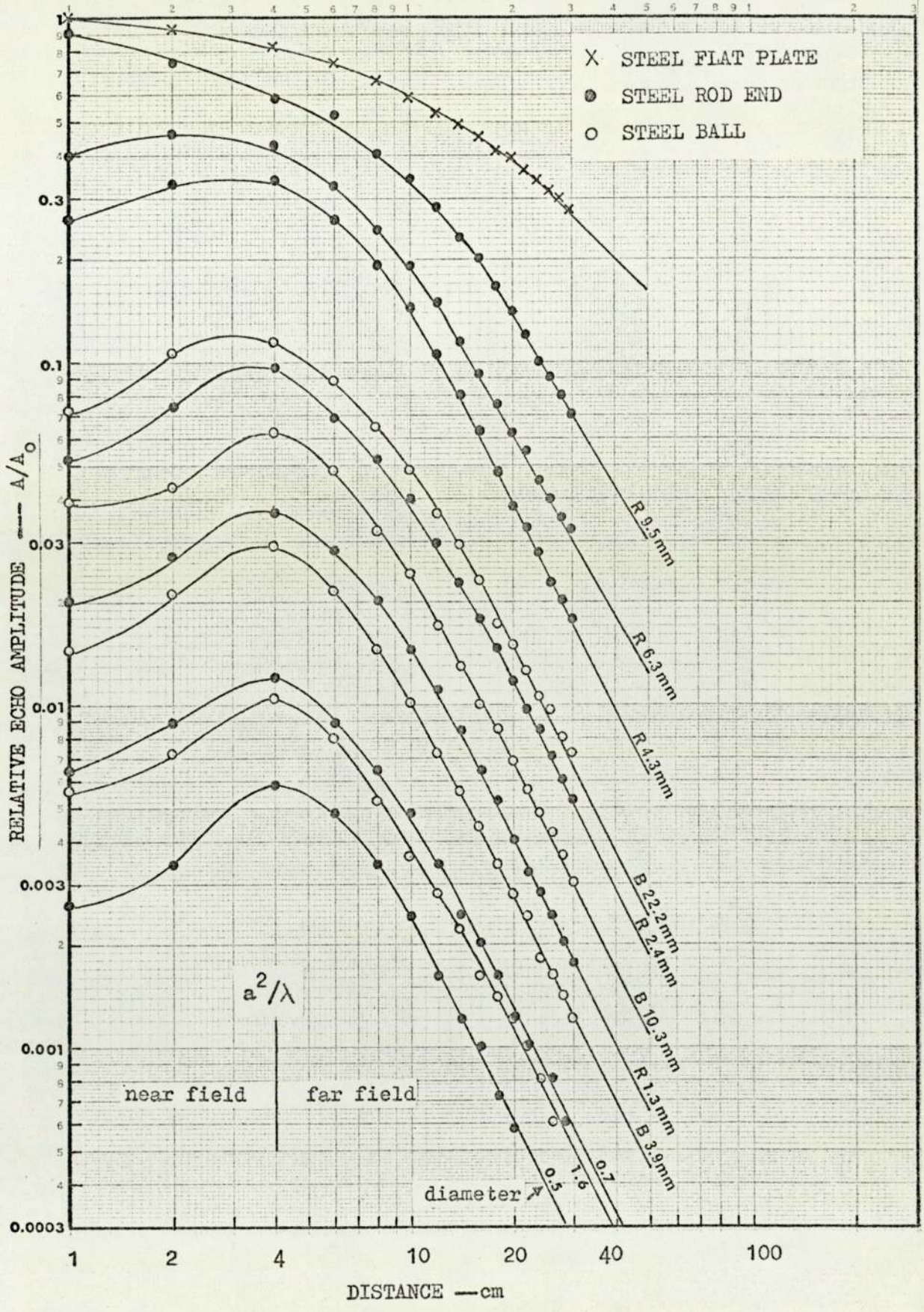


Fig. 3.10. Relative echo amplitude versus distance for spherical, circular and large flat targets for 2.5 MHz transducer of 10mm diameter.

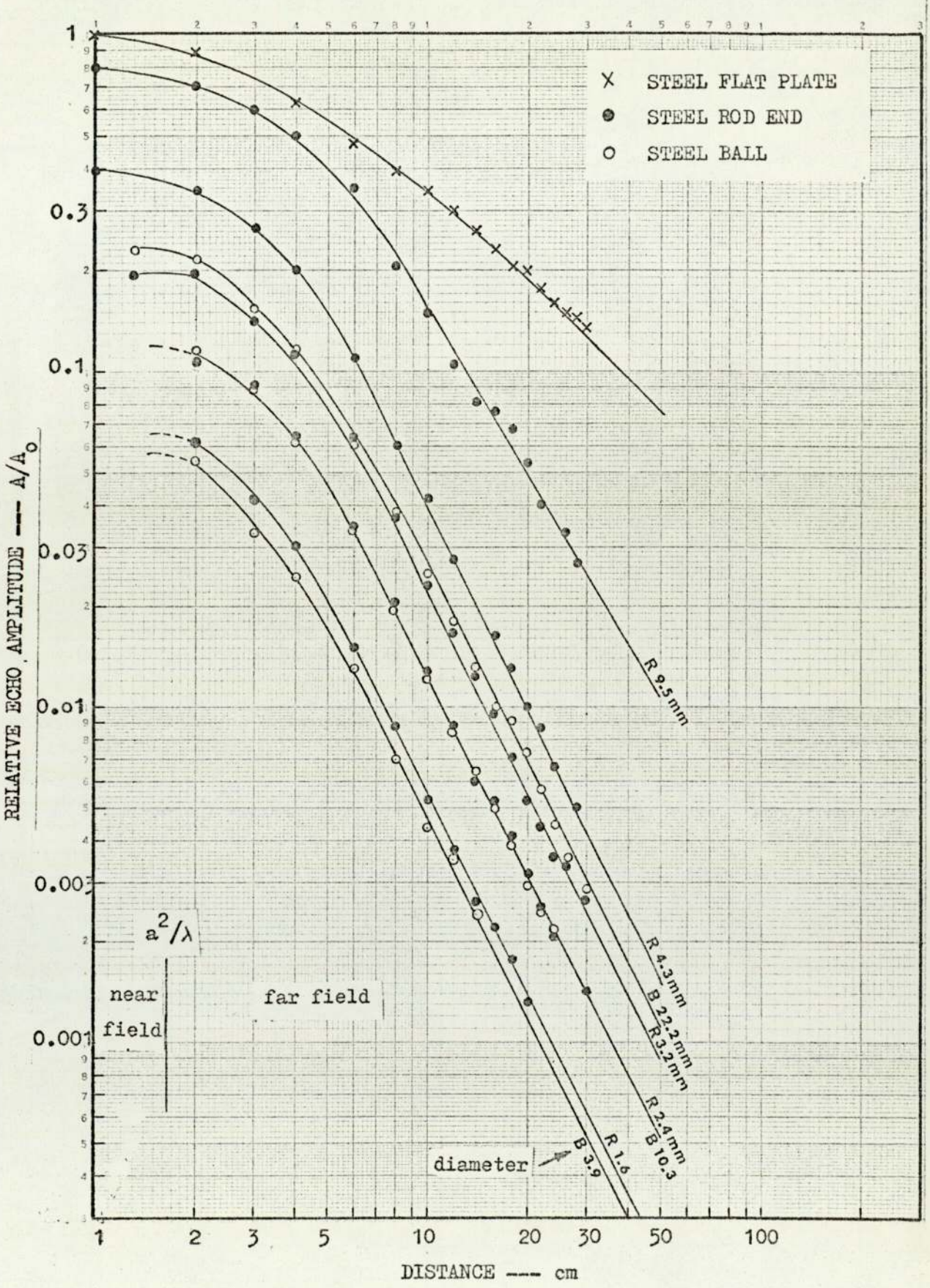


Fig. 3.11. Relative echo amplitude versus distance for spherical, circular and large flat targets for 1 MHz transducer of 10mm diameter.

In Fig. 3.9(4.1MHz) the curves for rod ends of small diameters (less than 2.4mm) and for all the spheres (of diameter up to 22.2mm) have a maximum at the end of the near field. At large distances they become almost straight lines with a gradient of-2 ie the echo amplitude is proportional to $1/r^2$. This is explained by equations (3.16) and (3.19). From Fig. 3.9 it is realised that for rods with diameters larger than 2.4mm the curves will eventually reach a gradient of -2 at distances greater than 30cm. Figs.3.10 and 11 show that the same gradient is obtained at shorter distances even for large targets, due to a smaller $k(=2\pi f/c)$ and thus smaller values of x.

### 3.3.1 Target Size and Frequency Effects

Theoretical predictions and experimental results for the echo amplitude show that the amplitude depends on the incident wavelength or the frequency. When $a/r(ka')^{-\frac{1}{2}}<0.5$ the echo amplitude from a sphere is proportional to fa' (product of radius and frequency). Equation (3.19) can be written as

$$\frac{A}{A_o} = \frac{\pi}{2} e^{-2\alpha r} \left(\frac{a^2}{cr^2}\right) (fa')$$

For similar conditions in the case of flat circular targets, ie when $kaT/r<0.5$, equation (3.16) changes to

$$\frac{A}{A_o} = \pi^2 e^{-2\alpha r} \left(\frac{a}{cr}\right)^2 (fT)^2$$

which is proportional to $f^2T^2$.

In Fig. 3.12 experimental values of $A/A_o$ for the spherical targets at distances 10, 20 and 30cm are plotted against the diameter $d_s(=2a')$. The results for sphere and circular targets, this time using the three transducers, are also shown in Fig. 3.13.. Good agreement between the

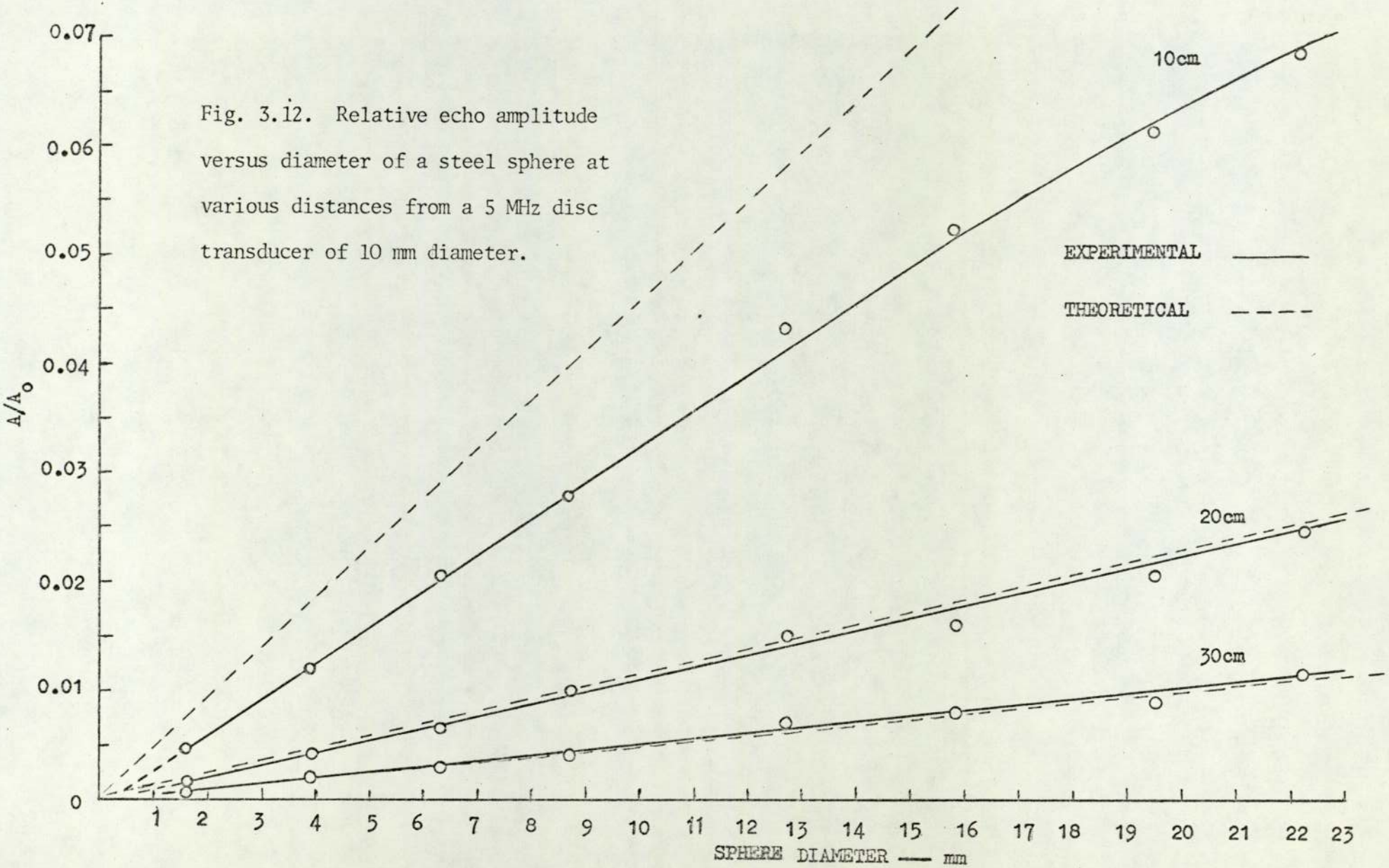


Fig. 3.12. Relative echo amplitude versus diameter of a steel sphere at various distances from a 5 MHz disc transducer of 10 mm diameter.

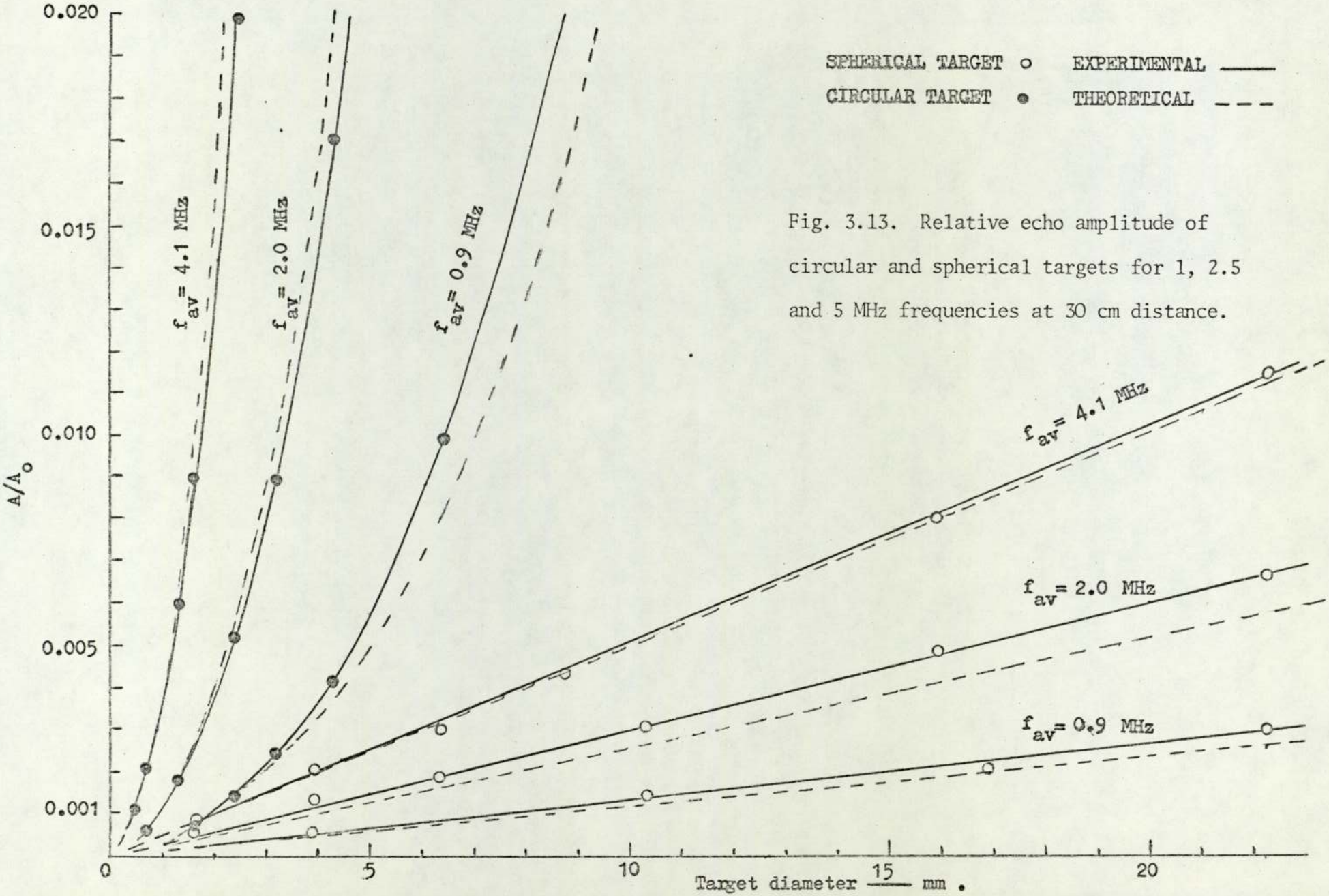


Fig. 3.13. Relative echo amplitude of circular and spherical targets for 1, 2.5 and 5 MHz frequencies at 30 cm distance.

theory and the experimental results for the far field is achieved when the average frequency of the pulse is used.

The three solid lines in Fig. 3.14 show the experimental results for the relationship between rod diameter $d_r$(=2T) and sphere diameter $d_s$ for the same echo amplitude. From equation (3.14) the theoretical relationship is

$$d_r^2 \simeq \frac{c}{\pi} \frac{d_s}{f_{(av)}}$$

where $d_r$ is the diameter of the effective reflecting area, c the sound velocity in the liquid and $f_{(av)}$ the average frequency of the short ultrasonic pulse employed. The theoretical relationship is represented in Fig. 3.14 by three dotted lines for the three frequencies (0.9, 2.0 and 4.1 MHz).

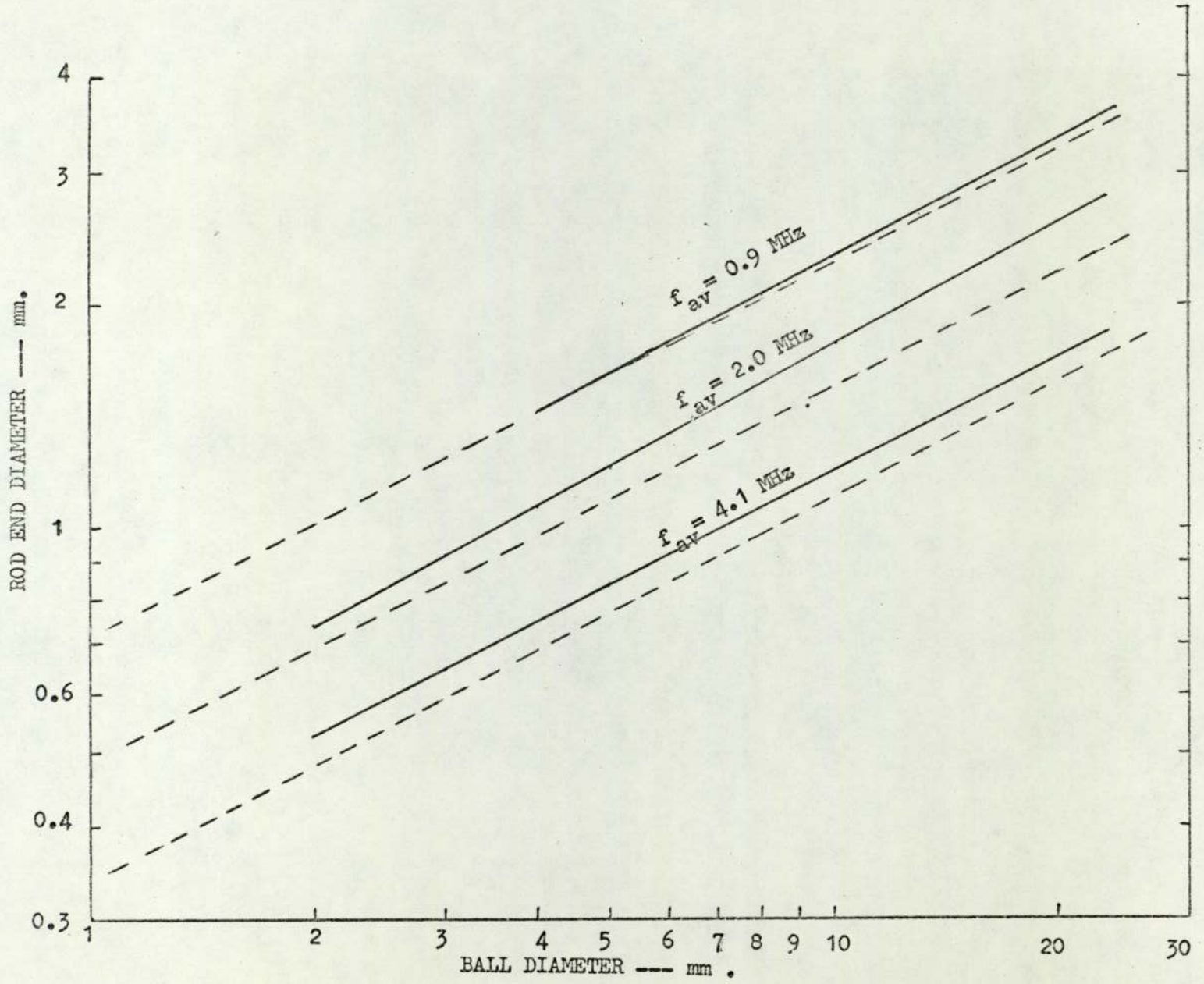


Fig. 3.14. Circular target diameter equivalent to spherical target diameter for equal echo amplitude.

# CHAPTER 4

# EFFECT OF DIAPHRAGM ON PERFORMANCE OF TRANSDUCER

## 4.1 INTRODUCTION

In the transmission of ultrasonic waves into an electrically-conducting or corrosive liquid, the transducer has to be protected by a metal buffer. For the sodium pool the transducer is mounted onto the outside of the pool and the sound pulse enters the liquid through a steel diaphragm. It is essential when using this method to choose the correct diaphragm thickness, due to its effect on the amplitude and the duration of the echo pulse.

The transmission process of continuous acoustic waves through an immersed plate is well known[38]. If a plate of thickness d and acoustic impedance $z_2$ is immersed in liquid of acoustic impedance $z_1$, the transmission coefficient is given by:

$$T = \left[ 1 + \frac{1}{4} \left( \frac{Z_1}{Z_2} - \frac{Z_2}{Z_1} \right)^2 \operatorname{Sin}^2 \frac{2\pi d}{\lambda} \right]^{-\frac{1}{2}} \qquad (4.1)$$

where $\lambda$ is the wavelength of sound in the plate. The transmission is a maximum when $d = 0, \lambda/2, 2\lambda/2$, etc and minimum when $d = \lambda/4, 3\lambda/4$, etc. Experimental results for a steel plate immersed in water reveal that at the maxima the plate shows almost complete transmittance. Equation (1) is for continuous longitudinal waves and so is valid only for a burst of oscillations which has a duration much longer than twice the transit time across the plate. In this case, the equation gives only the amplitude of the steady state region of the transmitted burst, which is expanded in length.

Similar findings are expected for the steel diaphragm which protects the transducer against the liquid, although the diaphragm separates two regions of unequal impedance. The transducer is coupled to the diaphragm with a thin film of a suitable paste. In order to generate a short pulse of ultrasonic waves, the transducer is shock-excited by a transient voltage but the diaphragm has a considerable effect on the duration of the transmitted pulse. The effect can be analysed by studying the interference of multiple reflections[40] in the diaphragm. It will be shown that for thin diaphragms a thickness of odd multiples of the quarter wavelength produces pulses of shorter duration, which are more desirable in the pulse-echo technique.

The experimental results with water and liquid tin, using a 5 MHz PZT transducer and a number of diaphragms, are presented in this chapter. The test results for a 4.6 MHz disc of lithium niobate brazed to a steel diaphragm are also given.

## 4.2 MULTIPLE REFLECTIONS IN THE DIAPHRAGM

If a long pulse of ultrasonic waves with a steady amplitude is incident on the surface of the metal diaphragm, as shown in Fig. 4.1, part of the wave will be transmitted into the diaphragm. On arrival at the opposite side, part of it will be transmitted into the liquid behind the diaphragm and part will be reflected back to the lower side. The latter will again be divided at the lower side, at which some of the energy will be absorbed into the transducer assembly and the rest will be reflected back. The continuation of the process is shown in Fig. 4.1 with the aid of a set of rays on the upper side of the diaphragm, at which the intensity decreases from one ray to the next.

Because each ray will have travelled a different distance, the rays on the upper side may be out of phase. In order to determine the phase

differences between the rays, the path traversed by a pair of successive rays, such as rays (1) and (2), must first be evaluated. Let d be the thickness of the diaphragm, and $\lambda$ the wavelength of sound in the diaphragm. The difference in these acoustic paths is equal to 2d. If this path difference is a whole number of wavelengths, rays (1), (2), (3), etc will be in phase and will give a maximum amplitude. Thus, the condition is

$$d = m\lambda/2$$

where m = 1, 2, 3 ...

Using a for the steady amplitude of the incident wave, r and r' for the reflection coefficients at the upper and lower surfaces of the diaphragm respectively, and t and t' for the transmission coefficients, the following geometrical progression is obtained for the maximum amplitude of the waves transmitted into the liquid. The attenuation within the diaphragm is assumed to be small

$$A_{MAX} = att' [1 + rr' + (rr')^2 + (rr')^3 + ...] \qquad (4.2)$$

Since r and r' are necessarily less than 1, the progression has a finite sum equal to

$$A_{MAX} = a \frac{tt'}{1-rr'}$$

Thus, the amplitude will build up from att' (the amplitude of the first cycle) to the maximum att'/(1-rr'), as in Fig. 4.2, and will then decay to zero after the last oscillation of the incident pulse has been cut off. The rate of increase in the amplitude on the front edge of the transmitted

pulse depends on r, r' and the diaphragm thickness. For example, the measured value of rr' for a steel diaphragm fixed to a tank of water and coupled to a PZT ceramic transducer with a coupling film is about 0.65. This means that the amplitude will build up to $A_{MAX}$ after almost 5 cycles for a diaphragm of $\lambda/2$ and after 10 cycles for a diaphragm of $\lambda$. A diaphragm of thickness $m\lambda/2$, therefore, increases the duration of the pulse and the maximum amplitude occurs in the middle.

When the diaphragm thickness is such that

$$d = (2m + 1)\lambda/4$$

rays (2), (4), (6), etc, shown in Fig.4.1, will be out of phase with rays (1), (3), (5), etc. Since ray (1) is more intense than (2), (3), (4) and so on, the combination of these rays produces complex waves for the first few oscillations of the transmitted pulse, then reaches an amplitude which is smaller than att' (the amplitude of the first cycle). This is described by the following progression :

$$A_{MIN} = att' [1 - rr' + (rr')^2 - (rr')^3 + ...] \qquad (4.3)$$

The finite sum is equal to

$$A_{MIN} = a\left(\frac{tt'}{1+rr'}\right)$$

It is therefore concluded that a diaphragm of thickness $(2m + 1)\lambda/4$ produces a short pulse, which is preferable for the majority of pulse-echo techniques (in which the detection of the first cycle of an echo between some unwanted echoes is required).

By changing the thickness of the diaphragm from $\lambda/4$ to $2\lambda/4$ or from $3\lambda/4$

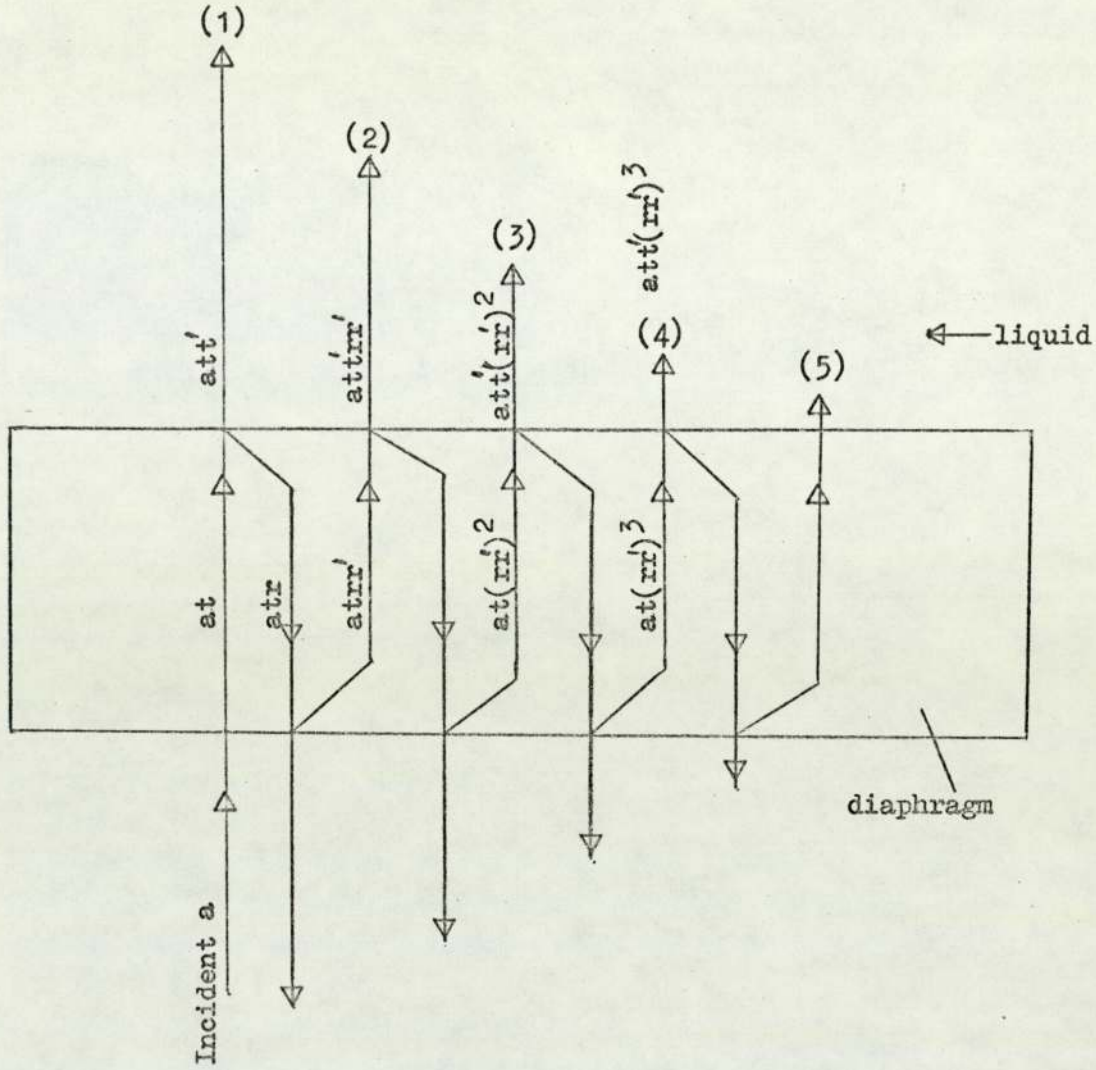


Fig. 4.1. Multiple reflections of ultrasonic waves in a metal diaphragm.

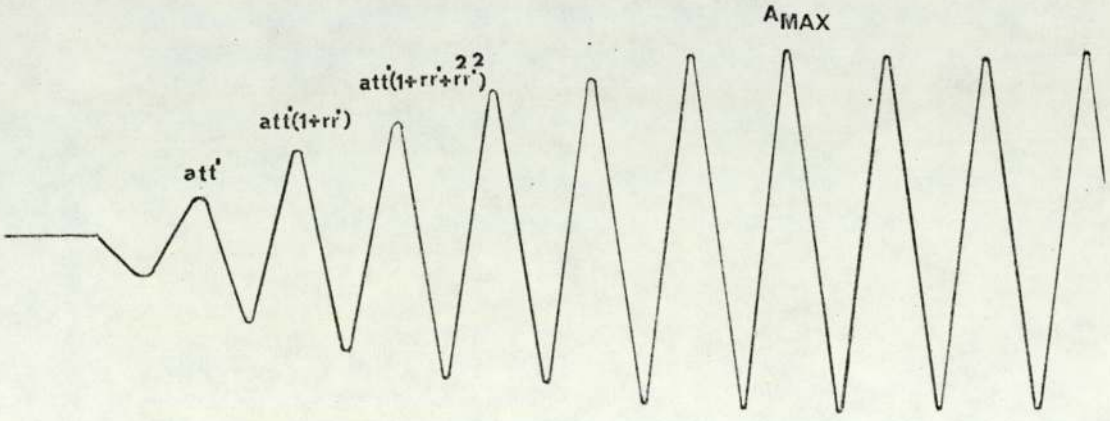


Fig. 4.2. Amplitudes of waves transmitted through a diaphragm of $\lambda/2$ thickness.

to $4\lambda/4$ and so on (or equally by changing the frequency for a fixed diaphragm thickness), the amplitude of the middle part of the long pulse varies from $A_{MIN}$ to $A_{MAX}$ at each stage of the thickness. The ratio between $A_{MAX}$ and $A_{MIN}$, $\frac{1+rr'}{1-rr'}$, depends on the values of r and r' : r and r' vary between 1 and 0. By decreasing r and r' towards zero, $A_{MIN}$ will increase to $A_{MAX}$.

If the transmitted pulse is reflected back from a target, the echo received by the transducer will be expanded further, due to the second transmission through the diaphragm. The progression of the amplitude on the front edge of this echo signal for $d = m\lambda/2$ is

$$A_{MAX} = a(tt')(t_1 t_2)\ K\ [1 + 2rr' + 3\ (rr')^2 + \ldots] \quad (4.4)$$

where $t_1$ and $t_2$ are the transmission coefficients at the two boundaries of the diaphragm, K is a coefficient less than unity, due to attenuation of sound in the liquid. Fig. 4.3 shows the typical shape of an echo signal for various diaphragm thicknesses, when $rr' = 0.65$.

So far, the effect of the diaphragm has been considered for long pulses. For short pulses and relatively thick diaphragms the echo signal may either have a fluctuating amplitude with a long duration or be composed of a number of separate pulses close together. Fig. 4.4 shows the effect of a thick diaphragm which sends a series of pulses into the liquid for only one transient voltage ; similarly, the echo signal has a number of pulses. There is no interference between the transmitted pulses, but when they return to the transducer multiple reflections occur again. Now, there is an interference between each pulse entering the diaphragm and the multiple reflections of the preceding pulses. Only the first echo pulse is free from interference and therefore reproduces the initial pulse. Due to the interference between the succeeding pulses, the amplitude of

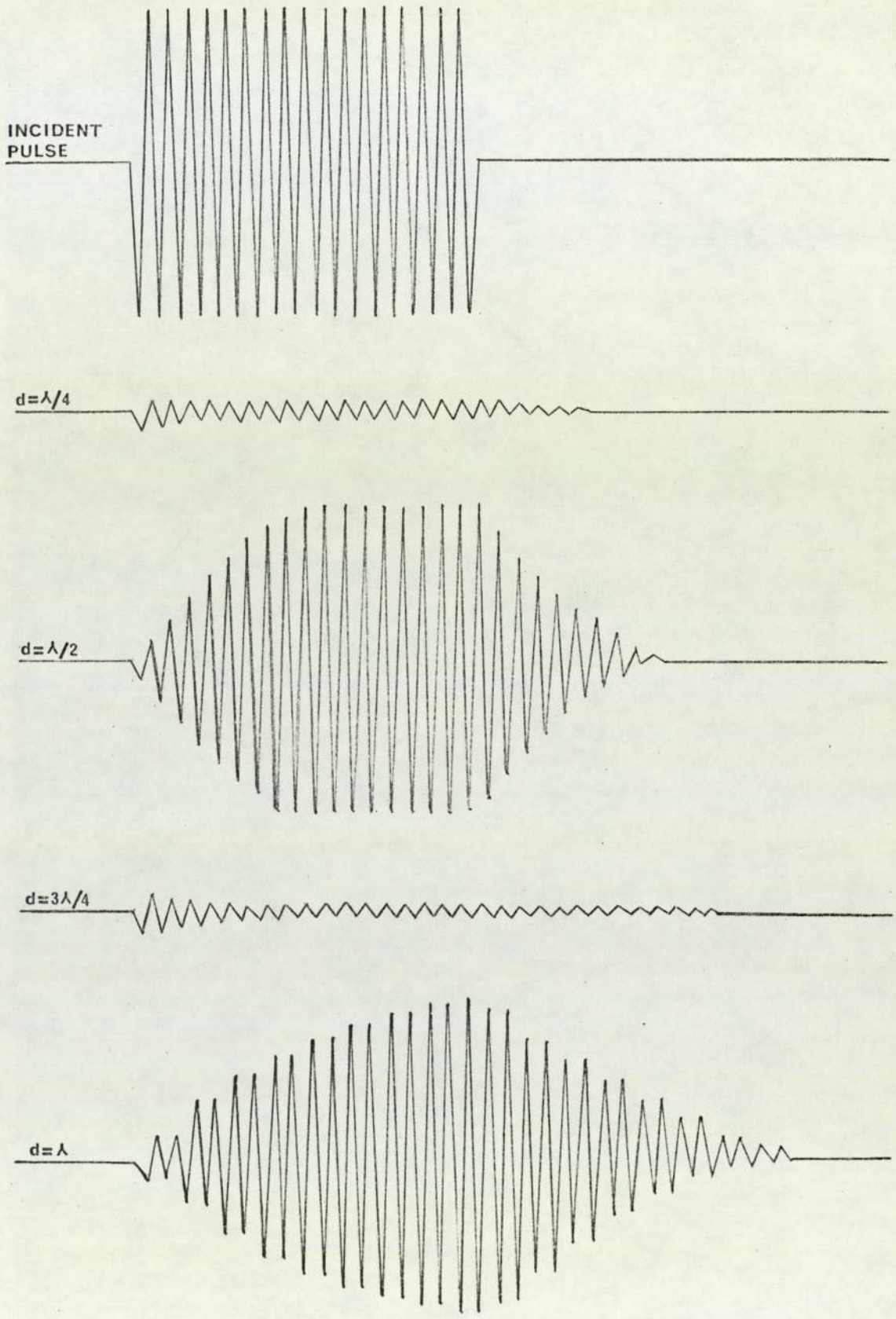


Fig. 4.3. Echo signals in liquid, using reversible transducer with metal diaphragm of various thicknesses, when $rr' = 0.64$.

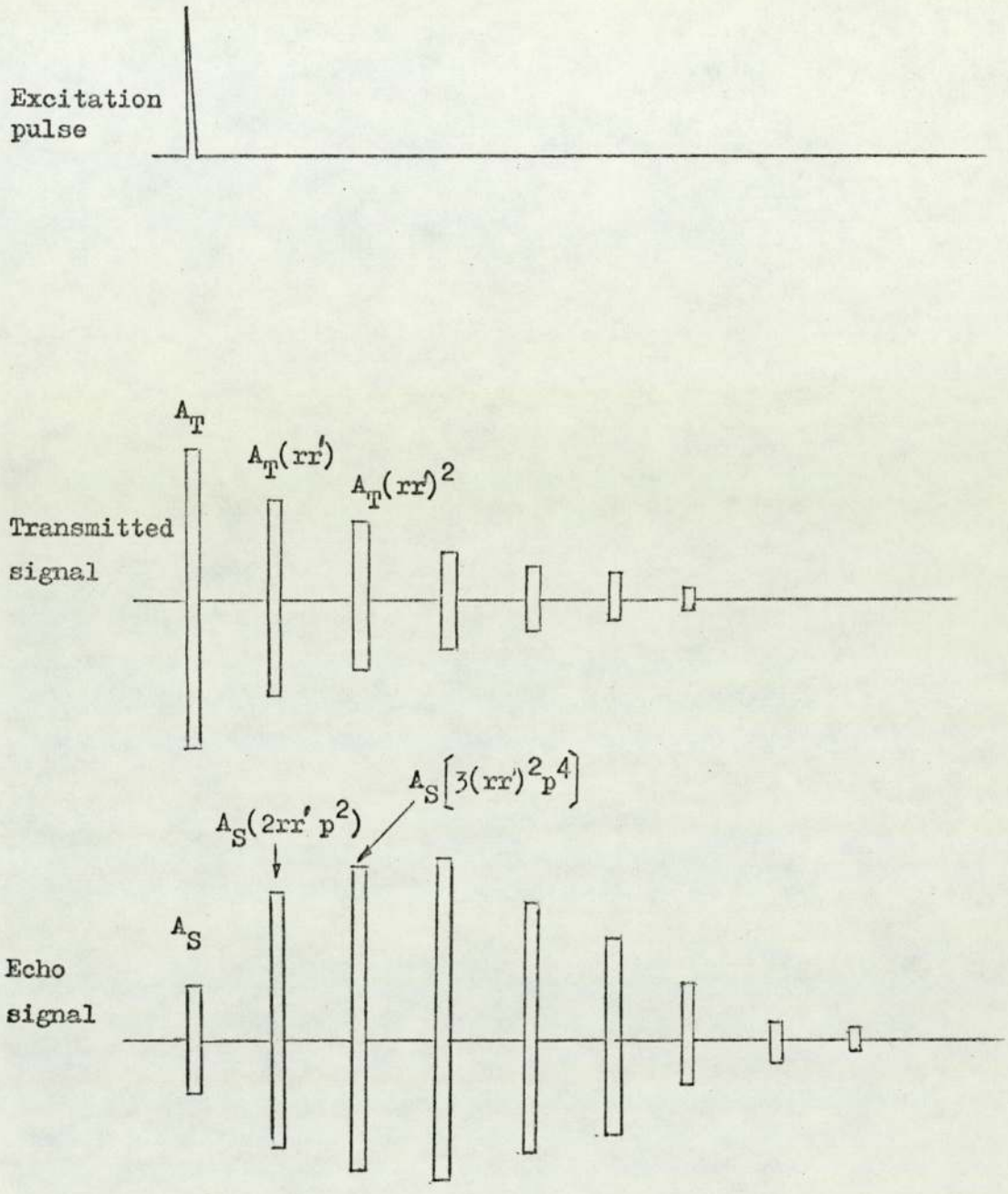


Fig. 4.4. Echo pulses received through a thick diaphragm for only one excitation of the transducer.

the first few will build up to a maximum and decay to zero for the rest. The relative amplitudes of these pulses can be given as follows:

$$A_s,\ A_s\ [2rr'p^2],\ A_s\ [3(rr')^2p^4],\ \ldots \qquad (4.5)$$

where $A_s$ is the amplitude of the first echo pulse and p, due to the attenuation of the ultrasonic pulse travelling in the metal diaphragm from one side to the other in each period of successive reflection, is a coefficient (numerically less than unity).

## 4.3 EXPERIMENTAL DEMONSTRATION OF THE EFFECT

### 4.3.1 In Water

A 5 MHz disc transducer of 10mm diameter, type PZT5A, was fixed at the base of a container filled with water. The arrangement was the same as that designed for the sodium pool. A flat target was placed normal to the beam axis at a distance of 15cm. The transducer was driven by an excitation voltage pulse and thus produced a typical short echo, as shown in Fig. 4.5a, in the absence of a metal diaphragm.

The effects produced on the echo signal by diaphragms of various thicknesses from 0.5mm to 5mm were investigated. Figs. 4.5b, c, d, and 6a and b show photographs of 5 echo signals for 5 selected diaphragm thicknesses of 0.52, 0.89, 1.12, 1.42, 1.65mm, being nearly equal to $2\lambda/4$, $3\lambda/4$, $4\lambda/4$, $5\lambda/4$, $6\lambda/4$ respectively. (The measured value of the wavelength in the diaphragm, made of Incoloy 800, for 5 MHz is 1.11mm). As is shown in Figs. 4.5 and 6 the amplitude and the duration of the echoes are greatest when the thicknesses are $\lambda/2$, $\lambda$ and $3\lambda/2$, and are smallest when the thicknesses are $3\lambda/4$ and $5\lambda/4$.

In this experiment, r and r' are the reflection coefficients at the diaphragm-water interface and the diaphragm-transducer interface

respectively; the value of rr' was estimated to be 0.65 which was measured in an experiment using the relative amplitudes of the multiple pulses in a thick diaphragm (10mm). According to equation (4.4), for a long incident pulse with a steady amplitude the echo amplitude will reach a maximum value after almost 10 successive reflections. Thus, for a diaphragm of thickness $\lambda/2$, the amplitude of the 10th cycle will be the greatest, as will be the amplitude of the 20th cycle for a diaphragm of thickness $\lambda$, see Fig. 4.3. Since the incident pulse, shown in Fig. 4.5a, had no steady amplitude, the amplitude built up to a maximum after 5 cycles with a diaphragm of thickness $\lambda/2$, after 8 cycles with a diaphragm of thickness $\lambda$ and after 14 cycles with a diaphragm of thickness $3\lambda/2$. Figs. 4.5 and 6 also show that the echo signal duration is more extended when the diaphragm is thicker.

Fig. 4.6c shows the echo signal when a thick diaphragm is used ie 5mm. Due to successive interval reflections in the thick diaphragm, the echo signal consists of several separate pulses close together. The first pulse in Fig. 4.6c is the actual echo from the target. The remaining pulses are the spurious echoes due to interference between the successive pulses reflected from both sides of the diaphragm, and they are attenuated and distorted progressively. As is expected, the amplitudes of the second and even the third pulse in Fig. 4.6c are greater than that of the first one.

### 4.3.2 In Molten Tin

The experiment described above was repeated with two diaphragms of thicknesses 1.18mm and 0.84mm, using molten tin at a temperature of 280°C in a specially-designed vessel (described in Chapter 7). Typical echoes are shown in Figs. 4.7a and 4.7b. A comparison of the signals obtained in water and tin using a diaphragm of approximately $\lambda/2$ shows that the echo has a shorter duration in tin. This is due to the reduction in r, the reflection coefficient at the tin-diaphragm boundary. With sodium at 250°C the

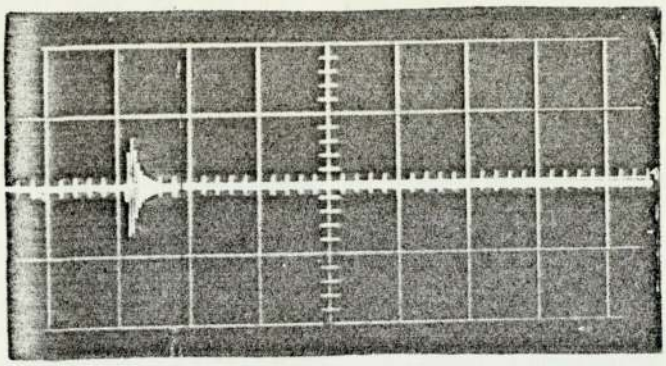

2 V/CM, 4 μsec/CM

(a) without using metal diaphragm.

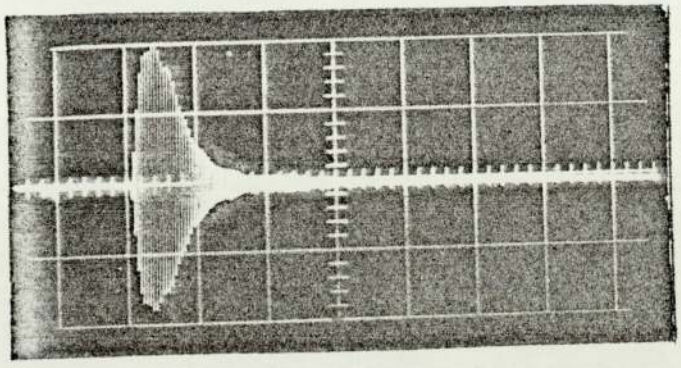

0.5 V/CM, 4μsec/CM

(b) diaphragm thickness = 0.52mm, $\lambda/2$ = 0.55mm

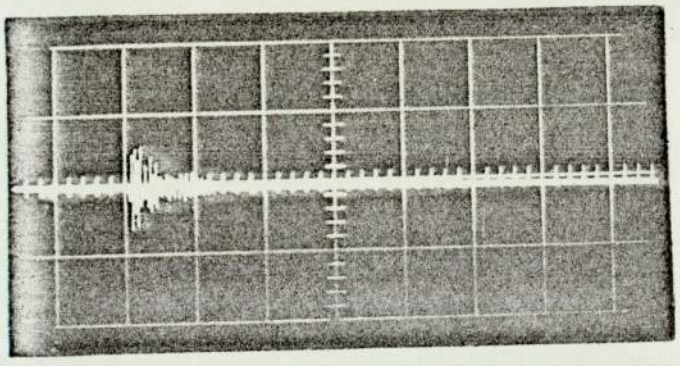

0.5 V/CM, 4μsec/CM

(c) diaphragm thickness = 0.89mm, $3\lambda/4$ = 0.84mm

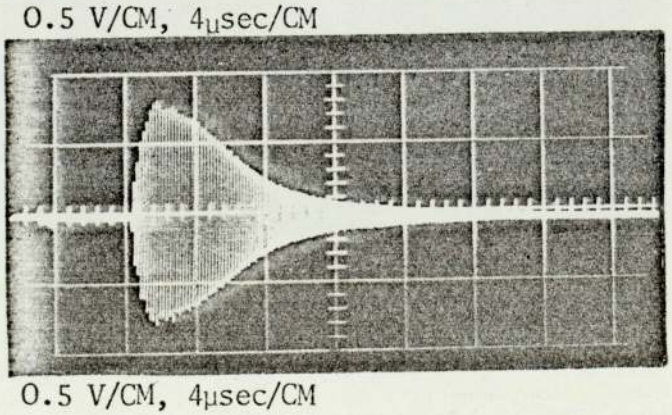

0.5 V/CM, 4μsec/CM

(d) diaphragm thickness = 1.12mm, $2\lambda/2$ = 1.11mm.

Fig. 4.5. Echo signals from target in water, using reversible transducer with steel diaphragm of various thicknesses.
Transducer frequency = 5 MHz.

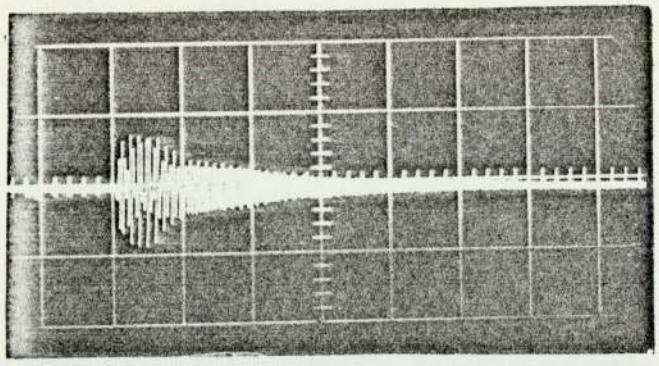

(a) diaphragm thickness = 1.42mm

$5\lambda/4$ = 1.39mm.

0.5 V/CM, 4μsec/CM

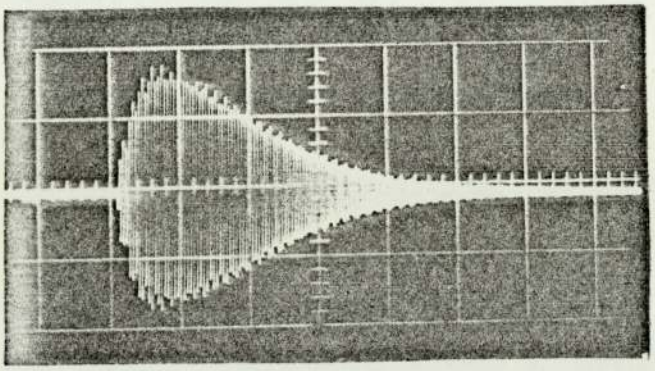

(b) diaphragm thickness = 1.65mm

$3\lambda/2$ = 1.66mm.

0.5 V/CM, 4μsec/CM

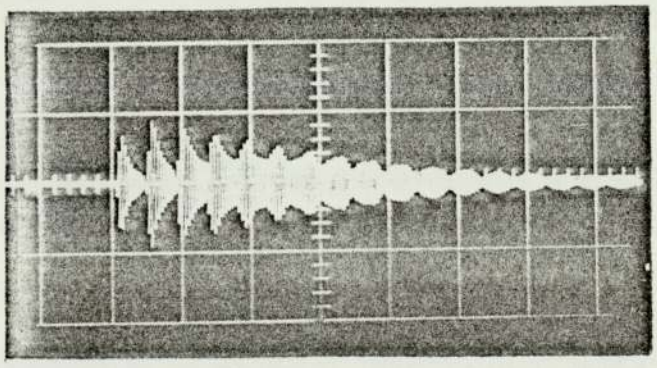

(c) diaphragm thickness = 5mm.

0.5 V/CM, 4μsec/CM

Fig. 4.6. Echo signals from target in water, using reversible transducer with steel diaphragm of various thickness.

Transducer frequency = 5 MHz.

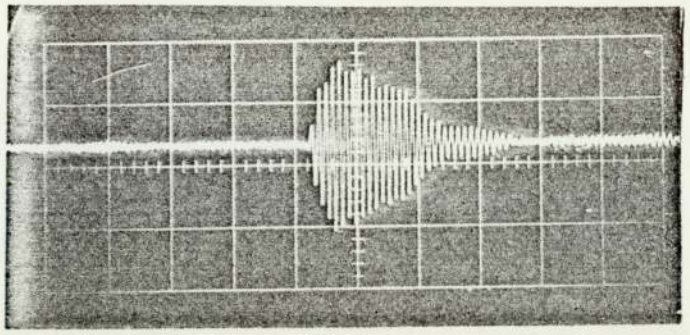

(a) diaphragm thickness = 1.18mm., $2\lambda/2$ = 1.11mm

1 V/CM, 2$\mu$sec/CM

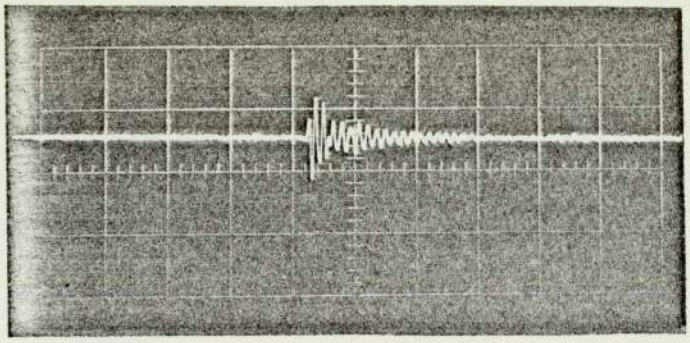

(b) diaphragm thickness = 0.84mm., $3\lambda/4$ = 0.84mm

1 V/CM, 2$\mu$sec/CM

Fig. 4.7. Echo signals from a flat target in molten tin at 408$^{o}$C, using a 5 MHz PZT5A coupled to a steel diaphragm.

reflection coefficient of the diaphragm-sodium boundary is expected to be 0.91 which is similar to that of the diaphragm-water interface. The echo signal in Fig. 4.7b shows again that a diaphragm of $3\lambda/4$, even for liquid tin with higher acoustic impedance, effectively produces a signal shorter than that for a diaphragm of thickness $2\lambda/2$.

## 4.4 HIGH-TEMPERATURE TRANSDUCER (LITHIUM NIOBATE)

In order to investigate the characteristics of lithium niobate as a pulsed ultrasonic transducer for use with sodium at high temperatures, several crystals brazed to steel rods and diaphragms were tested.

The lithium niobate was available in the form of discs which were obtained by slicing a single-crystal rod perpendicular to its axis. Each disc had a diameter of about 10mm and a resonance frequency in the range 4-5 MHz before bonding. Successful acoustical bonding was achieved, however, with only a few of the samples. Fig. 4.8 was obtained with a disc bonded to the flat end of a steel circular - section rod, and shows the typical short echo signals received from the extremities of the rod. The crystal was driven by an excitation voltage pulse and the amplifier used had a frequency band width of 3 to 6 MHz. The first signal in Fig. 4.8a is the result of direct reflection off the end face of the rod, while the second echo is the result of reflections of the diverged beam, first off the side surface and then off the end face. These two signals are identical but of opposite polarity, showing that the second echo is the result of two reflections on the rod boundaries. A number of spurious echoes were received after the first signal, due to the waveguide modes in the rod with longitudinal-shear wave conversion, shown in Fig. 4.8b.

Among the crystals brazed to the diaphragms, only one had a good acoustical joint. Its fundamental frequency was 4.6 MHz and the thickness of the diaphragm was 0.7mm, almost equal to $\lambda/2$ in steel. This transducer was

mounted at the base of the vessel described in Chapter 7. Fig. 4.9a shows the echo signal from a flat target in water. The amplifier had a frequency band of 1 to 3 MHz. The same echo produced the signal shown in Fig. 4.9b when a frequency band of 4 to 6 MHz was used for the amplifier. This shows that the brazed crystal with a good acoustical bonding has a wide frequency spectrum. A comparison between Figs. 4.8 and 4.9 reveals that although the crystal generates a short pulse in a rod, it rings for a long duration when it is bonded to a diaphragm of thickness $\lambda/2$.

To test the transducer at high temperature, the vessel was filled with solid tin and heated up slowly. No echoes were at first detected, even after all the tin had been melted; throughout this test the molten tin was not isolated from the surrounding air. The absence of echoes was due to the non-wetting of the diaphragm surface by the molten tin, giving a transmission coefficient of zero at the diaphragm-tin boundary. The echo appeared after the temperature had been held at 350°C for some hours and improved with time to the condition in Fig. 4.9c; the signal strength was low and suffered from background noise. The signal had a short duration, which, to some extent, was expected because of the smaller reflection coefficient of the diaphragm-tin boundary. The short duration and weakness of the signal were partly attributed to non-uniform wetting on the diaphragm face and further to the cracks which appeared in the crystal at these higher temperatures and which may have changed the frequency spectrum of the transducer.

Cracks observed in lithium niobate discs have been attributed to the unmatched temperature coefficients of expansion of the disc and the brazing/diaphragm material. Research on the bonding of lithium niobate to Incoloy 800 and steel has been undertaken at the AERE Harwell[34], and it is expected that a suitable transducer for working up to 600°C will be available for the sodium pool in due course.

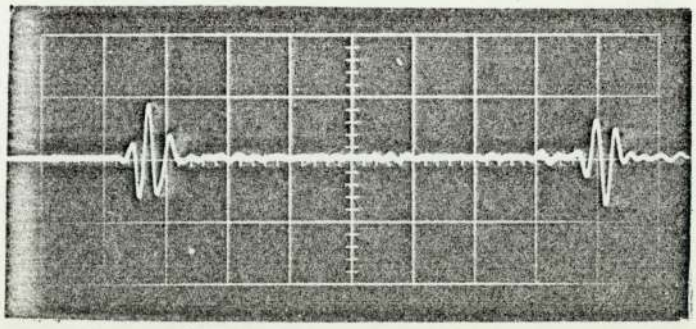

(a)

0.2 V/CM, 1μsec/CM

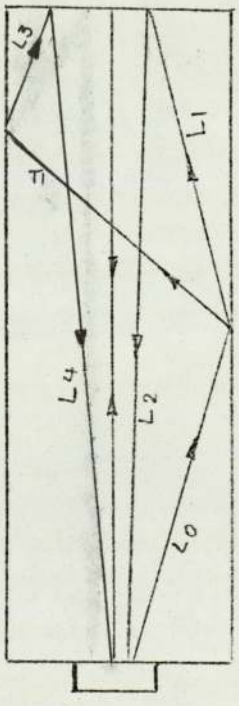


(b)

Fig. 4.8. Echo signals received from the extremities of a steel rod by a 4.4 MHz lithium niobate crystal brazed to one end.

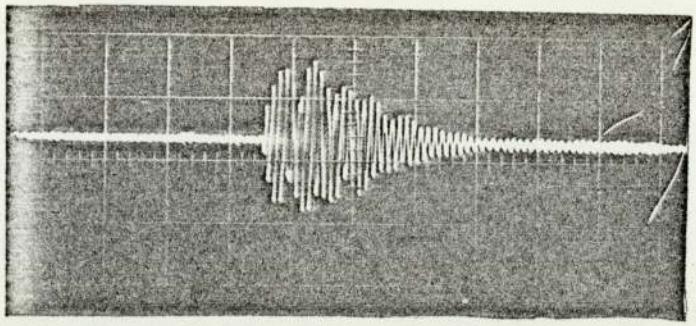

0.5 V/CM, 4μsec/CM

(a) In water, band pass frequency of amplifier = 2 MHz.

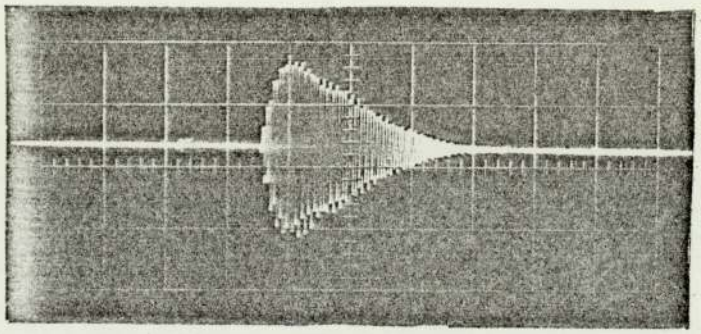

0.5 V/CM, 4μsec/CM

(b) In water, band pass frequency of amplifier = 5 MHz.

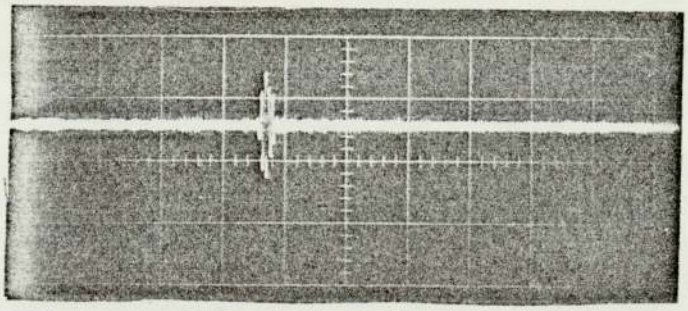

0.1 V/CM, 4μsec/CM

(c) In tin at 350°C, band pass frequency of amplifier = 5 MHz.

Fig. 4.9. Target echo signals produced by a 4.6 MHz lithium niobate crystal brazed to a stainless steel diaphragm of 0.7mm thickness.

## 4.5 EFFECT OF DRIVE PULSE

As was shown previously, the presence of a steel diaphragm between the transducer and the liquid can cause undesirable changes in the shape of the echo signal. These changes include an increase in its duration, slow rise and slow decay in amplitude. The particular shape of the echo produced by diaphragms of $d = m\lambda/2$ causes the signal-to-noise ratio of the pulse echo technique to deteriorate.

The first solution to the problem is to choose a diaphragm of thickness $3\lambda/4$, $5\lambda/4$ or $7\lambda/4$. But due to the typical shape of the pulse generated by the shock-excited transducer, it is sometimes difficult to find a diaphragm thickness which produces an echo of the desired short duration (see Figs. 4.5c and 4.6a).

An alternative solution is to modify the excitation of the transducer so that the summation of the multiply-reflected pulses in the diaphragm does not build beyond the first cycle. This can be achieved by changing the shape of the drive-pulse, as described below.

In order to obtain an echo signal with good efficiency the transducer has to be excited by a drive-pulse of fast rise time corresponding closely to the fundamental frequency of the transducer. If the decay time of the drive pulse is similarly fast, the transducer is excited by both the leading edge and the trailing edge. The ultrasonic pulse, therefore, is a superposition of the two waves generated by the two edges. The resultant waveform will depend on the relative phases of the two waves[47]. If the phases are equal, a long resonant type signal is generated; if they are in reverse phase, a short, well-defined pulse is produced. The shape of the drive-pulse can therefore be suited to a particular diaphragm thickness, so that the waves generated by the trailing edge can cancel to some extent the multiple-reflections in the diaphragm.

In a particular experiment, the required drive-pulse was generated by a circuit which uses a fast-switching thyristor (see section 5.4.2). It had an amplitude of 400 volts, a rise time of less than 80 nsec., and a variable decay time (from 50nsec.). By changing the decay time (or effectively the pulse width), ultrasonic pulses of various shapes were produced. For a given diaphragm it was possible to find a suitable drive-pulse for which the amplitude of the echo signal dropped to a minimum after the first 2 or 3 cycles. For example, Fig. 4.10 shows two echo signals obtained with a diaphragm of 1.22mm thickness when two different drive-pulses were used. The pulses show a marked contrast; the duration was reduced from about 16μs in (a) to 1μs in (b), although, as anticipated, the initial few cycles are not appreciably different.

The test was repeated with molten tin at 280°C, using a diaphragm of 1.18mm. Fig. 4.11 shows the improvement in the echo signal by choosing a suitable drive-pulse.

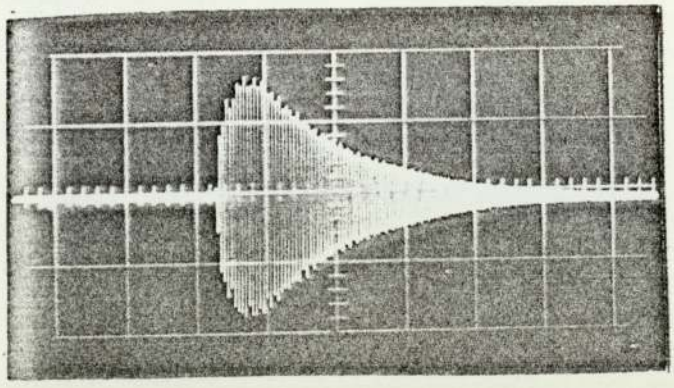

2 V/CM, 4μsec/CM

(a) Applying a shock pulse of 400v and 0.1μsec pulse width.

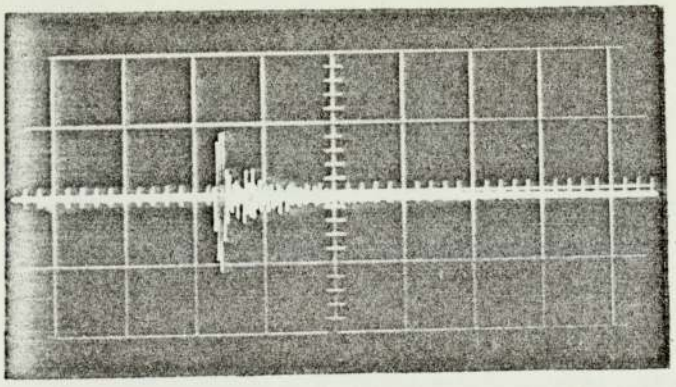

2 V/CM, 4μsec/CM

(b) Applying a shock pulse of 400v and 0.24μsec pulse width.

Fig. 4.10. Echoes from a target in water, using a 1.11 steel diaphragm at transducer, applying two different shock pulses for transducer excitation.

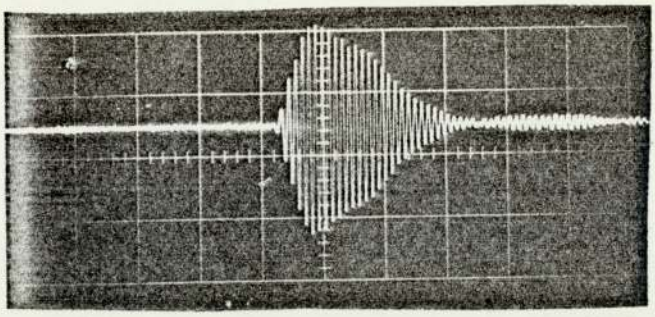

(a)

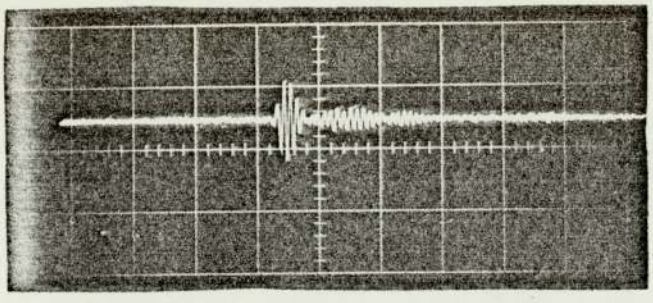

(b)

Fig. 4.11. Echoes from a target in tin at 280°C, using a 1.18mm steel diaphragm at transducer, applying two different shock pulses for transducer excitation.

# CHAPTER 5

# THE PULSE-ECHO TECHNIQUE

## 5.1 INTRODUCTION

The ultrasonic system for the measurement of bubble growth is described with the aid of the simplified functional block diagram shown in Fig. 5.1. The technique consists of the rapid processing and recording of the change in transit time of the bubble echo. The 5 MHz transducer employed at the base of the pool is energised by an excitation voltage pulse from the transducer drive unit which is triggered by the pulse generator. The transducer, which is used both as a transmitter and receiver, is driven at a pulse repetition frequency (PRF) of between 1 and 10 KHz. The echo signals received from the bubble interface are fed to an amplifier with a variable gain of 20 dB to 40 dB, in order to reach sufficient amplitude for signal processing.

In the pool, the transmitted ultrasonic pulse travels from the transducer to the target (the bubble nucleation rod) through a stable temperature gradient of between 250°C and 900°C in the cooling tube. The corresponding velocity of the sound travelling through this passage varies from 2440 to 2100 $msec^{-1}$. The time interval between the transmission signal and the first echo signal from the target rod corresponds to the acoustic delay in the return of the echo to the transducer. The time interval (or the transit time of the echo) is constant, provided that the temperature gradient remains stable. This time interval changes when a bubble grows at the end of the target rod. The time change, which is proportional to the bubble boundary movement, is detected and converted to a voltage analogue by the electronic system. The analogue output, which indicates directly the bubble size, is displayed on a storage oscilloscope.

The resolution of the system in detecting small echo signals from the

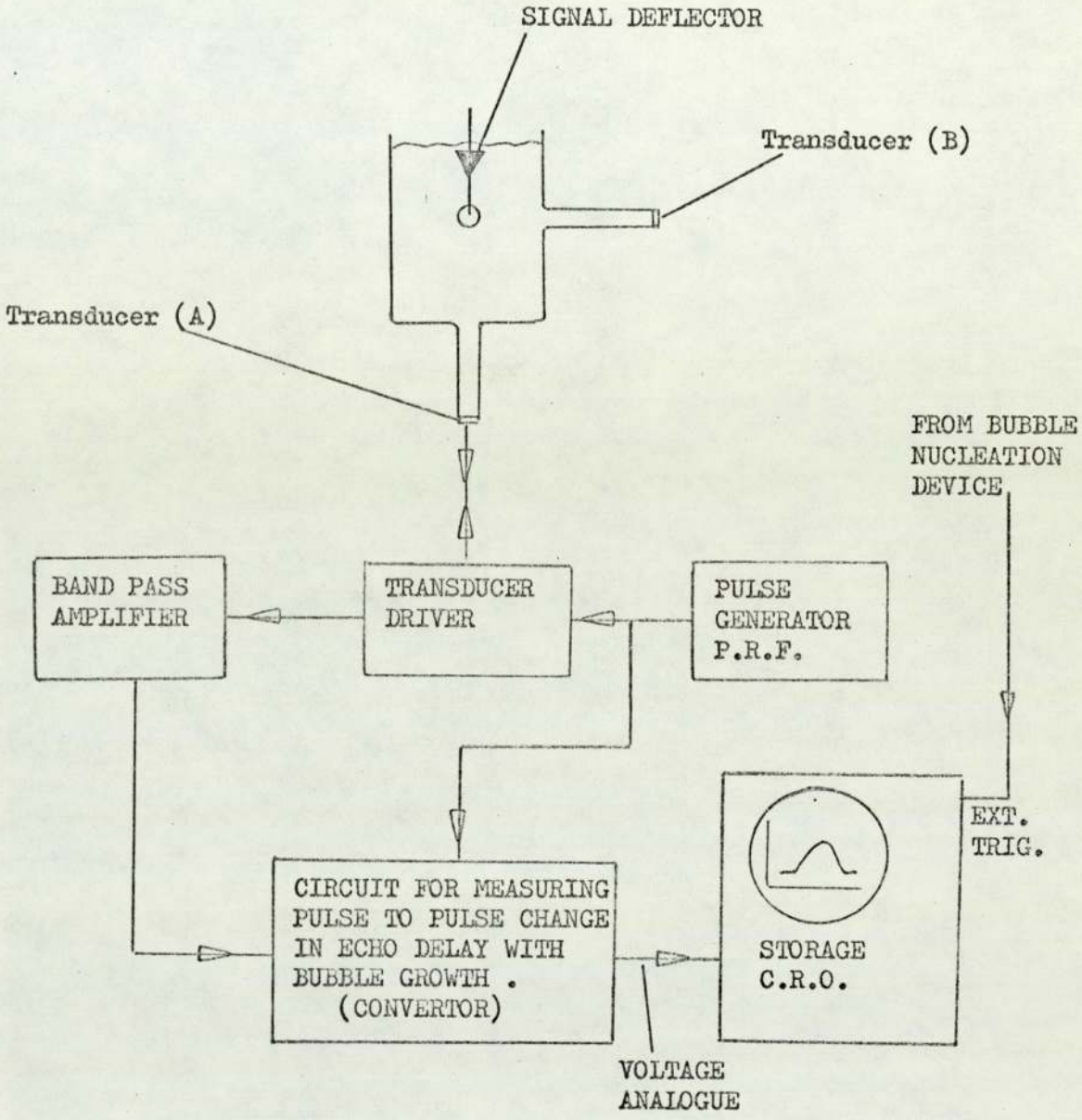


Fig. 5.1. Simplified functional block diagram of ultrasonic monitor for measuring bubble interface movement in sodium pool.

bubble at its initial stage of growth is limited by the interference from the unwanted echo signals (due to reverberation) received from different boundaries in the pool. This is made even worse by the effect of the steel diaphragm at the transducer face on the echo signal shape. The reverberation problem is explained in detail in section 5.3 and a solution is given.

In order to avoid further background reverberation, the side transducer (B in Fig. 5.1) has to be used only as a receiver for detecting the echoes from the bubble when the incident beam is generated from transducer A. An identical electronic system to the one used for the transducer at the base of the pool is employed for transducer B. Difficulties are expected due to convection in the side cooling tube when the temperature in the pool is 900°C and transducer B is kept below 250°C. In order to eliminate this convection, it may be necessary to use a shorter cooling tube, which in turn will necessitate the development of the high-temperature transducer (lithium niobate) for the mounting in the side tube.

## 5.2 THE TRANSDUCER PROBE

A schematic diagram of the transducer probe designed for the sodium pool is shown in Fig. 5.2. The transducer is a disc of PZT 5A ceramic of diameter 10mm, thickness 0.4mm and natural frequency 5 MHz. It is mounted between a stainless steel disc fixed on a ceramic button and the steel diaphragm at the base of the cooling tube. The diaphragm protects the piezoelectric material from the liquid sodium, and has to be thick enough to prevent the diaphragm from bending at the sodium temperature.

The PZT disc is coupled to the diaphragm with a very thin and uniform film of a coupling paste (ZGM, Krautkrämer) with a continuous operating temperature up to 280°C. The PZT disc is also held in position and damped by a spring behind the ceramic button. The back face of the PZT disc is electrically connected by a length of high temperature coaxial cable

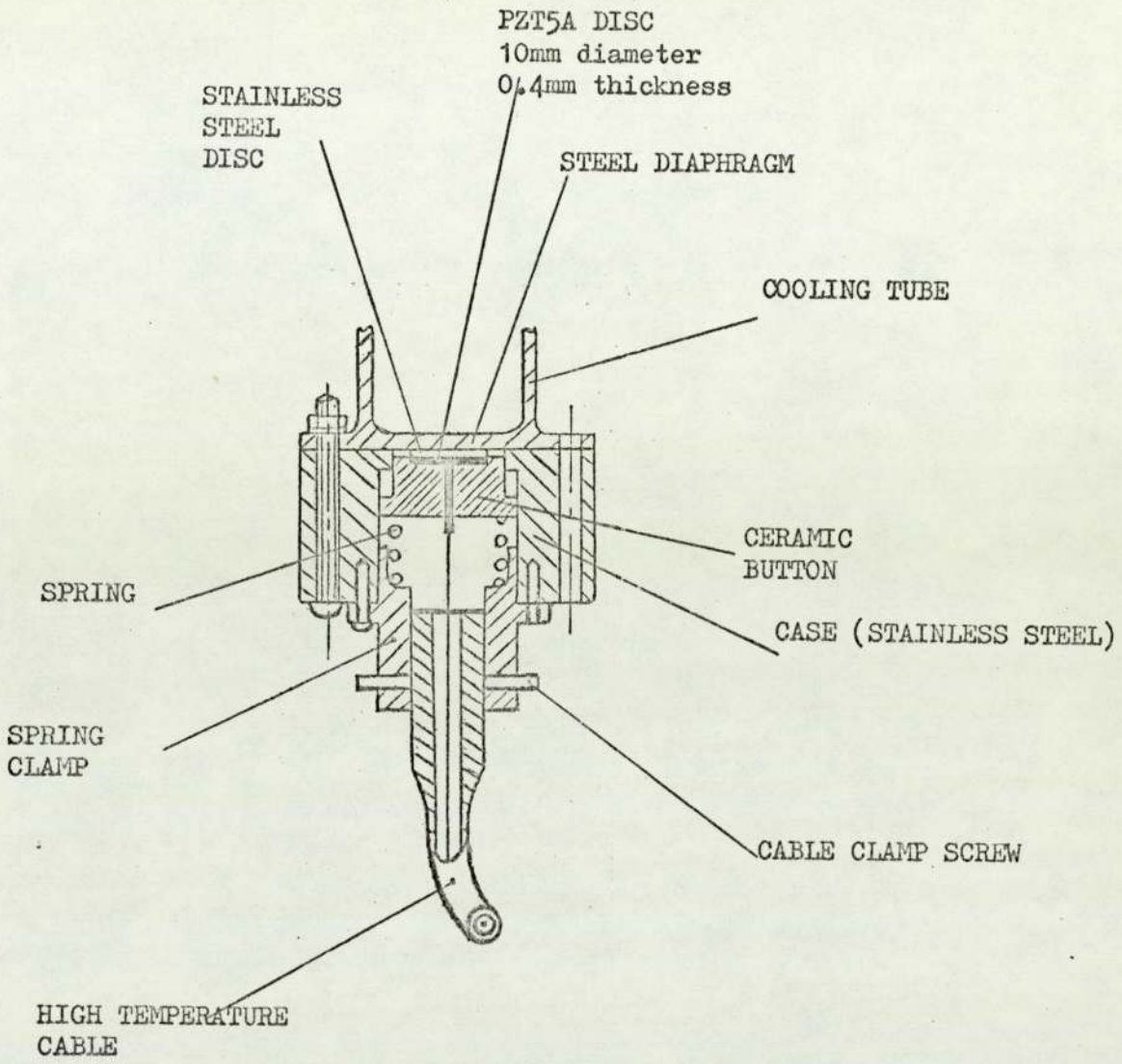


Fig. 5.2. Construction of the transducer probe mounted on the cooling tube of the sodium pool.

(mineral insulated, stainless steel sheathed cable-Pyrotenax) to the transducer driver unit. Its front face is connected to the grounded side of the circuit by the diaphragm. The required length for the lead is about 10m, since the electronic instrumentations must be set up away from the sodium pool assembly.

## 5.3 BACKGROUND REVERBERATION

Any acoustic energy which is returned to the receiving transducers without being reflected by the target rod is called reverberation. The unwanted echo signals caused by reverberation in the pool are from two different sources: (i) reflections from the liquid surface and the pool walls (ii) scattering of sound in the bulk of the liquid metal due to non-homogeneous properties resulting from suspended particles and gas bubbles[47]. The liquid surface reverberation produces the strongest unwanted echoes. These appear as a series of signals and are due to successive reflections between the liquid surface and the bottom walls of the pool. The reverberation signals are expanded in duration after each reflection off the transducer face, due to the effect of the steel diaphragm separating the transducer from the liquid (chapter 4). Tests in the pool filled with water showed that the echo from the target rod was followed by many unwanted signals, mostly from the liquid surface. The target echo was used as a reference signal which allowed the position of the bubble to be deduced. The unwanted signals, on the other hand, limited the repetition rate of the measuring system; they interfered greatly with the target echo when the PRF was higher than 1 kHz. This was improved considerably by using the techniques for reducing the effect of the diaphragm on echo signal expansion.

### 5.3.1 Reduction of Liquid Surface Reverberation

A significant reduction in unwanted echo signals from the liquid surface was also achieved when a signal deflector was used. This consists of a

metal cone which is concentric with the target rod and placed near the liquid surface (Fig. 5.1). The cross-section of the cone was greater than that of the incident beam so that the cone was able to scatter most of the incident energy away from the beam. Only a small part of the incident energy is scattered back to the transducer and received as the cone echo signal. Before re-entering the transducer zone, the scattered waves from the cone surface are attenuated in the liquid after many multiple reflections on the side walls of the container.

Actual tests using a metal cone of $100^{o}$ and 18mm diameter in the pool showed significant reduction in the level of background reverberation and even up to 3.5kHz repetition rate, the system was free from any serious interference. Higher PRFs could be used by employing the techniques for improving the echo signal shape.

## 5.4 THE ELECTRONIC SYSTEM

The block diagram in Fig. 5.3 and the waveforms diagram in Fig. 5.4 describe the sequence of operation . The numbers indicated in the first figure refer to the waveforms in the second.

For each trigger pulse supplied by the PRF generator and fed to the transducer driver, an ultrasonic pulse is transmitted into the pool. The transducer then receives some echoes which are converted to electric signals and then amplified. The circuit for measuring the change in echo delay receives two input signals, one from the PRF generator and the other from the amplifier. The pulses supplied by the PRF generator and the echo signals obtained at the amplifier output are represented in Fig. 5.4 by waveforms (1) and (2) respectively. Waveform (2) consists of the initial transmission signal $T_{T1}$ which is followed by the target echo $T_{P1}$, the cone echo $T_{C1}$ and some small reverberation signals, some of which may interfere with the echoes produced by the next transmission signal $T_{T2}$.

When a bubble has been formed at the end of the target rod, the bubble echo signal $T_{B1}$ appears before $T_{P1}$. It then moves on the time base from its initial position to position $T_{BM}$. Time $T_{BM}$ corresponds to the maximum position to which the bubble interface grows. For 10mm growth, for example, this time would be about 5μsec less than $T_{P1}$. The bubble echo signal $T_{B1}$ can be detected, provided that its amplitude is a few millivolts greater than that of the background reverberation received in the region from $T_{P1}$ to $T_{BM}$. The characteristic motion of $T_{B1}$ is identical to that of the bubble interface movement. As the bubble grows, the time difference $(T_{P1}-T_{B1})$ increases at a rate proportional to the growth rate. The variable time $(T_{P1}-T_{B1})$ is converted to a d.c. voltage step at each cycle of the PRF, as is described below.

The echo signals (waveform 2) are fed to a high speed voltage comparator, by which each signal is detected and converted to rectangular waves. Ideally, the comparator should operate as a zero crossing detector. Due to the background reverberation, however, it has to be employed as a threshold detector with a reference level of a few millivolts above the reverberation level which is higher when the PRF is increased. The unwanted echo signals situated before $T_{BM}$ and after $T_{P1}$ are checked at the comparator ouput by applying a gating pulse, waveform (3). Waveform (3) allows the comparator to detect only the fixed signal $T_{P1}$ and the moving signal $T_{B1}$. Waveform (4) shows the output signal.

The comparator output is fed to TTL logic circuits in order to detect the echo-delay variation. The function of the logic circuits is to generate a single pulse (pulse s in waveform 5) which is locked to the start of the echo signal $T_{B1}$. Pulse s is arranged to trigger a bistable circuit which is again triggered by the back edge of the gating pulse. The rectangular pulse at the bistable circuit output (waveform 6), therefore, has a width which changes in accordance with the echo-delay.

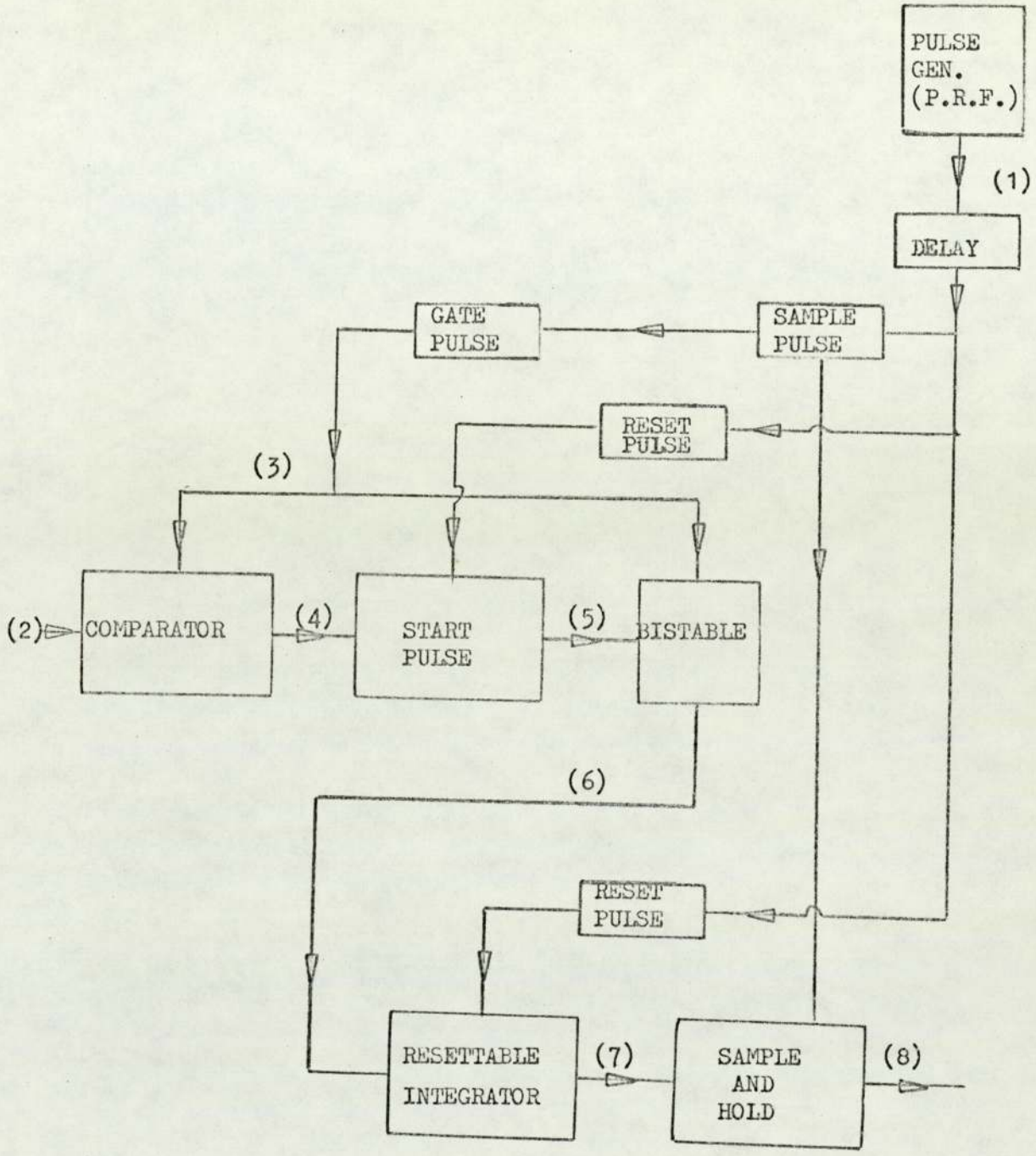


Fig. 5.3. Functional block diagram of the bubble echo converter.
The numbers on the figure refer to the wave forms of Fig. 5.4.

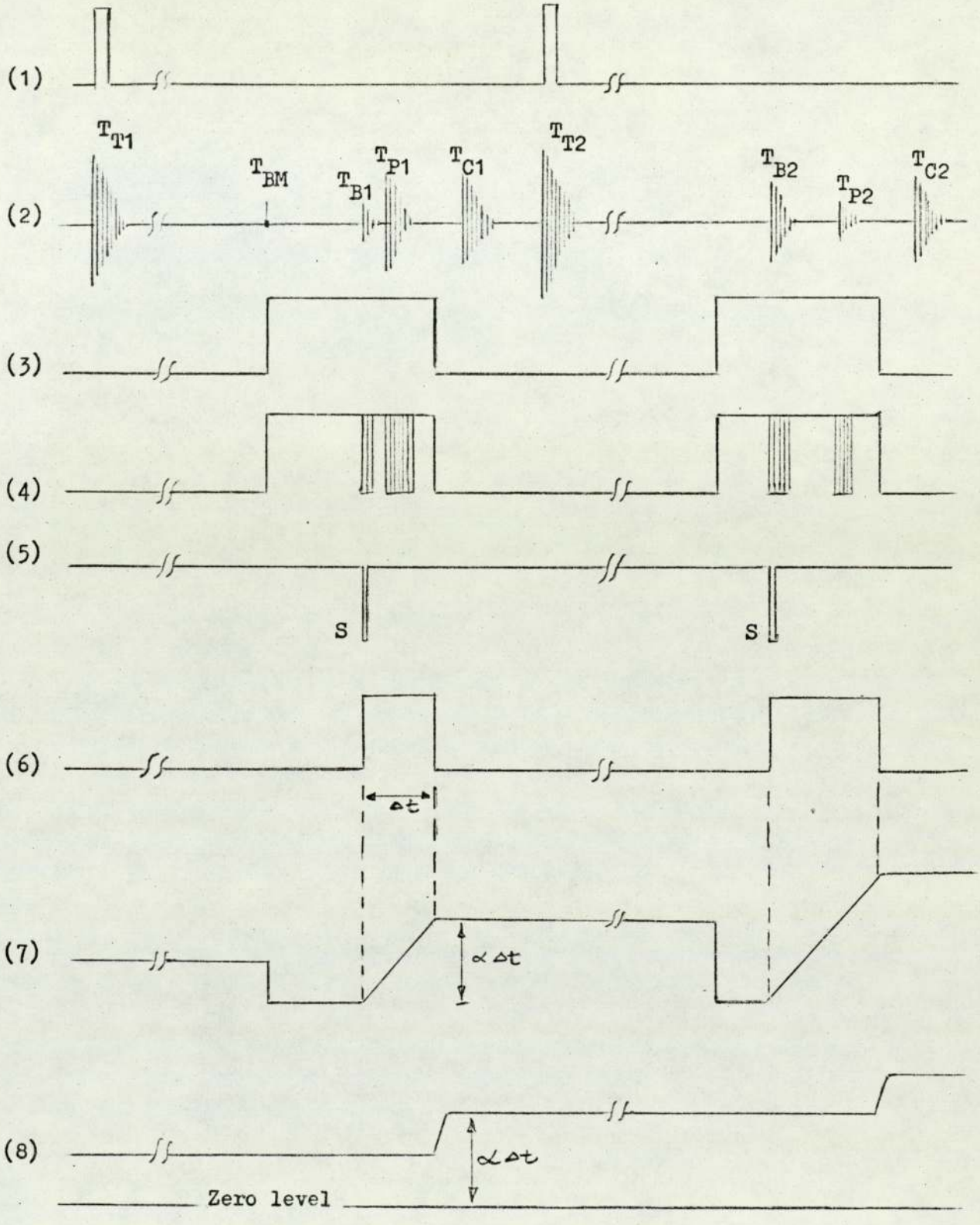


Fig. 5.4. Waveforms diagram of the ultrasonic system.

At the leading edge of pulse (6), the resettable integrator begins to charge up at a constant rate. The charging current stops at the negative going edge of pulse (6), causing the integrator to remain at a constant voltage level until it is reset to zero before the next PRF cycle. Thus, the pulse height of the integrator output (waveform 7) is proportional to the width of pulse (6).

The sample and hold unit receives the integrator output immediately after the time at which integration is complete. The d.c. voltage level of pulse (7) is sampled for a short period and is stored in order to generate an analogue voltage for recording. The change in the level of voltage output from one cycle of PRF to the next is proportional to the difference between the transit times of the two bubble echoes in the two neighbouring PRF cycles. The bubble growth, therefore, is represented by a series of voltage steps, the length of each being equal to the period of the PRF cycle. The change from one step to the next is fast and thus high repetition rates can be applied. The variation output of the voltage analogue can be displayed on a chart recorder for slow changes in echo delay and on a storage oscilloscope for fast changes, as in the case of vapour bubble growth.

### 5.4.1 PRF Generator

The PRF generator (Fig. 5.5) consists of a TTL compatible oscillator made of two cross-coupled monostable circuits (Bell et al)[48]. The charging current of the two monostables ($M_1$ and $M_2$) is provided by the constant current sources, transistors $T_1$ and $T_2$. The frequency can be varied continuously from 500 Hz to 10 kHz by changing the voltage applied to the transistors' bases through a single 20 kΩ potentiometer. The RC circuit at the B input of $M_1$ is to ensure that the oscillator starts when the supply is switched on. The oscillator output is fed to another monostable $M_3$ to form short pulses required for the transducer driver. The switch S1

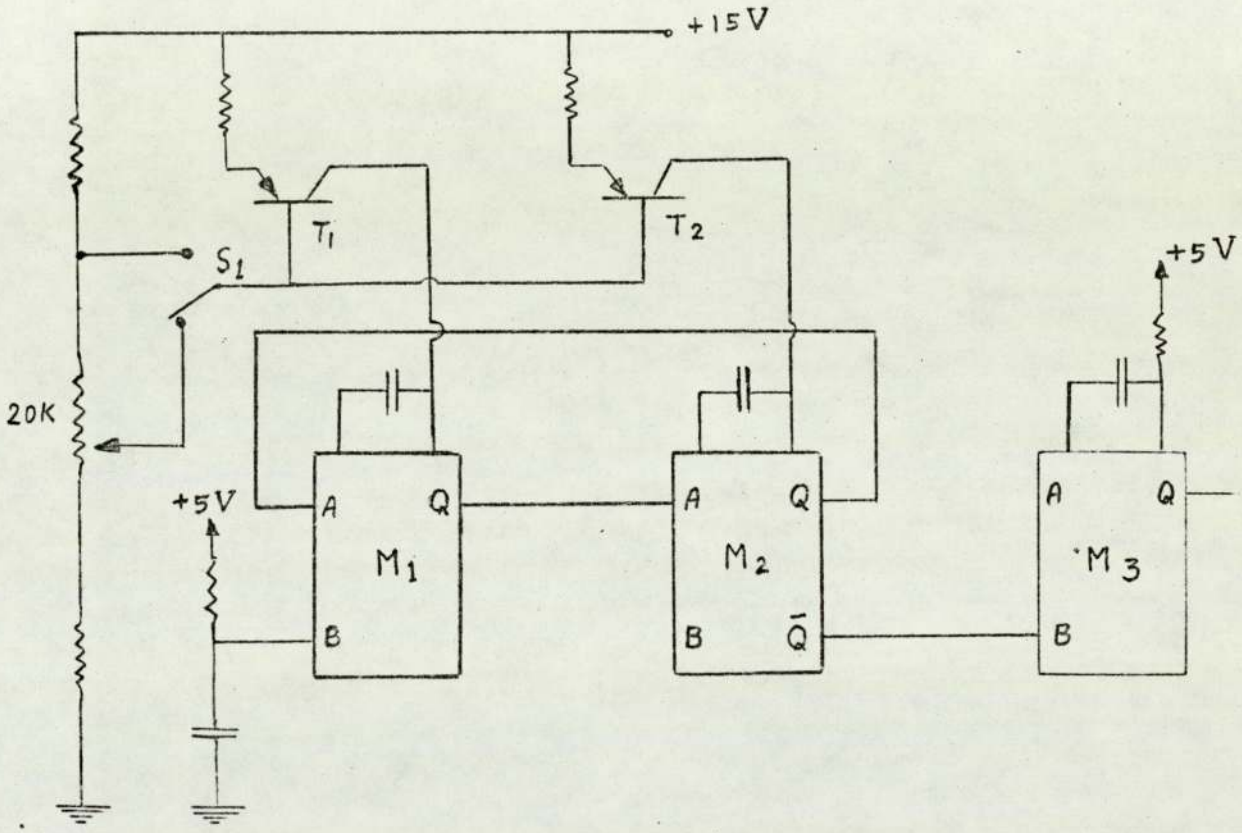


Fig. 5.5. Circuit diagram of PRF generator.

provided at the common base of $T_1$ and $T_2$ is for changing the PRF to the lowest rate without any adjustment to the potentiometer. It is required for finding the position of the target echo and for adjusting the gating pulse (waveform 3 in Fig. 5.4). The frequency stability of the oscillator used is adequate for measurements of short duration, which is the case for bubble growth measurement. However, even for a measurement of long duration a slight change in the pulse repetition period has no effect on the accuracy of the system. This is because the change in echo-delay in each cycle of the PRF is measured with respect to the time of the pulse-drive.

### 5.4.2 Transducer Driver

Excitation of piezoelectric transducers by a transient voltage pulse is one of the common methods of generating a short ultrasonic pulse. The transducer, in this way, rings at its fundamental frequency for a duration which depends on the Q factor of the system and the characteristic of the excitation pulse. The ultrasonic energy obtained per pulse depends on the amplitude and the duration of the drive-pulse. For a given amplitude, short pulses contain less energy than do longer pulses. High-voltage drive-pulses can be applied by suddenly discharging a capacitor across the transducer by means of a fast electronic switch. The typical valve-operated circuit commercially available (Diasonograph, type NE4100)[42] uses a thyratron and is capable of generating excitation pulses of about 850V with a rise time of 80 nsec. This signal has a high efficiency at frequencies around 5 to 10 MHz, since the rise time corresponds closely to that of the fundamental frequency. Myers et al[49] used an avalanche breakdown transistor for generating pulses of fast rise (10 nsec) and slow decay. The maximum amplitude using this device is under 200 volts. Furthermore, the operating life-span of the transistor is short for use in long experiments.

The circuit described here (Fig. 5.6a) uses a fast switching thyristor

(type BWT30) and is capable of generating high voltage pulses with a rise time of less than 80 nsec across a 50Ω resistor. The maximum amplitude of the pulses is limited by the maximum allowable forward voltage of the thyristor. Using the type BWT30-800R thyristor, the maximum amplitude obtained for the pulses was 500 volts with a choice of PRF up to 10 kHz for continuous operation. Higher amplitudes may be obtained by choosing thyristors of types BWT30-1000R and BWT30-1200R.

The thyristor operates when a pulse of 5V and 1A is applied to its gate terminal. In the initial state, when the thyristor is non-conducting, capacitor $C_1$ is charged up to positive supply voltage (at point A) and the voltage at point B or point C (the output) is zero. The energy stored in capacitor $C_1$ is about 1.3 m.joules.

Once the gate pulse has been applied, the thyristor turns on rapidly and thereby short-circuits one side of $C_1$ to the ground side of the circuit. This allows the resistors $R_2$ and $R_3$ and the transducer to make contact with the terminals of the charged capacitor. The instant at which the thyristor becomes conducting a transient negative voltage appears at points B and C, and immediately charges up the capacitance of the transducer and the cable. The large transient current through resistors $R_2$ and $R_3$ causes capacitor $C_1$ to lose its stored energy in a fraction of a microsecond and this produces a negative voltage signal at the output (as shown in Fig. 5.6b). The main part of the first edge of the signal (from 10% to the maximum amplitude) takes place within less than 80 nsec. The values of $C_1$, $C_0$ (the capacitance of the cable and transducer) and the equivalent resistance of the two parallel resistors $R_2$ and $R_3$ determine the decay time of the signal at the second edge.

The capacitance of the transducer and the cable has no considerable effect on the rise time of the transient voltage, since the conducting thyristor

and diode $D_1$ introduce a negligible resistance in the loop. It of course reduces the amplitude of the pulse to below the voltage to which the capacitor $C_1$ is initially charged. The rise time $t_r$ of the excitation pulse is completely determined by the thyristor, and starts after a short delay time $t_d$. The turn-on time of thyristors is usually defined as

$$t_{on} = t_d + t_r$$

The value $t_d$ for the BTW30 is approximately 0.2 μsec when a 1 amp trigger current is applied. In this circuit, capacitor $C_2$ is added across the thyristor in order to decrease time $t_r$. In operation, $C_2$ is charged up to the supply voltage at the same time as $C_1$. The voltage across this capacitor produces extra current for the thyristor and makes it conduct faster. The extra current causes no damage during its very short duration.

After the input trigger pulse has been removed, the thyristor remains conducting for a short time until the voltage of the discharging capacitor $C_1$ reaches a small value. At this time the current passing through the thyristor is approximately 100 mA, which is initiated from the supply voltage through $R_1$. This current is less than the holding current required for the thyristor and thus the thyristor reverts to the OFF state after a certain time called the turn-off time. This time for the thyristor BWT30 is a maximum of 12μsec, (Mullard handbook, 1972). As soon as the thyristor turns off, the capacitor $C_1$ recharges up to the supply voltage through $R_1$. The time taken for a full recharge of $C_1$ is less than 60n sec.

During the recharging of $C_1$, the transient current passing through $R_2$ generates a positive overshoot at point B of the circuit. The overshoot makes diode D become completely non-conducting and the transducer together

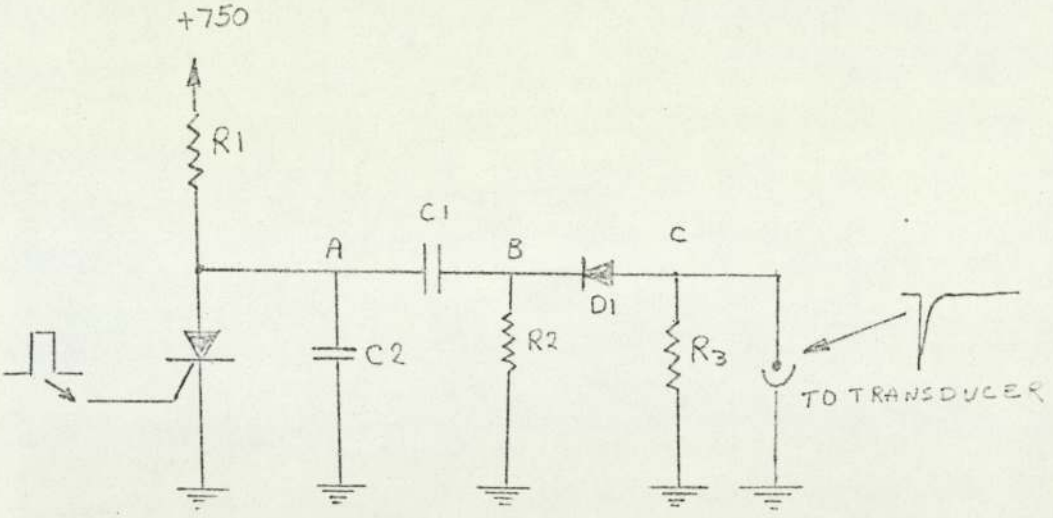


R1= 8K , R2 = 100 , R3 = 47 , C1 =4700pF ,
C2 = 2700pF

(a)

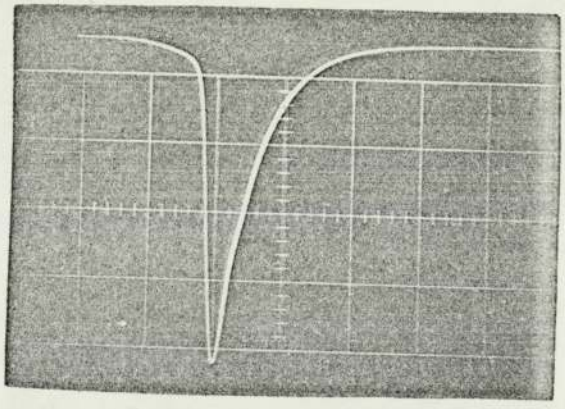

100 V/div , 0.4 μsec/div

(b)
without shunt
capacitor

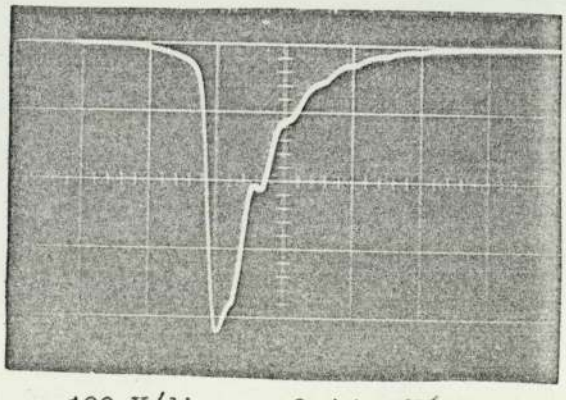

100 V/div , 0.4 μsec/div

(c)
with shunt capacitor

Fig. 5.6. Circuit diagram of the transducer driver.

with shunt $R_3$ becomes isolated from the rest of the circuit. At this stage, any echoes received back at the transducer are detected without being superimposed on any d.c. voltage.

In order to amplify the small echoes received across $R_d$ (=50Ω), the output can be connected to a suitable amplifier, which is protected by a limiter circuit (eg two parallel diodes) from high-voltage excitation-pulses. The Harwell band pass amplifier type 95/0187-$\frac{1}{6}$ was used for this purpose.

Finally, it must be noted that a variable shunt capacitor can be applied across $R_3$ in order to change the shape of the driver pulse (Fig. 5.6c).

### 5.5.3 The Converter

Details of the circuits designed for converting the detected change in transit time to a voltage analogue are shown in Fig. 5.7. The action of the circuits is controlled by the four short pulses: the gating pulse, reset pulse, clear pulse and sampling pulse. These are all generated after a certain delay from each drive pulse.

The threshold voltage comparator, which first receives the echo signals, uses an integrated circuit (type LM306). Its operation lasts for the duration of the gating pulse, which is supplied to the strobe of the LM306. The delay and the width of the gating pulse are adjustable, using the mono-stable flip-flop type 74121, over a range covering one cycle of the PRF.

The threshold level of the comparator can be adjusted by the 1 kΩ potentiometer to a few millivolts above the reverberation background level. The adjustment can be set for detection of either the positive amplitude or the negative amplitude of the first cycle at the start of the target echo signal. Having adjusted for positive amplitude, the output is superimposed on the gating pulse, waveform (4) in Fig.5.4.

The output of the comparator will cause the JK flip-flop $B_1$ to generate one single pulse (waveform (5) in Fig.5.4), which changes the state of the JK flip-flop $B_2$ and in turn stops the operation of $B_1$. $B_2$ will be returned to its normal state (logical 0) by means of the clear pulse.

The negative-going edge of the pulse generated by $B_1$ is locked to the positive amplitude of the first cycle of the echo signal. This pulse changes the state of the D-type edge-triggered flip-flop ($D_1$), which will be changed again by the negative going edge of the gating pulse. The output pulse (waveform (6) in Fig.5.4) has a width which changes in step with the echo-delay.

The integrator is a high-speed operational amplifier (type μA715) with a feedback capacitor C. The capacitor is paralleled with a fast-switching transistor $T_1$, which allows the rapid discharge of the capacitor at a specified time. $T_1$ is driven by the reset pulse from the cut-off region into the saturation region for 1μsec. For each pulse generated by the D-type flip-flop, $C_1$ is charged with a constant current determined by Ein, the amplitude of the input pulse (logical 1, approximately 3.5 volt), and the input resistor R. Integration stops immediately after the input pulse has returned to the low level (logical 0; approx. 0.22 volt). The input diode is to isolate the integrator from this low level.

The integrator output is sampled by the FET $T_2$ and stored on $C_2$. $T_2$ conducts during the sampling pulse. To avoid any loading effects, the voltage stored across $C_2$ is available for recording through a unity gain buffer amplifier.

The calibration graph in Fig. 5.8 shows the linearity and the high sensitivity of the system.

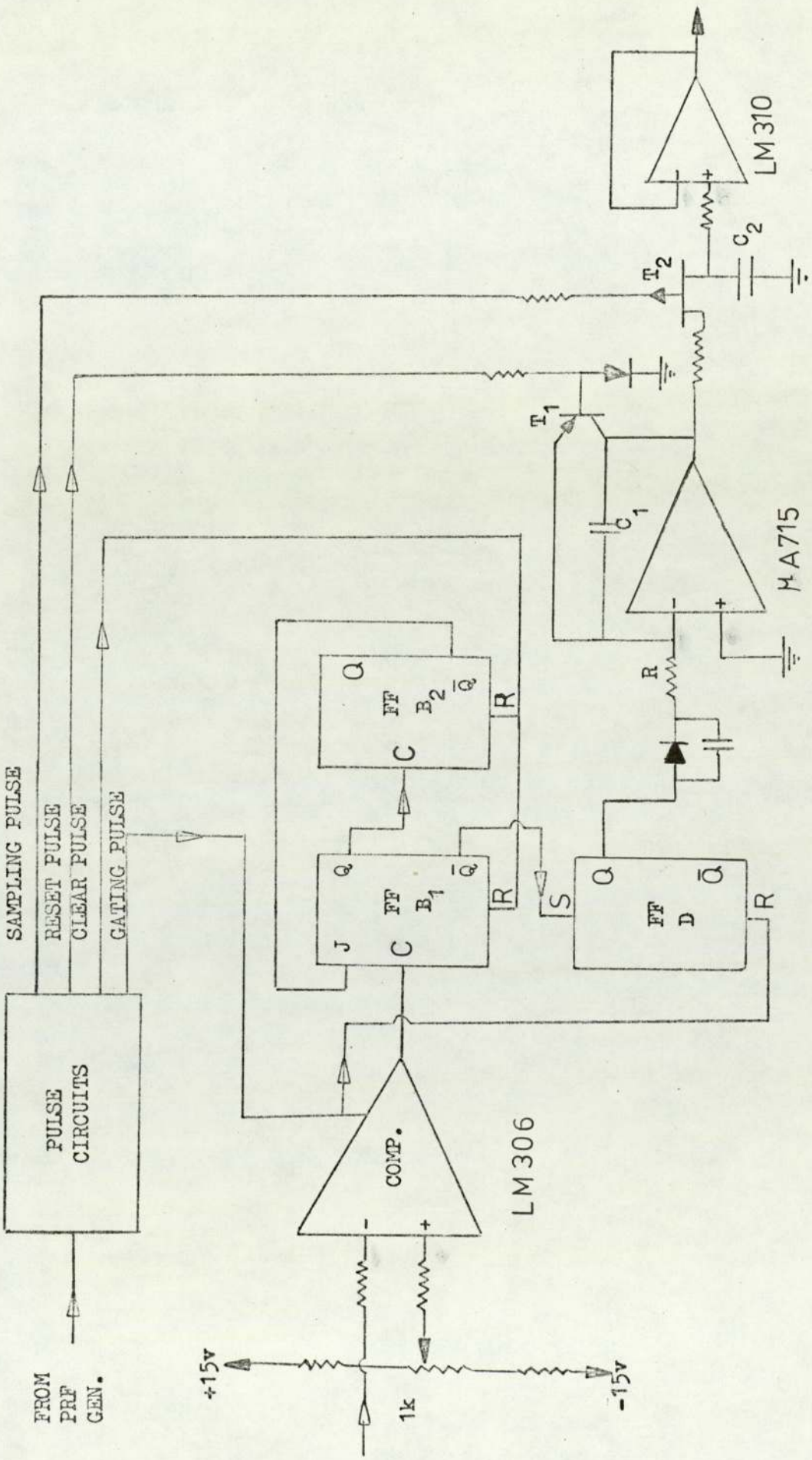


Fig. 5.7. Circuit diagram of the converter.

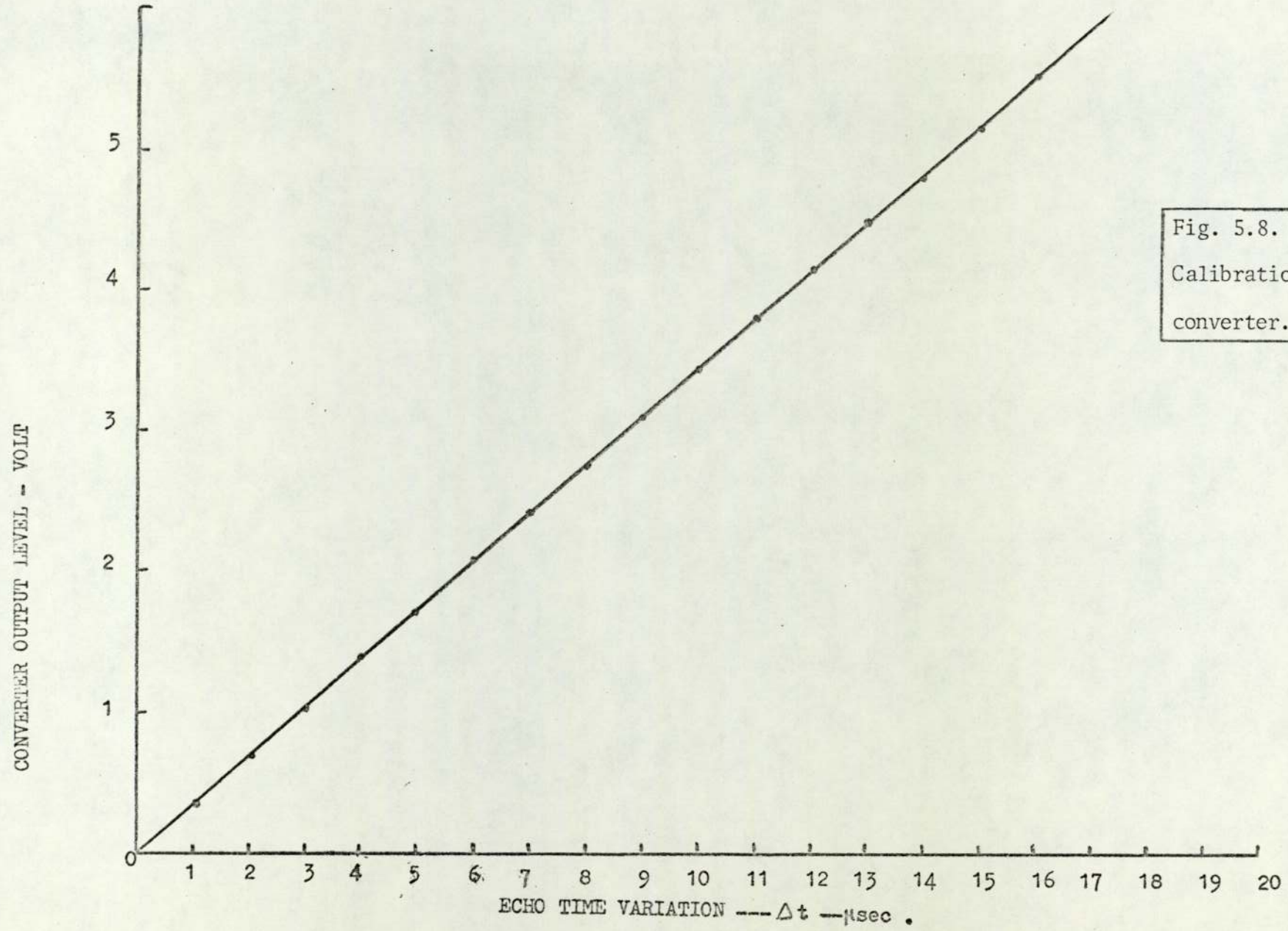


Fig. 5.8.
Calibration of the converter.

As an illustration of the sensitivity, an experiment was conducted in which the change in transit time of an echo from a target in a water column was measured (apparatus as in Figs. 7.1 and 7.2). When the column was heated in order to induce circulating convection currents, the presence of the currents was shown to a remarkable degree by the fluctuations in transit time, as in Fig. 5.9. It can be seen that the system was sensitive to changes in the region of 0.5nsec, and excursions as large as 40nsec were observed. Simultaneously a recording of temperature fluctuations was taken with a thermocouple, and verified the turbulent nature of the water. It is realised that the observed variation in the transit time is due to sound velocity fluctuations within the beam and to refraction of the beam caused by moving the thermal boundaries. It is clear that the system was functioning properly, for on removal of the source of heat the water column rapidly became stable, as is shown by the later part of the same recording. It is worth noting that if similar temperature fluctuations occur in the cooling tube, the slow transit time variations have no serious effect on the rapid bubble size measurement, provided that the echo amplitude does not drop below the threshold level.

The fluctuations in transit time observed in Fig. 5.9 were partly due to fluctuations in the echo amplitude. When the amplitude varies above the threshold level of the comparator, the phase of the detected point changes too. Thus, the system can also be applied for detection of small changes in echo amplitude, such as attenuation of a target echo due to movement of suspended gas bubbles or particles. The time record in Fig. 5.10a was obtained when the temperature in the water column was stable and uniform; each detected pulse indicated on the record was produced by the movement of a narrow wire (0.5mm diameter) across the beam. The width of the pulse indicates the time taken for the wire to

cross the beam. Fig. 5.10b shows a similar record when molten tin at 350°C was used.

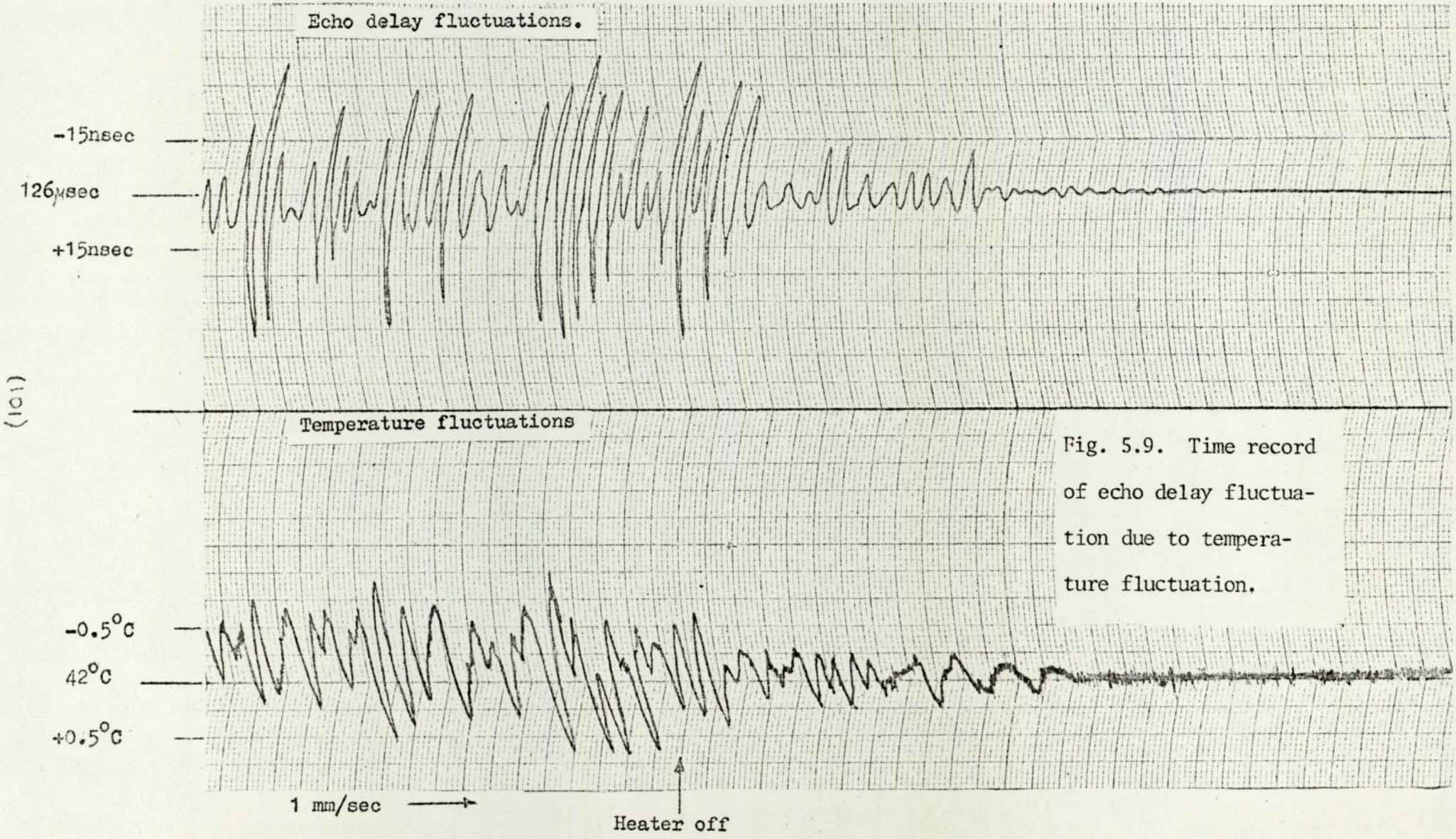


Fig. 5.9. Time record of echo delay fluctuation due to temperature fluctuation.

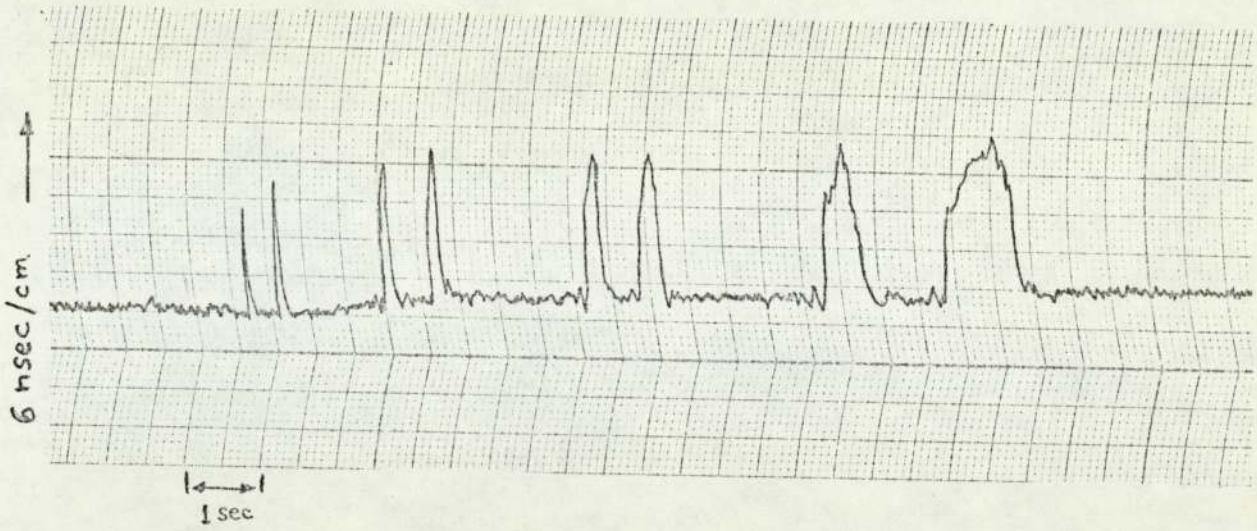


(a) Movement of 0.5mm wire across the beam in water, back target distance 20cm.

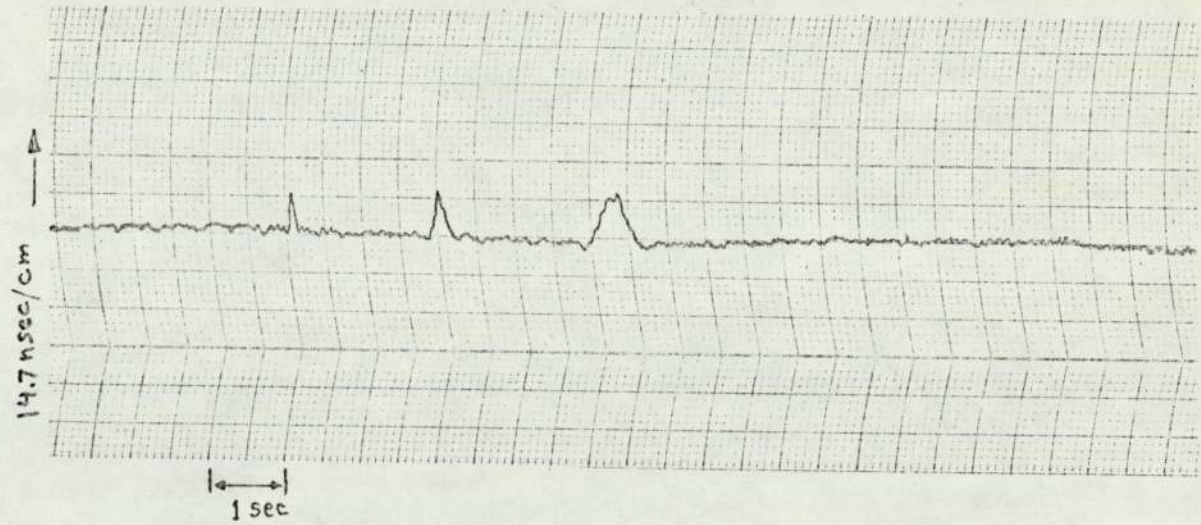


(b) Movement of 0.5mm wire across beam in molten tin at 350°C, target distance 20cm.

Fig. 5.10. Detection of moving small particles in liquids by back target echo method.

# CHAPTER 6

# ANALOGUE EXPERIMENT FOR BUBBLE GROWTH MEASUREMENT

## 6.1 DESCRIPTION

In order to determine the ability of the ultrasonic system to detect and measure small and/or fast liquid - vapour interface movements, a relatively simple experiment was carried out using water as an analogue of liquid sodium. Water and sodium are similar acoustically; for comparison the sound velocity, acoustic impedance and bulk attenuation in pure water[51] and pure sodium[27] are given in Table 6.1.

TABLE 6.1

| Liquid | | Velocity (c) $m.sec^{-1}$ | Acoustic Impedance ($\rho c$) $(kg.m^{-2}.sec^{-1})\times10^{-6}$ | Attenuation $(\alpha/f^2)\times10^{17}$ $cm^{-1}.sec^2$ |
|---|---|---|---|---|
| Pure water, | 20°C | 1497 | 1.49 | 21 |
| Pure Sodium | 250°C | 2440 | 2.16 | 15 |
| | 900°C | 2100 | 1.57 | ? |

In a container air bubbles were blown from the end of a narrow target pipe in water; the bubbles formed in this way behaved rather differently from a vapour bubble but did present a moving curved interface similar to that of a growing vapour bubble. A high-speed ciné camera was used to photograph the air-bubble growth, and continuously to superimpose the ultrasonic monitor output trace from the CRO (cathode ray oscilloscope) face onto the ciné film (see Fig. 6.1). With this method the film moved in a direction parallel to the CRO time-axis and the CRO time-base was turned off. The output voltage of the electronic system in response to a fast-growing bubble consists of a series of steps, as was described in Chapter 5, and thus appears on the ciné film as a series

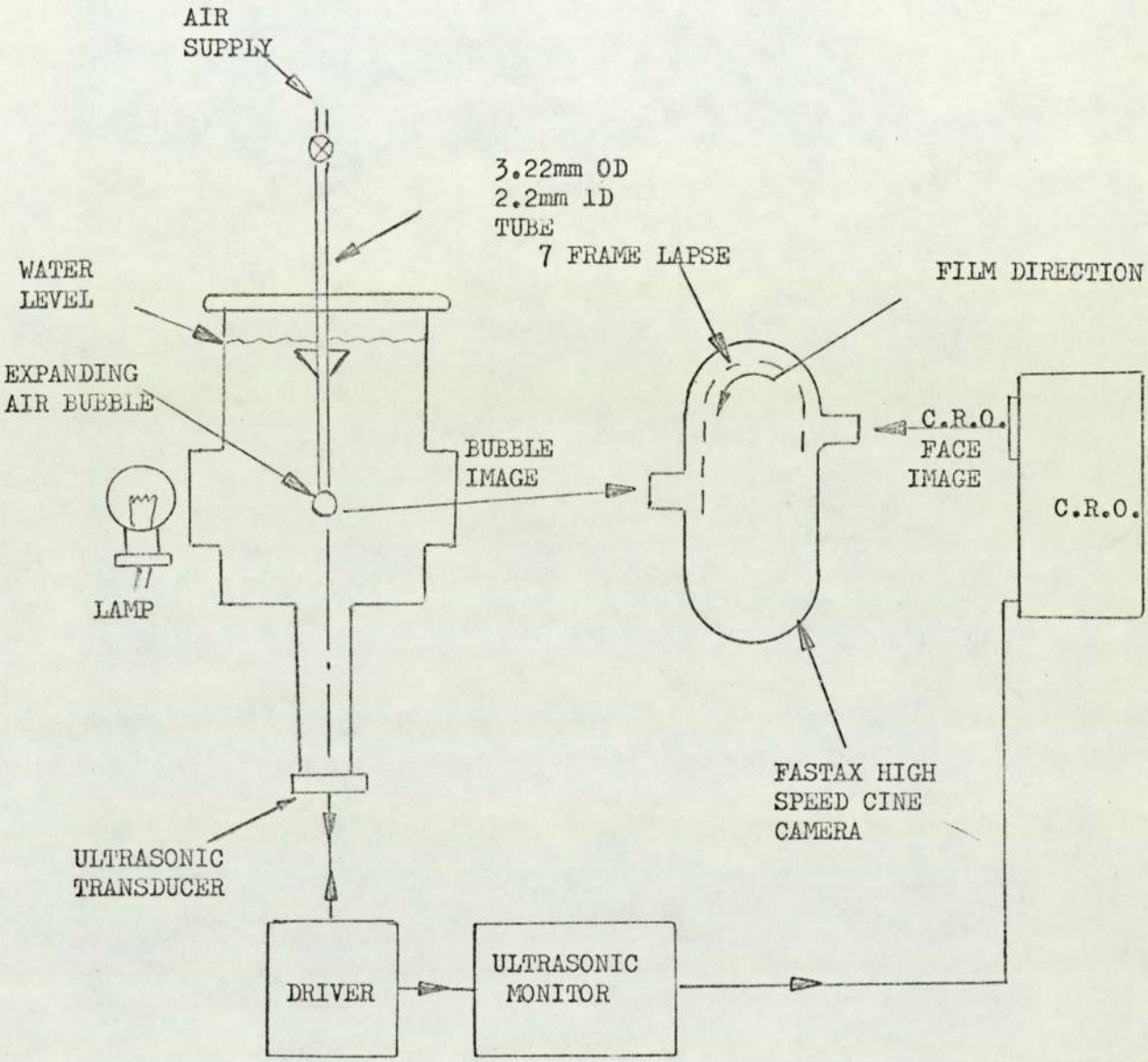


Fig. 6.1, Arrangement for simultaneous optical and ultrasonic detection of the interface position of an expanding air bubble in water.

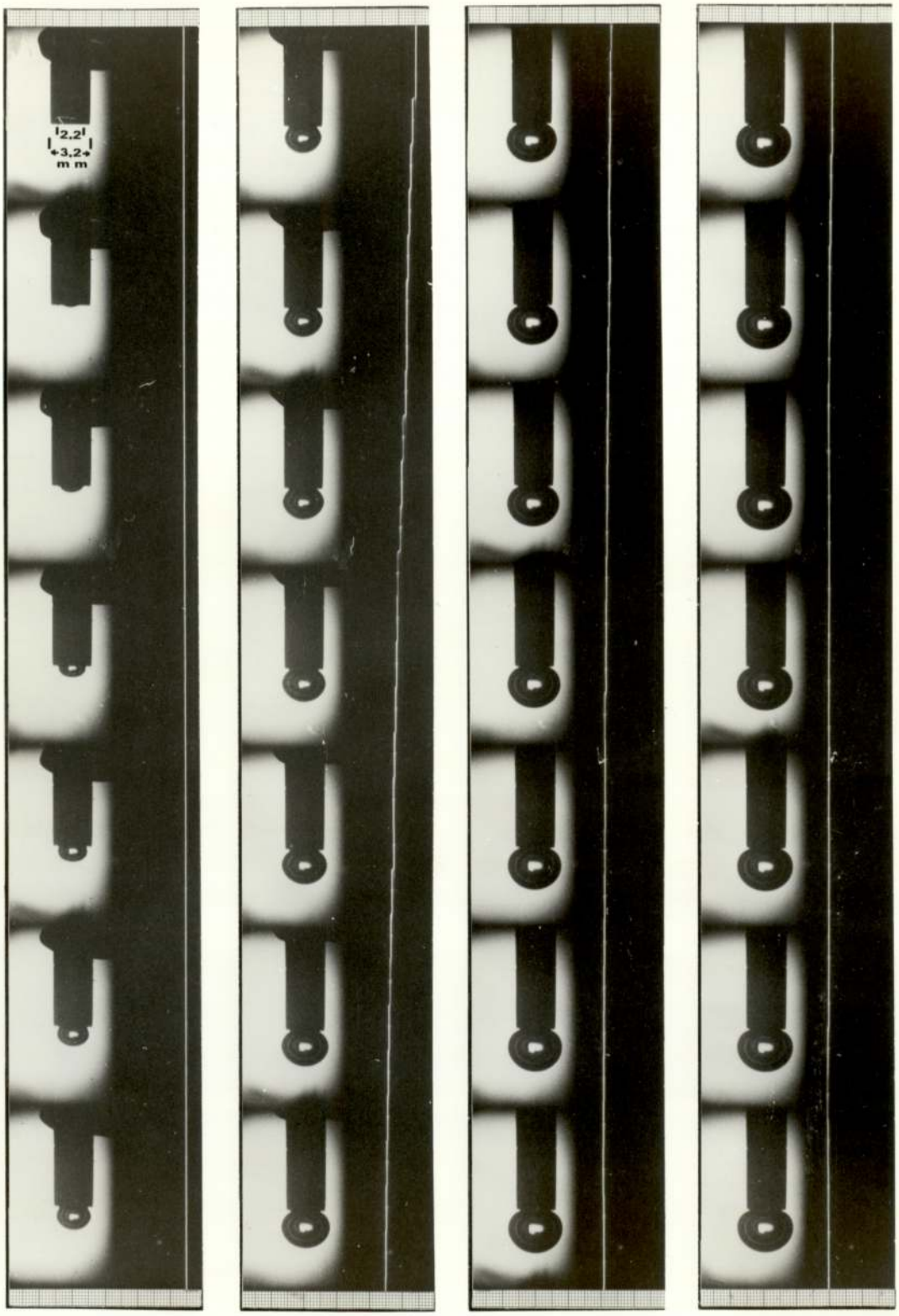


FIG. 6.2 CONSECUTIVE FRAMES FROM CINE FILM OF AIR BUBBLE GROWTH AND OSCILLOSCOPE TRACE OF ULTRASONIC MONITOR OUTPUT.

NOTE: 7 FRAMES DELAY BETWEEN TRACE AND BUBBLE.

FILM SPEED = 1250 F/S. PRF = 5.3 KHZ.

of short lines along the film. Each line has a length which depends on the film speed and the PRF. The position of each short line on the film changes as the bubble interface moves and therefore the ultrasonic monitor output can be compared with the actual bubble size. A series of prints taken from part of a high-speed ciné film is shown in Fig. 6.2. Details of the early tests have been reported in AERE-R7840 (Kazemeini/Ralph 1975).

Measurements from the ciné film were taken from two separate reference points on the enlarged picture of each frame. One side of the air pipe was chosen as the reference point for the trace, and the base of the pipe as the reference point for the extreme bubble interface position. It was concluded in Chapter 3 that in the geometrical region the bubble echo received at the transducer is from the point on the bubble surface nearest to the transducer (the effective reflecting area). The bubble size seen on each frame corresponds with the trace seven frames behind, due to the relative position of the two camera lenses. Using the calibration graph of the electronic system, the conversion factor of the ultrasonic measurement in water is 0.45 volts per 1mm bubble interface movement. The results showed excellent agreement between the actual bubble interface movement and the ultrasonic measurement for PRF rates up to 10 kHz.

## 6.2 EXPERIMENTAL CONDITIONS

The experiment was carried out in a brass container identical to the sodium pool. The following conditions were therefore met, although they limited the system operation:

(i) detection of the bubble at a large distance in the far field of the transducer.

(ii) use of a metal diaphragm to protect the transducer.

(iii) the necessity for transmission and reception of the echo

through a narrow tube of 2cm diameter and 15cm length (for cooling purposes in the actual pool).

Spurious echo signals, due to reverberation in the pool and to the reflection off the inner surface of the cooling tube of waves entering it, are to be expected in the analogue pool and will cause further problems in operating the system.

Large distances between the transducer and the bubble reduce the resolution of the pulse-echo system. The best distance is at the end of the near field (8cm in water, 6cm in sodium), since the sensitivity of the incident beam is maximum at this distance. The actual target distance was 27cm.

It was shown in Chapter 4 that if the diaphragm has a thickness of approximately $\lambda/2$, $\lambda$, or $3\lambda/2$, the transducer, after being excited with a transient voltage, generates a long duration signal for each echo received. The maximum amplitude of the echo signal appears after almost eight cycles for a diaphragm of $\lambda/2$ thickness and fourteen cycles for a diaphragm of $\lambda$, etc. The echo amplitude decays to zero at a slower rate. With these diaphragm thicknesses the energy contained in each echo pulse is great; the shape of the signal, however, is unsatisfactory for the system. This is because the energy of the unwanted echo signals together with their interference with each other greatly increases the level of background reverberation.

In some measurements discrepancies between the actual bubble-interface movements and the ultrasonic measurement were observed. They were attributed, in the main, to the effect of the diaphragm.

## 6.3 EFFECT OF ECHO SHAPE

A steel diaphragm of 0.57mm thickness (near to $\lambda/2 = 0.55$) was chosen for the study of its effects on the measurement. Since the background

reverberation increases with PRF, the PRF was adjusted to 2.4kHz at which the maximum amplitude of the echo from a spherical bubble of for example 1.5mm diameter could just be detected against the background noise level. This maximum amplitude was estimated by using the pipe echo amplitude as a reference. The target pipe represented a flat area of 4.2mm$^2$. According to Chapter 3 the estimated echo amplitude from a spherical target of 1.5mm diameter is about 1/26 of that from a flat circular target of 4.2mm$^2$ area. Graphs of the bubble interface position and the simultaneous detector output, taken from the ciné film, are shown as a function of time in Fig. 6.3. The relationship between the two measured values is also shown in Fig. 6.4. It can be seen that the agreement between the observed bubble interface position and the ultrasonic measurement was not achieved during bubble growth until the interface had moved some 3mm. The reason for the disagreement is associated essentially with the shape of the echo signal. Figs. 6.3 and 6.9 also show further disagreement during the bubble detachment phase. This is attributed to the bubble movement out of the centre part of the ultrasonic beam and thus to the drop of the back-scattered energy to below detection level.

During the early stages of bubble growth, the amplitudes of the first few cycles of the bubble echo, ie 1st to 7th, were smaller than the background reverberation level. Since the threshold level of the electronic system is adjusted to above this noise level, only the 8th cycle of the echo was detected (as pulse (S) in Fig. 6.5), and that after some delay from growth commencement. Fig. 6.5 shows that the initial echo movement during the time taken from the tube echo $T_{P1}$ to $T_{BS}$ cannot be detected. As the bubble size increased, the amplitude of the echo increased too and at a certain size, at time $T_{BM}$, the first cycle was detected above the reverberation level. As a result of this,

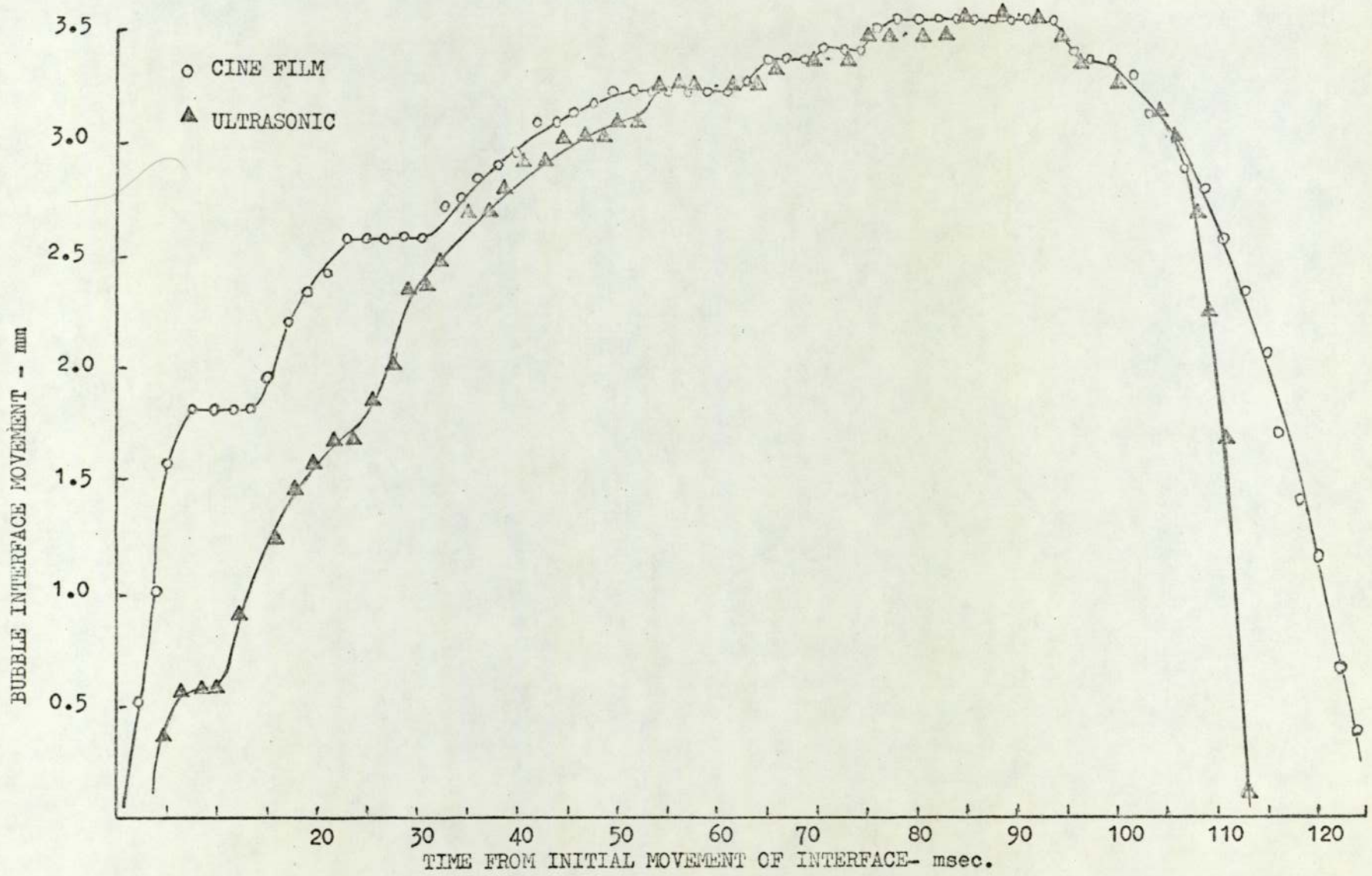


Fig. 6.3. Comparison between actual bubble growth and ultrasonic monitor output with time.

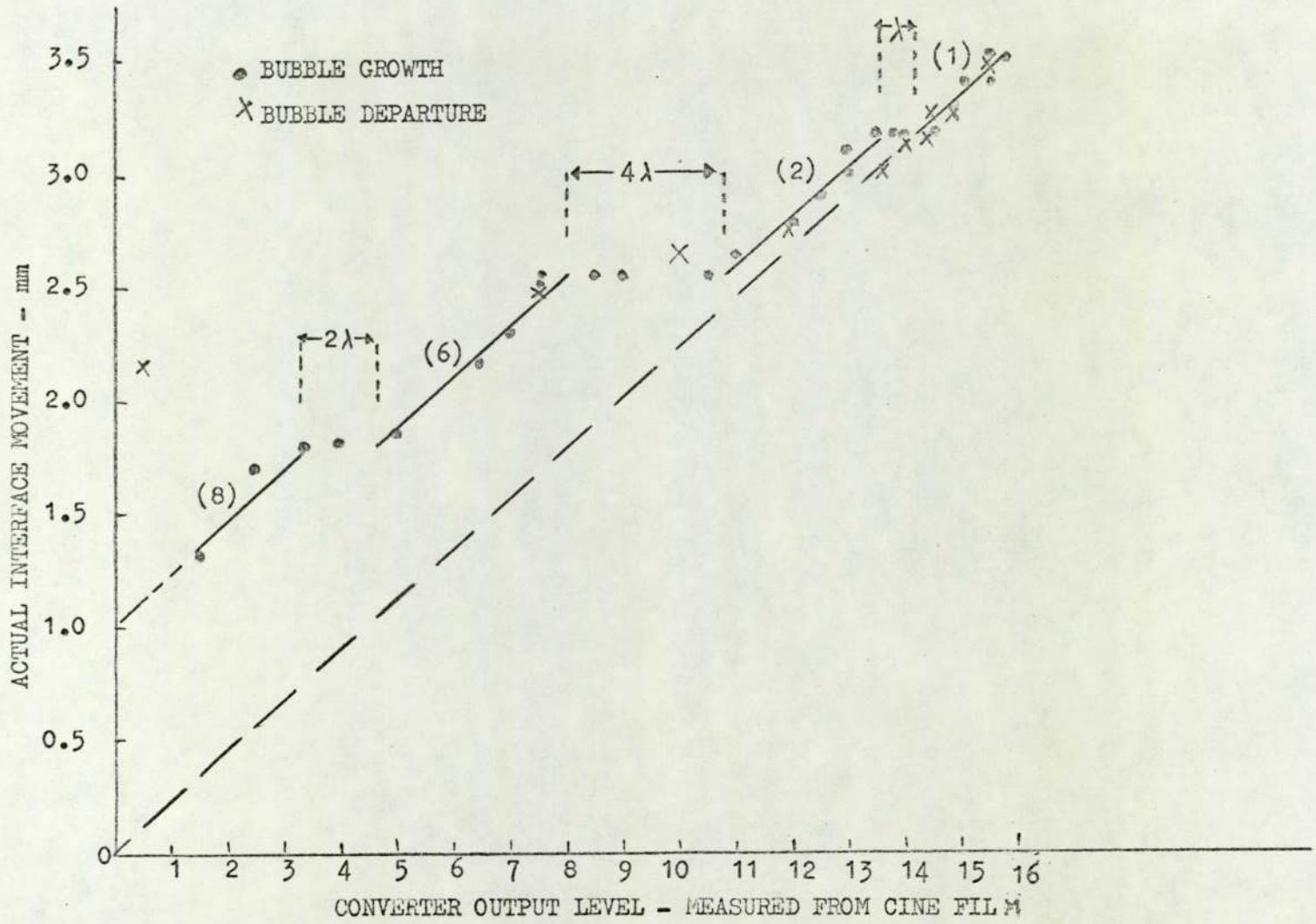


Fig. 6.4. Comparison between actual bubble growth and ultrasonic monitor output.

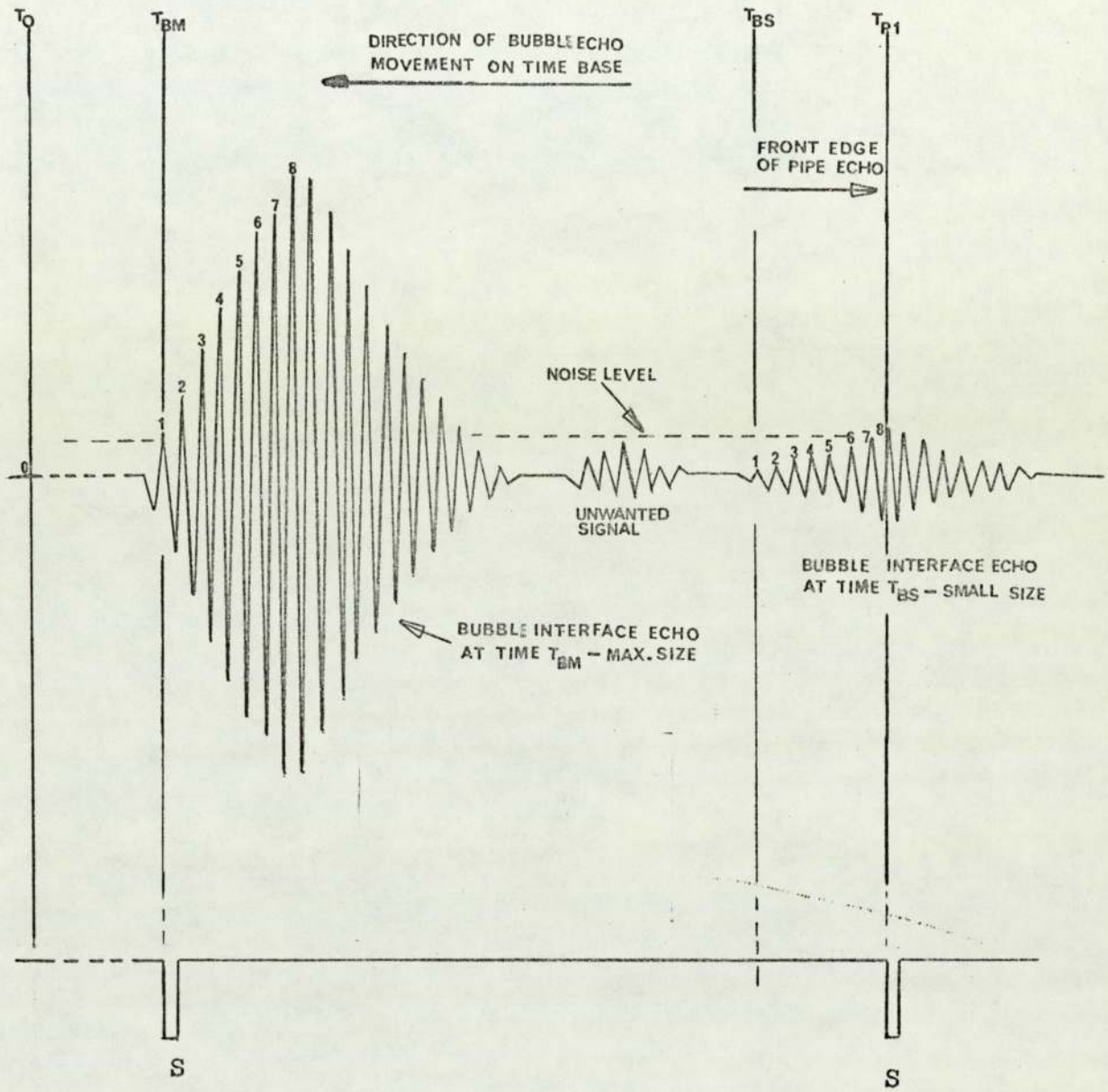


Fig. 6.5. Movement of pulse S during bubble growth.

pulse(s) jumped, cycle by cycle, from the 8th to the 1st as the bubble grew. Due to this effect, the experimental graph in Fig. 6.4 is divided into several, almost straight, short lines; each line is labelled with a number corresponding to the number of the cycle in Fig. 6.5. Fig. 6.4 shows that during bubble growth the monitor output level has jumped from the position of cycle (8) to that of cycle (6), from (6) to (2) and from (2) to (1). The broken line represents the ideal relationship between the bubble interface position and the ultrasonic measurement.

The above effect also occurred in the opposite direction when the echo amplitude decreased during bubble departure. Surface tension and buoyancy forces caused the bubble to move out of the sensitive part of the beam and so reduced the echo amplitude. Since the echo is reflected from the extreme bubble interface (the nearest point to the transducer), the echo amplitude decreases as the nearest point moves away from the beam axis. This has been analysed in Chapter 3.

It can be seen from the above that the resolution and the accuracy of the system were generally unsatisfactory at a PRF of 2.4 kHz. At lower PRFs (eg 1.5 kHz) the signal-to-noise ratio of the system was improved so that small bubble echo signals could be detected. But this range of PRF is inadequate for the measurement of the rapid growth and collapse of the sodium vapour bubble. The need to detect the bubble interface movements at higher PRFs meant that an improvement of the echo shape was required.

## 6.4 IMPROVED SYSTEM

In order to improve the performance of the detection system, the echo signal duration had to be reduced. As was mentioned above, the presence of a metal diaphragm of thickness $\lambda/2$ extended the echo signal with a typical shape causing the signal-to-noise ratio of the system to

deteriorate. Consequently, it was not possible to detect the earlier stages of bubble growth when the interface movement was less than 1.3mm.

One solution to the problem is to choose a diaphragm thickness of an odd multiple of $\lambda/4$. Thus, if the transducer oscillates at a single frequency the duration of the echo signal becomes a minimum. However, this is not really satisfactory in the case where the transducer is driven by a shock pulse.

A second solution to the problem is to change the shape of the drive pulse, as was described in Chapter 4. With this method the leading edge of the drive pulse excites the transducer, and the trailing edge, with some delay, excites the transducer again out of phase with the reflected waves inside the diaphragm. This, to some extent, cancels the effect of the multiple reflections in the diaphragm and significantly reduces the signal duration. The required pulse-drive was generated by the transducer driver (Chapter 5) with the aid of a simple shaping circuit. Fig. 4.10 in Chapter 4 shows that the echo signal duration can be reduced from 16μ.sec to approximately 1μ.sec without any changes in the amplitude of the first or the second cycle of the signal. By applying this method the signal-to-noise ratio of the system was greatly improved, even up to 10 kHz.

Fig. 6.6 shows the echoes reflected from the target tube and the bubble in its early stages of growth. The amplitude of the spurious echoes (reverberation level) and the interference from these echoes increase with repetition rate (compare Fig. 6.6a with Fig. 6.6b). Comparison of Figs. 6.6b and c shows the improvement in the bubble echo shape and the reduction in the noise level when the transducer is excited by a suitably-shaped drive-pulse.

The correlation between the bubble interface movement and the monitor

output of the improved system was tested in the analogue experiment. The graph in Fig. 6.7 shows excellent agreement between the bubble interface position and the simultaneous detector output at the growth stage. The discrepancy at the bubble departure stage is again due to the movement of the bubble out of the ultrasonic beam, resulting in the detector output voltage falling to zero.

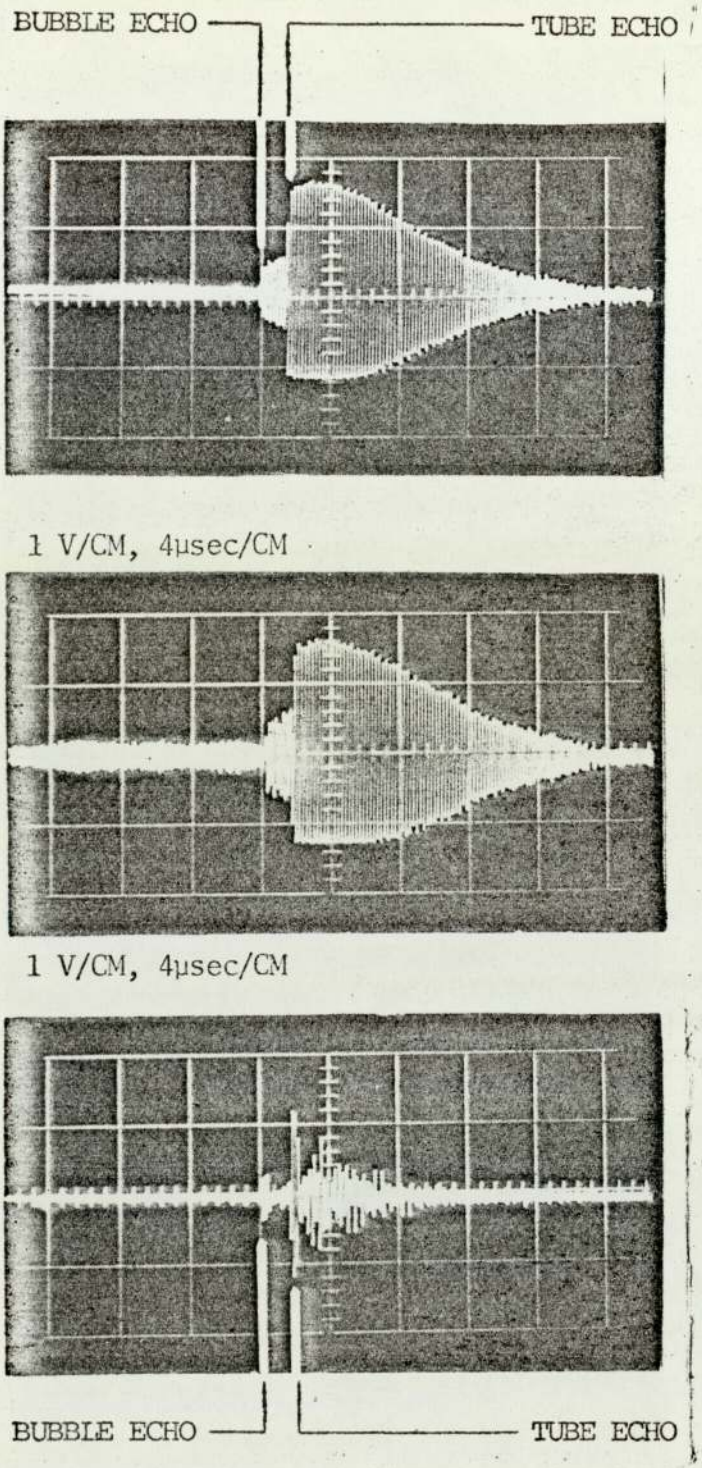


(a) Using transient pulse excitation at 1.8 kHz PRF.

(b) Using transient pulse excitation at 4.8 kHz PRF.

(c) Using modified pulse excitation at 4.8 kHz PRF.

Fig. 6.6. Echoes from tip of target tube and air bubble with a diameter of 1.2mm in water.

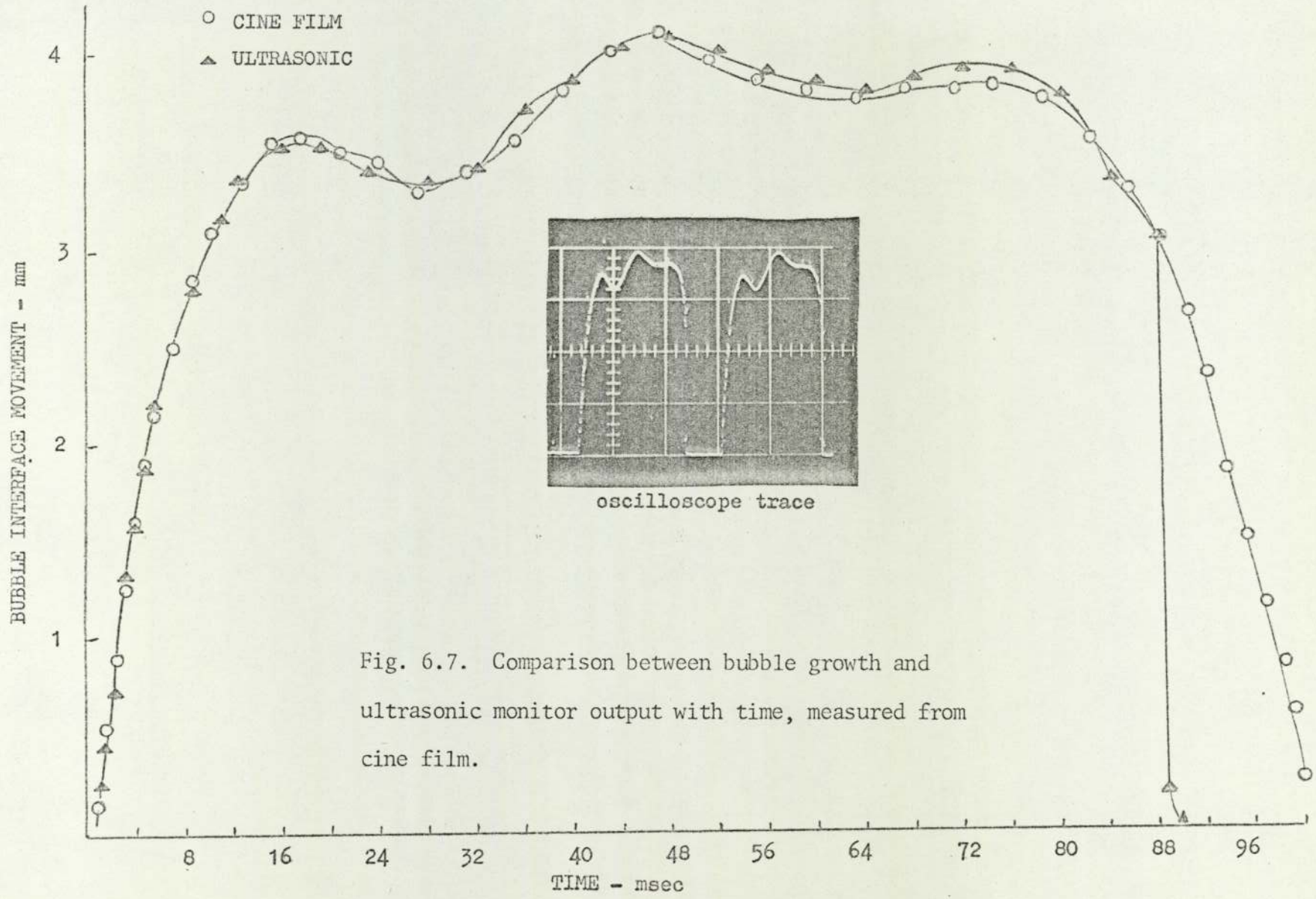


Fig. 6.7. Comparison between bubble growth and ultrasonic monitor output with time, measured from cine film.

# CHAPTER 7

# PULSE ECHO MEASUREMENT IN TEMPERATURE GRADIENTS IN LIQUID METALS

## 7.1 INTRODUCTION

In the sodium pool the piezoelectric transducer (PZT5A) is protected from the high temperature (900°C) by a liquid-filled cooling tube. A sharp temperature gradient exists along the ultrasonic path, since the end of the tube is cooled to 250°C.

In order to test for any problems of ultrasonic signal attenuation associated with this type of temperature buffer, experiments were carried out in Woods metal (MP 70°C) up to 400°C and tin (MP 232°C) up to 900°C. Liquid sodium was not used for this investigation since it can only be handled using the most stringent safety precautions and the cost of building and maintaining a sodium apparatus would be considerable. Justification for choosing Woods metal and tin is simply that their melting points, like that of sodium (MP 98°C), are both lower than the maximum operating temperature of the transducer (280°C).

The tests were carried out in a vertical cylinder with the protective diaphragm and the transducer mounted at the base in an air-cooled section. With Woods metal, the temperature of the transducer was kept at 90°C while the liquid in the hot zone had a maximum temperature of 400°C. For the tin experiment, the transducer temperature was held near to or below 280°C while the temperature of the liquid in the hot zone was increased up to 900°C. Large temperature gradients were thus obtained and echo signals from the hot zone were studied.

Useful information was obtained for the application of this technique in the sodium pool. The technique was also used for measuring sound

velocity in Woods metal and tin at high temperatures.

## 7.2 ECHO SIGNAL ATTENUATION

Some energy is lost in transmission due to the impedance mismatch at the liquid-diaphragm boundary. The acoustic impedance of steel (the diaphragm) is $47 \times 10^6$ kg.m$^{-2}$.sec$^{-1}$ and the acoustic impedance of Woods metal, tin and sodium at 250°C are given for comparison in Table 7.1. Stronger echo signals are expected in liquid metals than in water, since the acoustic impedance of water is less ($1.5 \times 10^6$ kg.m$^{-2}$.sec$^{-1}$ at 20°C) than that of liquid metals. However, if the liquid metal does not wet the diaphragm completely the impedance mismatch becomes much greater and most of the energy can be lost in this way.

TABLE 7.1: Acoustic Impedance at 250°C

| Liquid | Density ($\rho$) kg.m$^{-3}$ x $10^{-3}$ | Velocity (c) m.sec$^{-1}$ | Acoustic impedance ($\rho c$) kg.m$^{-2}$.sec$^{-1}$ x $10^{-6}$ | Reference |
|---|---|---|---|---|
| Sodium | 0.88 | 2440 | 2.16 | (28) |
| Woods metal | 9.26* | 1992 | 17.71 | *(59) |
| Tin | 6.93* | 2455 | 16.98 | *(58) |

Reduction of the echo strength in the liquid itself is due to bulk attenuation, beam-spreading at large distances and refraction by the thermal boundaries. Bulk attenuation is brought about by two phenomena: scattering and absorption. Scattering results from the inhomogeneities and suspended particles, and it increases as the third power of particle cross-section area (see Chapter 3). The Rayleigh region in Fig. 3.4 shows that scattering for particle sizes smaller than $\frac{1}{100}$th of the wavelength becomes negligible.

Absorption is attributed to shear viscosity, thermal conductivity (the

classical absorption) and possibly structural relaxation,[26,27] and it usually increases with the square of frequency. The classical absorption increases with temperature. Kim et al[27] showed that even slight impurities or contamination (eg by contact with air) can change the absorption coefficient noticeably. In pure liquid metals the absorption of sound is very small.

The attenuated intensity of a plane wave due to bulk attenuation is given by:

$$I = I_o \, e^{-2\alpha r}$$

where $I_o$ and I are the intensity at the beginning and the end, respectively, of a section with length r. Since the wave generated by the disc transducer diverges in the far field, according to equation (3.3), further decrease in intensity with distance occurs. Thus

$$I \propto \left(\frac{2J_1 (k\mathrm{Sin}\theta)}{k\mathrm{Sin}\theta}\right) \frac{1}{r^2} . e^{-2\alpha r}$$

and the energy of an echo reflected from a target depends in part on the average incident intensity which in turn depends on the size and position of the target. This is fully described in Chapter 3.

The above expression shows that if the position of the target changes within the beam (ie $\theta$ changes) the echo strength will change too. This would also happen in the case of a fixed target in a liquid with temperature fluctuations; the beam is refracted due to random motions of the thermal boundaries, and causes the average incident intensity on the target to fluctuate. Echo amplitude fluctuation is expected to occur together with echo delay fluctuation. To establish a controlled and stable thermal gradient through the temperature buffer, the cylinder has to be mounted with its long axis vertical, heated at the top and cooled at the bottom.

## 7.3 EXPERIMENTAL APPARATUS

The apparatus, as illustrated in Figs. 7.1 and 7.2, consisted of a vertical cylindrical vessel fitted with the ultrasonic transducer at the base and a target at the top, both on the axis of the vessel.

A large temperature difference in the liquid metal was obtained by using a heater wound round the top portion of the vessel and a cooler at the base.

Changes in the amplitude and the transit time of the target echo, together with changes in temperature were recorded by the system shown in Fig.7.2.

The vessel was made of a stainless steel cylinder, 25cm long and of 4.5cm diameter, which opened from the lower end into a smaller cylinder 5cm long and 2cm in diameter.

The top of the vessel was closed by a lid with small access holes for insertion of two thermocouple probes and the target rod, and for running a current of argon gas into the vessel. The argon gas current was to prevent oxidation at the surface of the liquid metal.

The target was the bottom face of a long stainless steel rod (40cm) of 6mm diameter, which was machined to 2mm diameter for a length of 5mm from the rod end, so that two parallel circular steps at the end of the rod were formed.

The transducer was a 5MHz/PZT ceramic disc of 10mm diameter, energised by a transient voltage pulse. The arrangement of the transducer probe was similar to that designed for the sodium pool. The transducer was isolated from the liquid by a steel diaphragm which was mounted at the cylinder base with an asbestos gasket with a maximum operating temperature of 480°C.

The heat sources in the system consisted of two electrical heaters, which were mineral insulated, stainless steel sheathed cables (Pyrotenax), with a maximum operating temperature of about 1000°C, power being supplied from two variacs connected to the 50Hz mains supply.

The temperature of the cylinder at the bottom was limited by the maximum operating temperature of the coupling paste (280°C) between the transducer and the diaphragm. In order to maintain the transducer at such a low and constant temperature while the temperature at the top was high and variable, an air cooler with a variable flow rate was mounted around the base of the cylinder, as shown in Fig. 7.1.

To avoid solidification of the liquid metal on the diaphragm face, another electrical heater was wound around the lower part of the vessel. This extra heater was used especially at the beginning of each experiment when melting the metal on the face of the diaphragm.

The body of the vessel was thermally insulated with stainless steel foil and ceramic fibre.

The measurement of the bulk-liquid temperature at different points was carried out with two shielded probe thermocouples which could be moved axially and radially in the vessel. The temperature of the transducer was measured by a thermocouple attached to the base of the vessel. Two more fixed thermocouples were used for measuring the temperature of the heaters. All thermocouples were chromel-alumel stainless steel sheathed, of 0.5mm diameter.

The output of the movable thermocouple, immersed in the liquid metal, was fed to the chart recorder, as shown in Fig. 7.2, so that a time record was available for each experiment. The outputs of all thermocouples were read separately, using a selective switch box and a digital voltmeter.

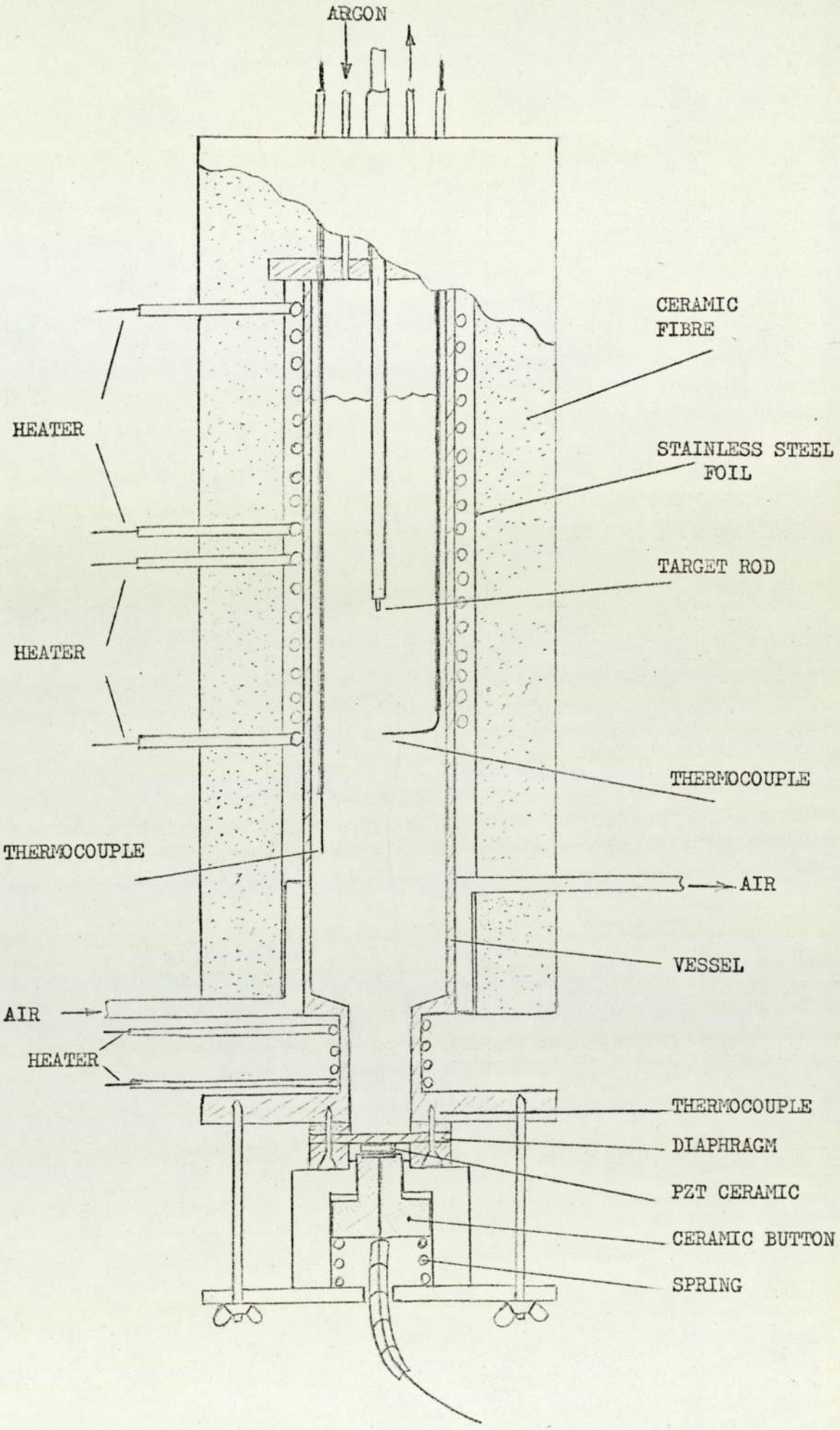


Fig. 7.1. Apparatus.

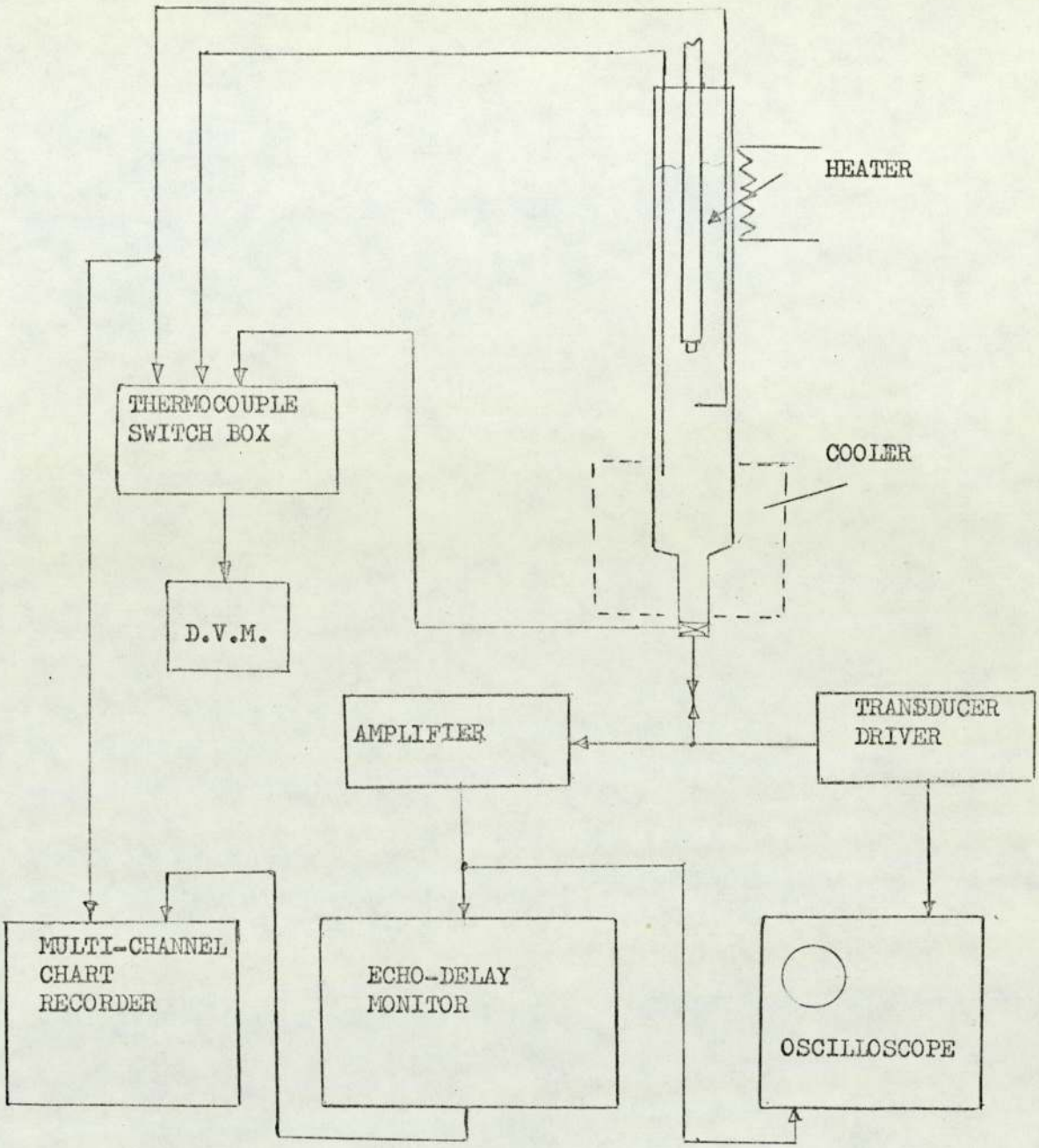


Fig. 7.2. Block diagram of measuring system.

## 7.4 SOUND VELOCITY MEASUREMENT

The apparatus was used to measure the velocity of sound and its temperature coefficient in Woods metal and tin at high temperatures. The technique was to measure the difference between the transit times of the echoes from the two steps of the target located in the isothermal region of the vessel. For this measurement the temperature of the transducer at the cylinder base was kept low and constant and the liquid temperature above 15cm from the transducer was increased to the required temperature. The target was placed at 20cm distance where the temperature and thus the sound velocity were uniform. The sound velocity at a fixed temperature, therefore, was obtained from the simple linear relationship between the transit time difference $\Delta t$ and d the distance between the two steps of the target (ie d = 5mm):

$$C = 2d/\Delta t$$

Fig. 7.3 shows the echo signals received from the two steps in Woods metal. The echo amplitude from the second step is about 5 times greater than that from the first step, due to their different areas ($3mm^2/25mm^2$). The difference between the amplitudes enabled the electronic system to measure $\Delta t$ easily. The echo signals were detected by two separate threshold voltage comparators which were adjusted for two different threshold levels. The electronic circuit was similar to that described in Chapter 5. $\Delta t$ was converted to a dc voltage and its variations with temperature were recorded on the chart recorder of the system shown in Fig. 7.2.

The results for Woods metal at temperatures between 90°C and 400°C and for tin between 300°C and 900°C are represented by the graphs in Figs. 7.4 and 7.5. It seems that the sound velocity in both liquids decreases almost linearly with temperature at least within the measured range. The

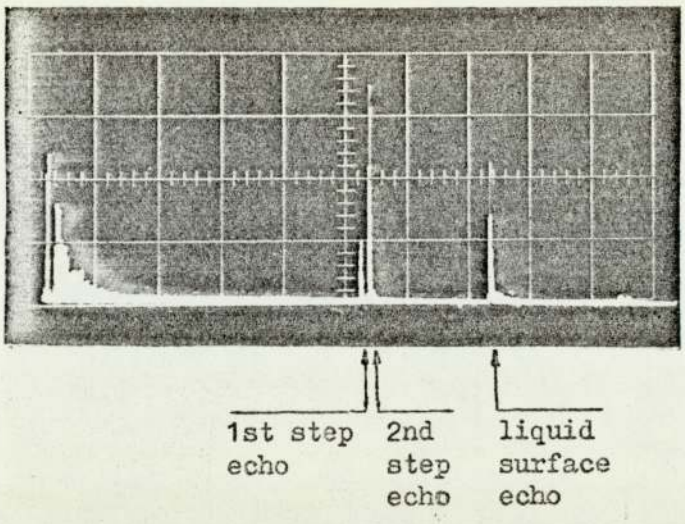


(a) 0.5 V/CM, 40μsec/CM

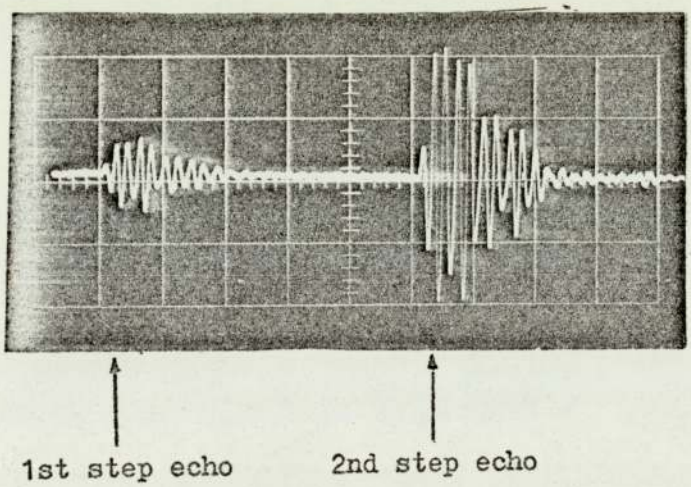


(b) Expanded echo signals 1V/CM, 1μsec/CM

Fig. 7.3. Echo signals from the two-step target and liquid surface in Woods metal at 320°C.

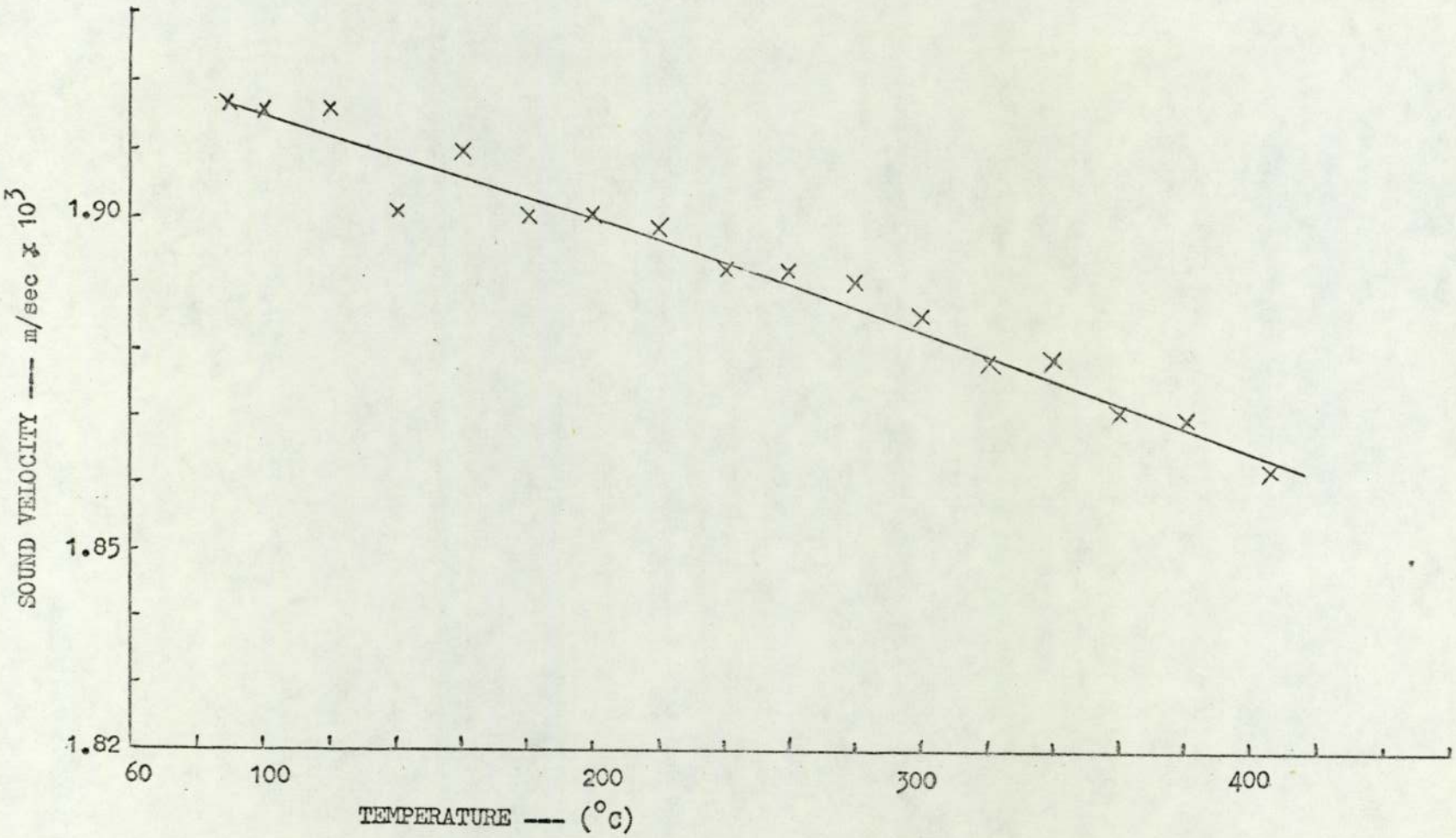


Fig. 7.4. Variation of sound velocity with temperature in Woods metal.

Woods metal: 50%Bi, 25%Pb, 12.5%Sn, 12.5%Cd.

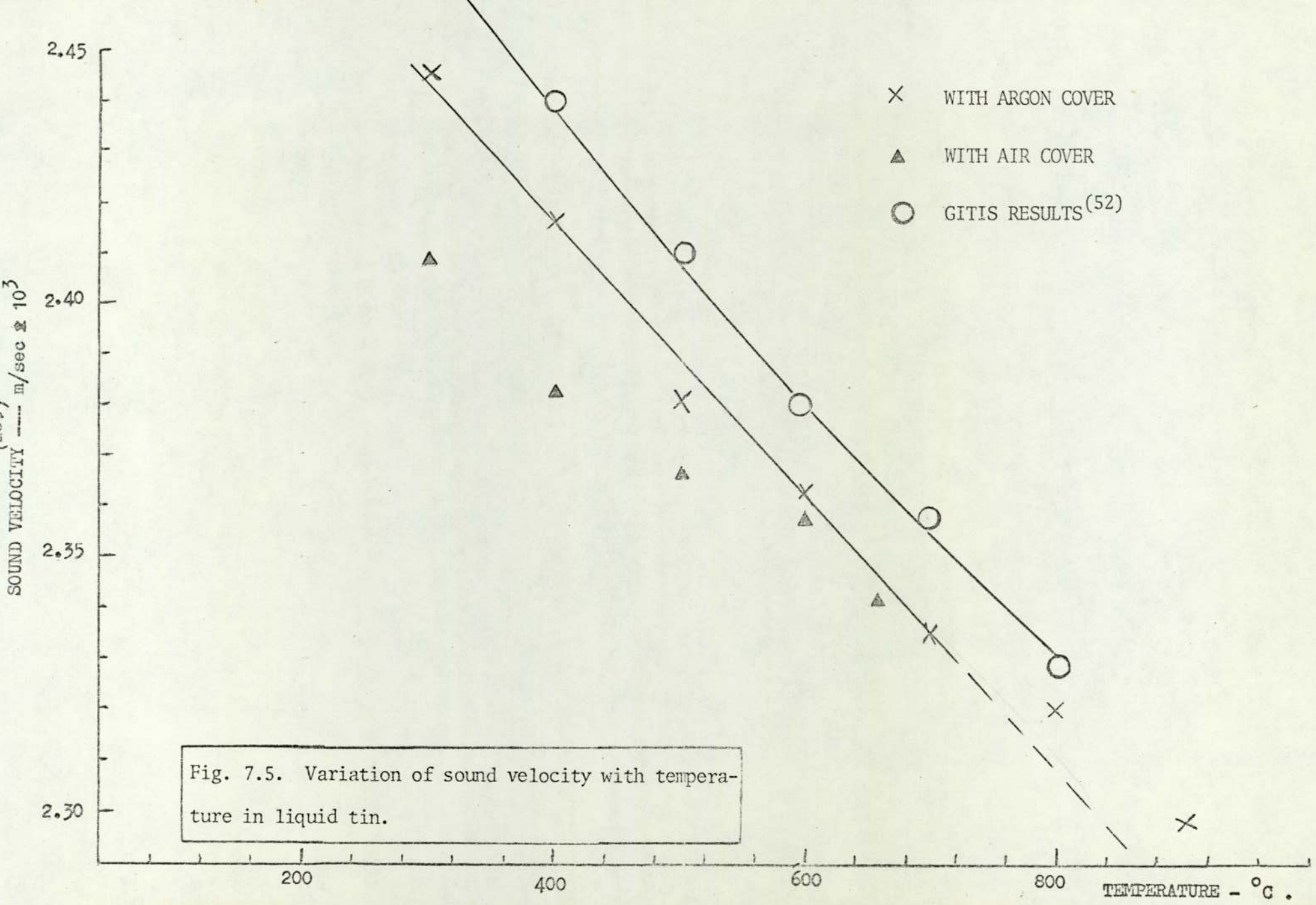


Fig. 7.5. Variation of sound velocity with temperature in liquid tin.

temperature coefficients in Woods metal and tin are $-0.17 m.sec^{-1}.deg^{-1}$ and $-0.25 m.sec^{-1}.deg^{-1}$ respectively. The results in tin agree with those obtained by Gitis et al.[52]

The same measurement in tin, where simple air melting had been used, was only possible up to 670°C, since the amplitude of the echoes began to fall noticeably as the temperature at the target area increased. As Fig. 7.5 shows, the sound velocity in tin, when the metal is melted in contact with air, is different from the velocity when an argon gas blanket is used. This change in velocity is probably due to the mass of minute oxide particles of tin and other impurities suspended in the liquid. Since the density of $SnO_2$ becomes greater than that of liquid tin at temperatures higher than about 400°C, it is suspected that the impurities rain down on the diaphragm, thus obscuring it. Certainly this would account for the severe fading which is observed at high temperatures. It must be pointed out that a similar problem may well recur with sodium where the densities are even more disparate (2.270/0.970).

## 7.5 NON-WETTING/IMPURITIES/REFRACTIONS

In the experiment using Woods metal, the liquid demonstrated its ability to wet the diaphragm immediately after melting. However, improvement in the echo amplitude by 70% was observed after some 10 hours - showing that the wetting was completed with time.

The amplitude of the echo signal from the 2mm target placed at various distances was first measured in a uniform temperature (100°C) and then in a temperature gradient (transducer temperature = 100°C, liquid at 15cm = 400°C). A 15% reduction in the echo amplitude was observed in the far field when the temperature had been increased from 100°C to 400°C. This was mostly attributed to the increase of bulk attenuation with temperature . A maximum echo amplitude was achieved when the target was at

about 5.5cm, the distance of the near field. The calculated length of the near field for 5MHz in 100°C Woods metal is 6.5cm.

When the temperature of all the liquid had stabilised to about 100°C, the liquid was stirred mechanically and an immediate large reduction in the signal strength was noted; the relative echo amplitude, when the 2mm target was at 20cm, dropped from 0.2 to 0.07 (ie about 10dB). The original amplitude was then only reached again some two hours after the liquid had been disturbed. Fig.7.6 shows part of a time record indicating the slow recovery of the echo amplitude. The record was obtained by the ultrasonic transit time monitor. It shows that the increase in echo amplitude has caused the detectable cycle of the signal to change from the second to the first, causing a 0.2μsec change in the transit time. The signal fading was thought to be due to inhomogeneities in the liquid caused by stirring and to scattering from suspended metal oxide, stirred in from the air-covered free surface. Some very small echoes from moving objects were in fact detected during this test and were also attributed to oxide particles. These particles in Woods metal could be any of the oxides given in Table 7.2.

TABLE 7.2

| Oxide | Density g/cc at R.T. | Melting Point °C |
|---|---|---|
| BiO | 7.15 | 700 to 860 |
| $Bi_2O_3$ | 8.1 to 8.9 | |
| $Bi_2O_5$ | 8.2 | |
| CdO | 6.95 to 8.15 | < 1400 |
| $Pb_2O$ | 8.3 | 888 |
| PbO | 8.0 to 9.5 | |
| $Pb_3O_4$ | 9.1 | |
| $SnO_2$ | 6.95 | > 1500 (or 2000) |

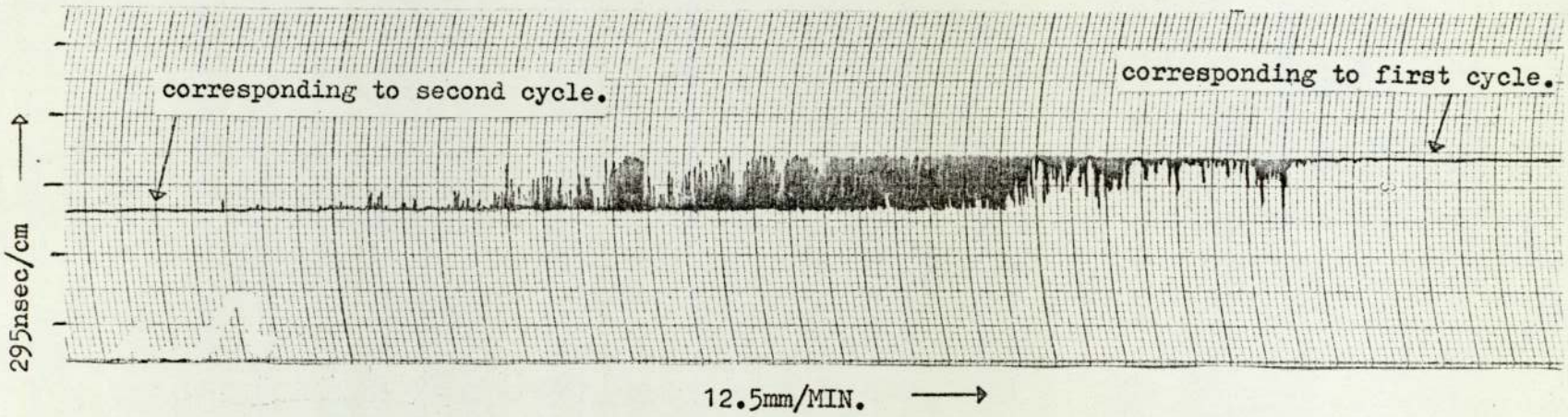


Fig. 7.6. Ultrasonic monitor output indicating slow recovery of echo amplitude in Woods metal after stirring the liquid.

During the tests with molten tin, it was found that the ability of the liquid to wet the steel diaphragm at temperatures between 232°C (melting point) and 280° (the maximum operating temperature of the transducer) was very poor. In the experiment with simple air melting, when the temperature at the diaphragm was 280°C and the temperature at 15cm from the diaphragm was 300°C, a small echo signal from the target at 15cm did not appear until one hour after the tin had been melted. This echo improved with time and some six hours after the diaphragm had been kept at 280°C the echo reached a reasonable amplitude.

The echo signal obtained at 300°C, however, started to fade when the temperature at 15cm was increased to above 450°C while keeping the transducer at the same temperature, 280°C. At 670°C the echo became extremely small and did not recover, even when the temperature returned to its original 300°C. This was attributed to a deposit of tin oxide on the face of the diaphragm. Fading at high temperatures occurred even when the diaphragm was pre-wetted completely with a layer of tin by means of phosphoric acid. The problem therefore could not be attributed to the non-wetting effect.

This high temperature problem in the liquid tin was solved by using an argon gas cover and a titanium rod to minimise oxide formation. Adequate echo signals from the target in the hot zone were obtained up to the maximum operating temperature of 900°C, which was held for several hours. Removal of the argon gas caused a loss in the echo signal after only a few minutes at this temperature. This again appears to be due to contamination of the melt. Some mechanical resistance could in fact be felt when a probe was inserted to within about 1mm of the diaphragm face, which suggests that a denser oxide had been deposited on the diaphragm face.

Some lens effect was observed during the tests with high temperature liquid tin. Table 7.3 shows the measured values of the echo amplitude from the target at 10cm on the axis of the vessel, for a range of temperatures up to 877°C. The measurement was started when the temperatures were 262°C at the bottom of the cylinder and 263°C at the target area. The temperature at the target area was increased gradually while the temperature at the bottom was kept between 250°C and 280°C by manually controlling the bottom heater and the air cooler.

The amplitude fluctuation of the echo, during the temperature increase (from 263°C to 877°C), was caused by the fluctuations in the temperature of the body of the narrow cylinder at the bottom of the vessel. This is clear in Table 7.3 which shows that a sudden increase in the air flow rate of the cooler causes an increase in the echo amplitude. This can be attributed to the change in the curvature of the thermal boundaries across the narrow cylinder and thus to their focusing effect.

TABLE 7.3: Variation in Echo Amplitude due to Lens effect in High-Temperature Liquid Tin

| | Temperature at vessel base (°C) | Temperature at target (°C) | Echo amplitude (volt) |
|---|---|---|---|
| | 262 | 263 | 1.2 |
| | 267 | 372 | 0.9 |
| Air flow increased → | 269 | 457 | 0.85 |
| | 262 | 485 | 0.9 |
| | 261 | 514 | 1.0 |
| | 264 | 545 | 0.9 |
| Air flow increased → | 265 | 584 | 0.9 |
| | 260 | 577 | 1.1 |
| | 251 | 590 | 1.25 |
| | 256 | 630 | 1.05 |
| | 263 | 661 | 1.0 |
| | 266 | 676 | 0.95 |
| | 270 | 695 | 0.9 |

Table 7.3 cont.

| | Temperature at vessel base (°C) | Temperature at target (°C) | Echo amplitude (volt) |
|---|---|---|---|
| Air flow increased → | 274 | 712 | 0.8 |
| | 268 | 681 | 0.95 |
| | 264 | 726 | 1.0 |
| | 271 | 762 | 0.8 |
| | 277 | 784 | 0.65 |
| Air flow increased → | 281 | 798 | 0.55 |
| | 261 | 776 | 1.0 |
| | 247 | 773 | 1.3 |
| | 244 | 775 | 1.4 |
| | 248 | 823 | 1.2 |
| | 258 | 867 | 0.8 |
| | 262 | 877 | 0.6 |

## 7.6 TEMPERATURE FLUCTUATIONS

If temperature fluctuations occur within the bulk of the liquid in the cooling tube, fluctuations in echo amplitude and echo delay are to be expected, since the sound velocity changes noticeably with temperature. The amplitudes of the echo fluctuations depend in turn on the amplitudes of the temperature oscillations and the temperature coefficient of the sound velocity in the liquid. Similar random fluctuations can occur in the acoustic field propagating through the oceans (Clarke 1974)[53]. This has been related to the interfacial wave separating two media of different sound velocity.

In order to examine this phenomenon, temperature fluctuations were promoted in the Woods metal experiment. The cylinder was heated at the bottom and cooled at the top in order to promote free convection currents The temperature oscillations were then measured by the thermocouple in the cylinder and recorded on the chart recorder. The graph in Fig. 7.7

shows the average temperature profile along the axis of the cylinder when the temperature had stabilised at 175°C at the base and 131°C at the top. Fig. 7.7 also shows the maximum amplitude of the temperature oscillations at various distances along the axis of the cylinder.

The fluctuations in the transit time of the echo when the target was fixed at 20cm were also recorded on the chart recorder of the apparatus. The electronic system used here is the same as that designed for measuring change in bubble echo delay (Chapter 5).

Fig. 7.8 shows the record of the echo delay fluctuations and the simultaneous temperature oscillations. It can be seen that the fluctuations in both the temperature and echo delay are random. This is due to turbulence produced by the current of hot liquid (175°C) rising from the bottom of the cylinder along the ultrasonic beam and mixing with the cold liquid (131°C).

Similar experiments in water showed much larger fluctuations in the echo delay at temperatures below 60°C. This is due to the larger temperature coefficient of the sound velocity in water below 60°C and to the lower thermal conductivity. The average temperature coefficient of sound velocity in water[30] is $+2.9\ m.sec^{-1}.deg^{-1}$ at 20°C but zero at 75°C, while the measured value between 70°C and 400°C in Woods metal is constant at $-0.17 m.sec^{-1}.deg^{-1}$.

Provided that convection does not produce turbulence in the liquid, there is an apparent correlation between the amplitudes of the temperature oscillations and the echo delay oscillations, as seen in Fig. 7.9. This was observed in water when the temperature at the base of the cylinder was 20°C and the water above 15cm was just below boiling point. The target was at 10cm. In these conditions, the strong free convection at the top, between the heater at 15cm and the water surface,

produced some small temperature oscillations below the target. Fig. 7.9 shows that the maximum temperature oscillation was about 1°C which caused some 120 nsec oscillation in the echo delay.

In the experiment using water with small temperature oscillations, the echo delay oscillations became negligible when the temperature at the top decreased to 80°C, while the temperature at the bottom remained at 20°C. Under these conditions, the slight movement of a narrow wire in the water near the wall of the vessel produced a short oscillation in the echo delay as well as in the temperature, as shown in Fig. 7.10. This was probably due to induced stable oscillations of the isothermal boundaries in the liquid with temperature gradient. A similar test in Woods metal showed only a small effect, probably due to the higher thermal conductivity.

A cursory glance at Figs. 7.8, 7.9 and 7.10 will reveal a similarity between the frequencies of oscillations in echo delay and temperature over part of the record. A correlation may, therefore, be found between the frequencies of oscillations in echo delay and the velocity of convection currents in the liquid bulk.

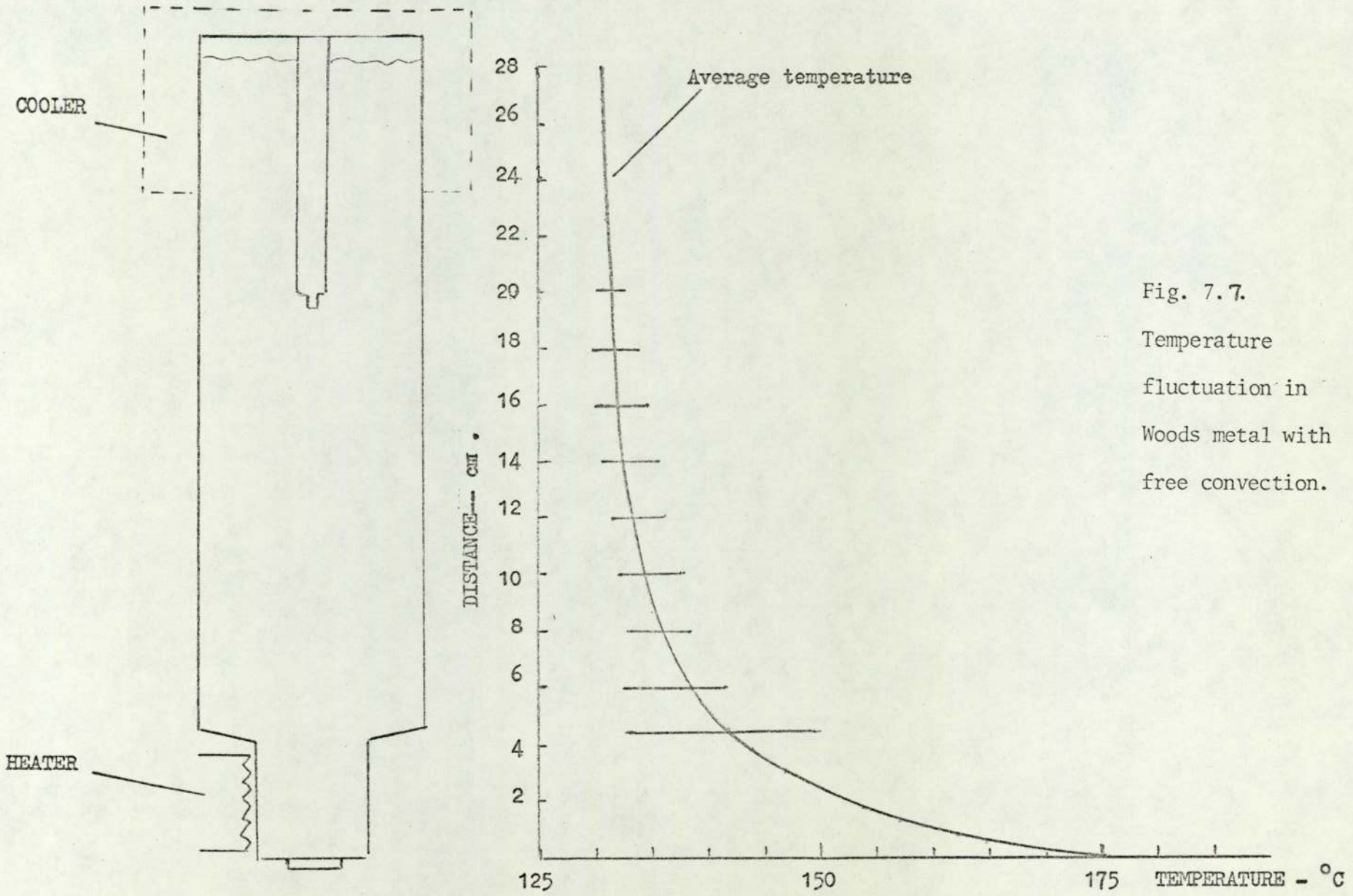


Fig. 7.7.
Temperature fluctuation in Woods metal with free convection.

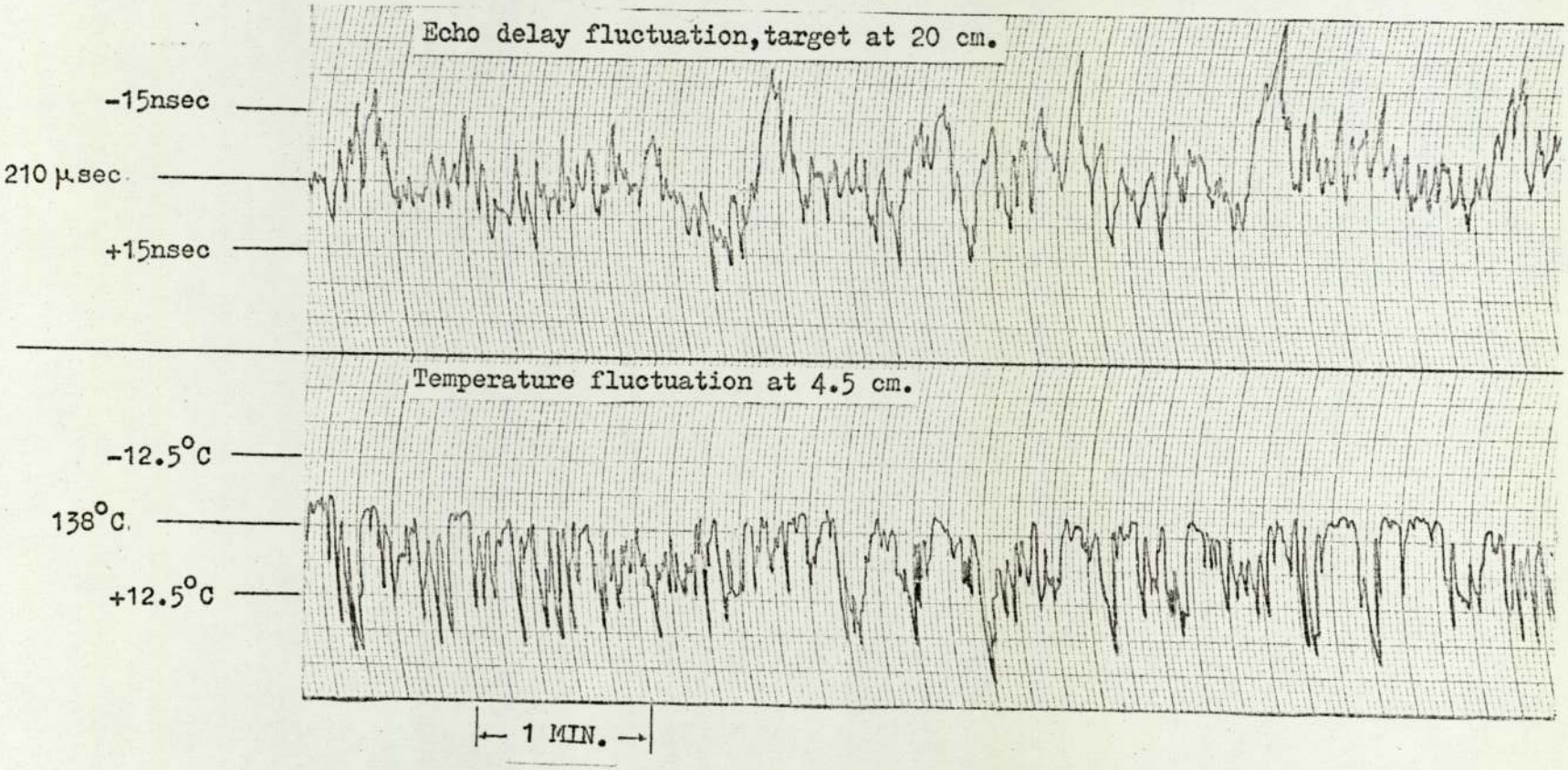


Fig. 7.8, Time record of echo delay fluctuations and simultaneous temperature oscillations in Woods metal with free convection.

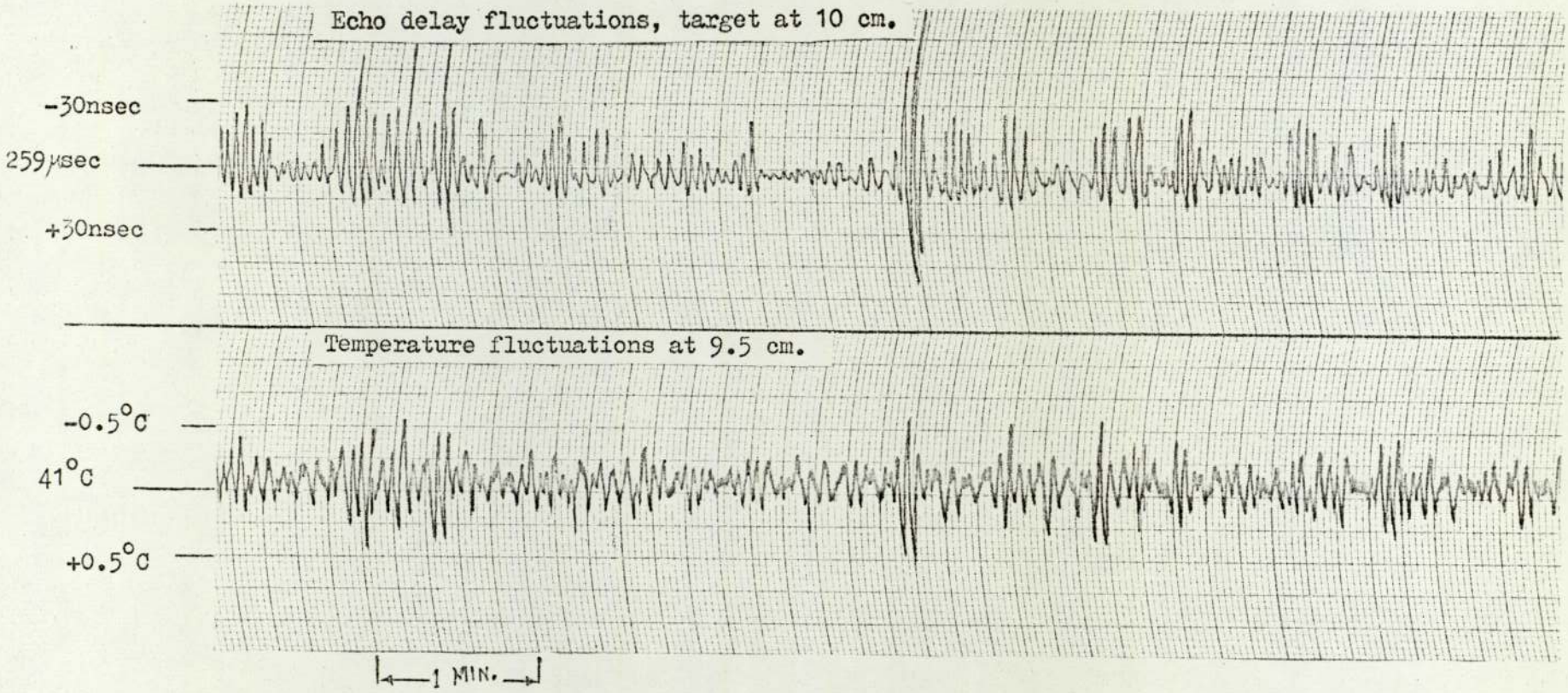




Fig. 7.9. Time record of echo delay fluctuations and simultaneous temperature oscillations in water with small convection current at target area.

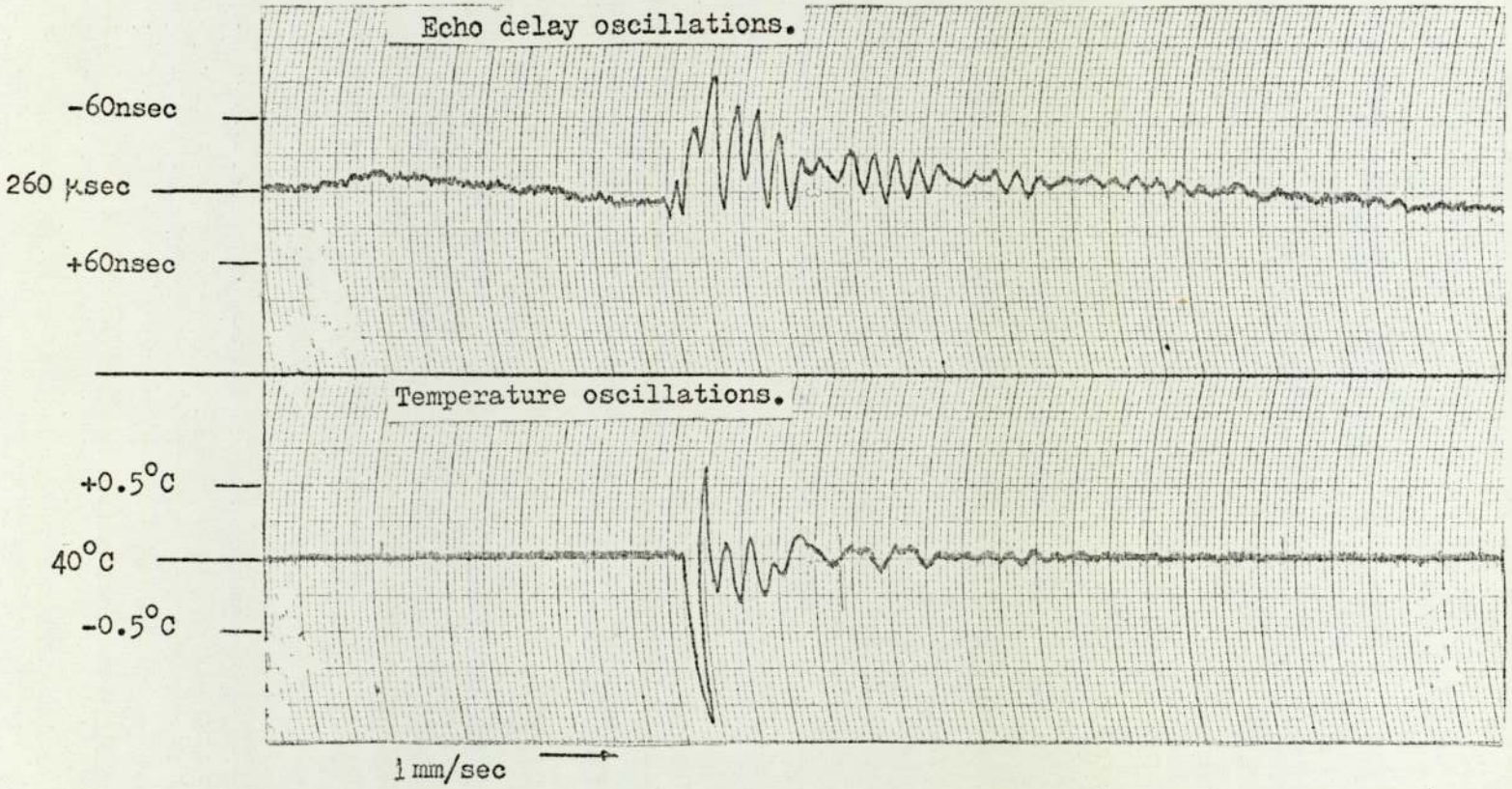


Fig. 7.10 Time record of a short oscillation in echo delay and simultaneous temperature in water with stable temperature gradient, disturbed by the short movement of a narrow wire.

# CHAPTER 8

# CONTROL SYSTEM OF BUBBLE GROWTH AND COLLAPSE CYCLE

## 8.1 INTRODUCTION

In the planned experiments with the sodium pool, vapour bubble growth is initiated by the rod withdrawal technique. Argon released from a small high-pressure reservoir then collapses the bubble . The rod is actuated by a solenoid magnet and the collapse system uses a high-speed valve. The bubble growth and collapse rates are measured by the ultrasonic monitor, two transducers being available for simultaneous viewing from two directions at right angles.

The solenoid-actuated rod and the high-speed valve have to be capable of operating together with short and consistent response times. The valve must operate within a few milliseconds of the rod, since the predicted bubble growth time is a few milliseconds. The high-speed valve must also have a short opening time of a fraction of a millisecond in order to generate a near step-function of pressure of a very short rise time. This pressure increase causes the growing bubble to collapse in a few milliseconds.

The short response times required for this experiment cannot be obtained from solenoids and valves available commercially. However, the combination of a bubble nucleation rod using a commercial solenoid and a specially designed, pneumatically-energised, high-speed valve has enabled a satisfactory design to be produced. Their individual response times are rather long, but when operated together their consistency gives the required short time interval between the action of the rod and that of the valve. The individual performance of each instrument and their

sequence of operation are described in this chapter.

## 8.2 BUBBLE NUCLEATION DEVICE

A schematic diagram of the bubble nucleation rod for water analogue experiments is shown in Fig. 8.1. The rod, made of stainless steel and 1mm in diameter, is contained within a stainless steel tube of 1.5mm bore. The tip of the rod, which before operation protrudes 1mm from the mouth of the tube, can be withdrawn by the solenoid to a retracted position 1mm inside the tube, to give the rarefaction which initiates the bubble. The upper end of the rod joins the solenoid plunger body through a rubber gasket which seals the upper end of the tube. In the actual sodium pool experiment, a bellows replaces the rubber gasket. The force on the plunger from the extension of either the rubber gasket or the bellows affects the operation of the solenoid. This force becomes quite considerable when the static pressure inside the pool is not equal to the atmospheric pressure.

The magnetic force of the solenoid, therefore, has to be large enough to compensate for the load on the plunger and also to withdraw the rod at the required speed. The commercial solenoid chosen for this purpose is a 24VDC N.S.F., type 5SF.

The rod is energised when an input DC voltage signal has been applied to the coil of the solenoid. Due to the build-up time of the current in the coil, there is a delay between applying the input voltage and the commencement of the plunger movement. After this delay, the plunger starts to move at a low speed, and completes retraction at a high speed - the magnetic force increases as the plunger moves towards the core of the solenoid. It is expected, therefore, that the vapour bubble will start to grow once the rod is fully retracted. Thus, the sum of the delay time and the retraction time of the plunger is the response time of the

bubble nucleation device. This response time depends on : (i) the characteristics of the solenoid, (ii) the stroke distance, (iii) the amplitude of the input DC signal, (iv) the mechanical force on the plunger.

The operating time of the nucleation device has to be measured under a variety of conditions within the pool in order that allowance can be made for the time-interval required between bubble formation and collapse. This time-interval is the time in which a bubble is allowed to grow before the collapse mechanism is started.

The response was measured using a linear variable displacement transducer(LVDT). The fastest possible operating time of the solenoid plunger, without the loading of the nucleation rod, using the maximum allowable input voltage for 2mm stroke was approximately 6msec. With the plunger attached, this was increased by only 3.5msec.

For each experiment in the sodium pool, a method of measuring the exact response time of the nucleation device under experimental conditions is needed. A simple method was found from observing the solenoid current.

The solenoid has two different inductances $L_1$ and $L_2$ for the two extreme positions of the plunger, the resting position and the retracted position respectively. When a d.c. signal is applied the current builds up with initial time constant $L_1/R$, where R is the resistance of the coil. Fig. 8.2 shows the behaviour of the current. After a certain delay time $t_d$, the plunger starts to move and so causes the build-up current to drop to a minimum point M, due to the increase in inductance. When the plunger reaches the fully retracted position after a further time $t_r$, the current starts to build up again with a new time constant $L_2/R$. Thus, at the minimum point M in the current signal, retraction of the

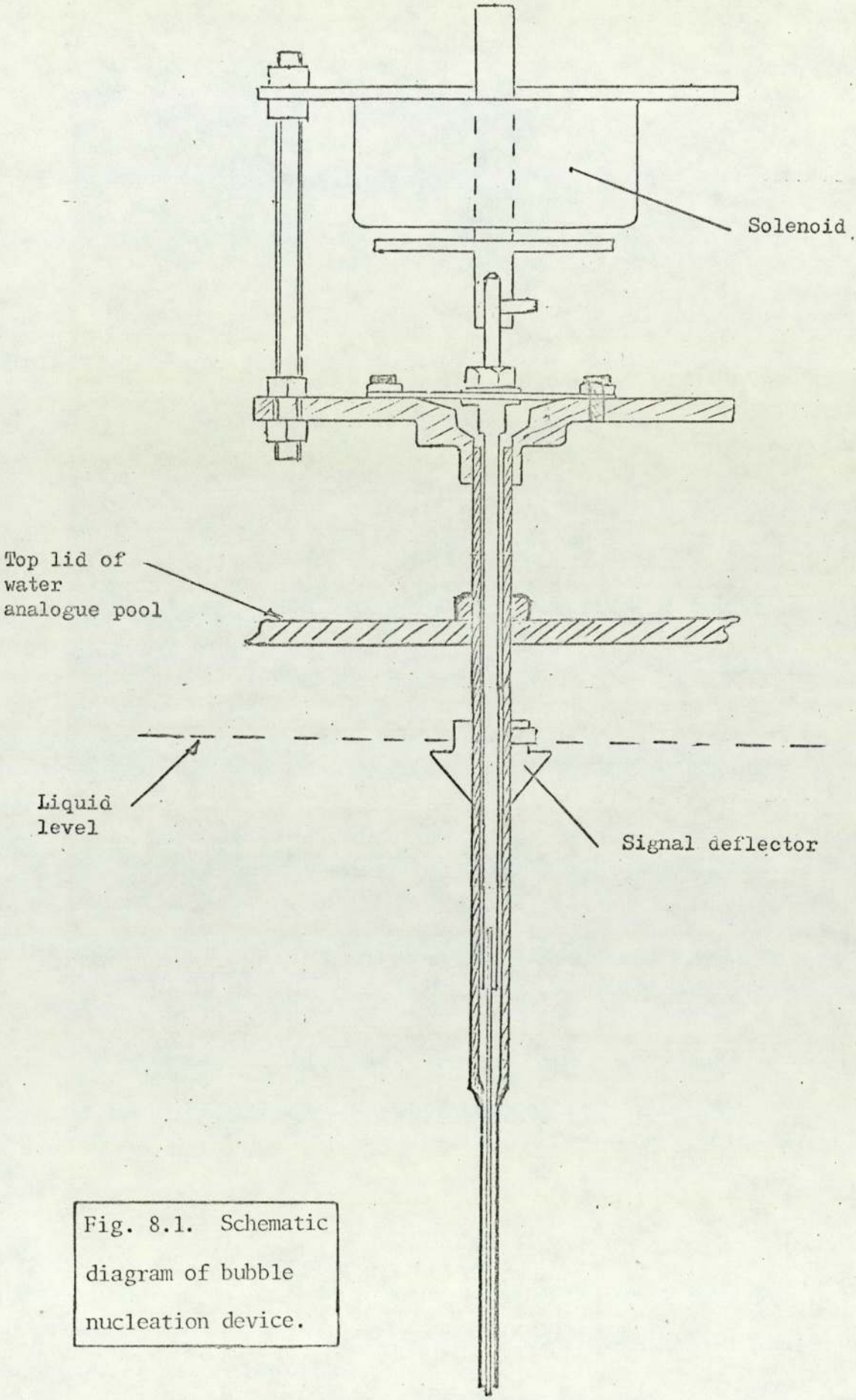


Fig. 8.1. Schematic diagram of bubble nucleation device.

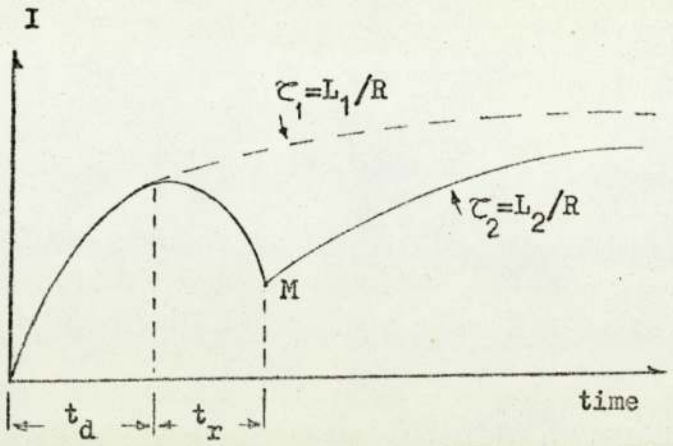


(a)

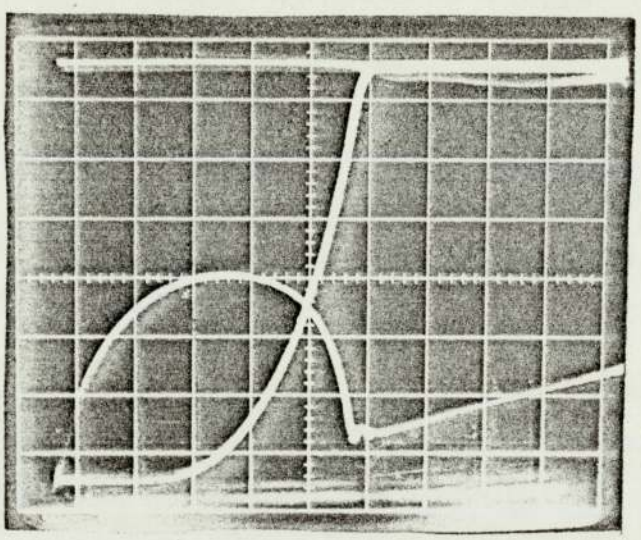

(b)
displacement:
0.25 mm/CM .

Fig. 8.2. Measurement of response time of nucleation device; (a) solenoid current signal; (b) comparison of displacment transducer output and current signal.

solenoid-actuated rod is complete. The current signal was detected by placing a very low resistance in series with the coil of the solenoid. The results are consistent with those obtained from the displacement transducer. The technique allows the measurement to be obtained in the high-temperature environment above the pool where the usual displacement transducer cannot be used.

## 8.3 HIGH-SPEED VALVE

The bubble collapse system requires a valve with a very short opening time in order to generate in the pool a rapid pressure increase up to 1 atm. Although it is impossible to generate a perfect step function, it was thought that for the present operation a pressure ramp function with a duration of a fraction of a millisecond would be acceptable.

Such a ramp can be generated easily by the burst diaphragm technique used in shock tubes. This technique involves mounting a frangible diaphragm between two volumes of gas at different pressures and then rupturing the diaphragm by means of a puncture mechanism[19]. The technique, however, is neither reliable nor practical for use in a sodium pool, especially with the requirement for repeated experiments and safety.

An alternative to the burst diaphragm technique is the use of electro-magnetic valves. Most of the electro-magnetic valves available commercially, however, have long opening times due to the build-up time of the current in the solenoid magnet. It was therefore necessary to design a high-speed automatic valve.

The high speed required was obtained by a valve with an orifice diameter of 0.5"; this operates through the impact of a projectile in the form of a fast-moving 1" ball-bearing projected by gas pressure[54], as shown in Fig. 8.3. The flight-tube carrying the ball has a length of 40cm and an

inside diameter slightly larger than that of the ball. The valve assembly closes the top end of the flight tube where vent holes have been made to allow the escape of pressurised air above the projectile. The lower end of the flight tube is connected to a gas line (eg a high pressure air supply) which is closed by a magnetic valve with a large orifice. The slow opening time of the magnetic valve has no effect on the performance of the main valve. When the magnetic valve is closed the ball-bearing remains at the bottom of the flight tube, thereby closing it.

Thus, the ball shoots from the lower end of the flight tube to the top and strikes the plunger of the valve assembly. The valve opens in less than 1msec and the restoring force of a spring closes it after some 20msec. After impact, the ball returns freely to the lower end of the tube since the drive gas is no longer applied.

The kinetic energy of the moving ball at the moment of impact is much greater than that required to open fully the valve against the force of the spring. The excess energy at the moment of impact increases the speed of the valve. Since the time during which the valve remains open cannot be specified precisely, a small reservoir (about 10cc) containing high-pressure argon gas is used, and the known amount of gas fed through to the pool during the valve operation. The reservoir is actually incorporated in the valve assembly and its volume can be adjusted over a range of capacities. Before each test the reservoir is pre-charged with argon gas of 100-300psi ($lbf/in^2$). Experimental results show that a pressure of 150psi is sufficient for the required final pressure in the pool, when the volume of the gas blanket above the liquid level is approximately 100cc.

The opening speed of the valve can be calculated approximately by know-

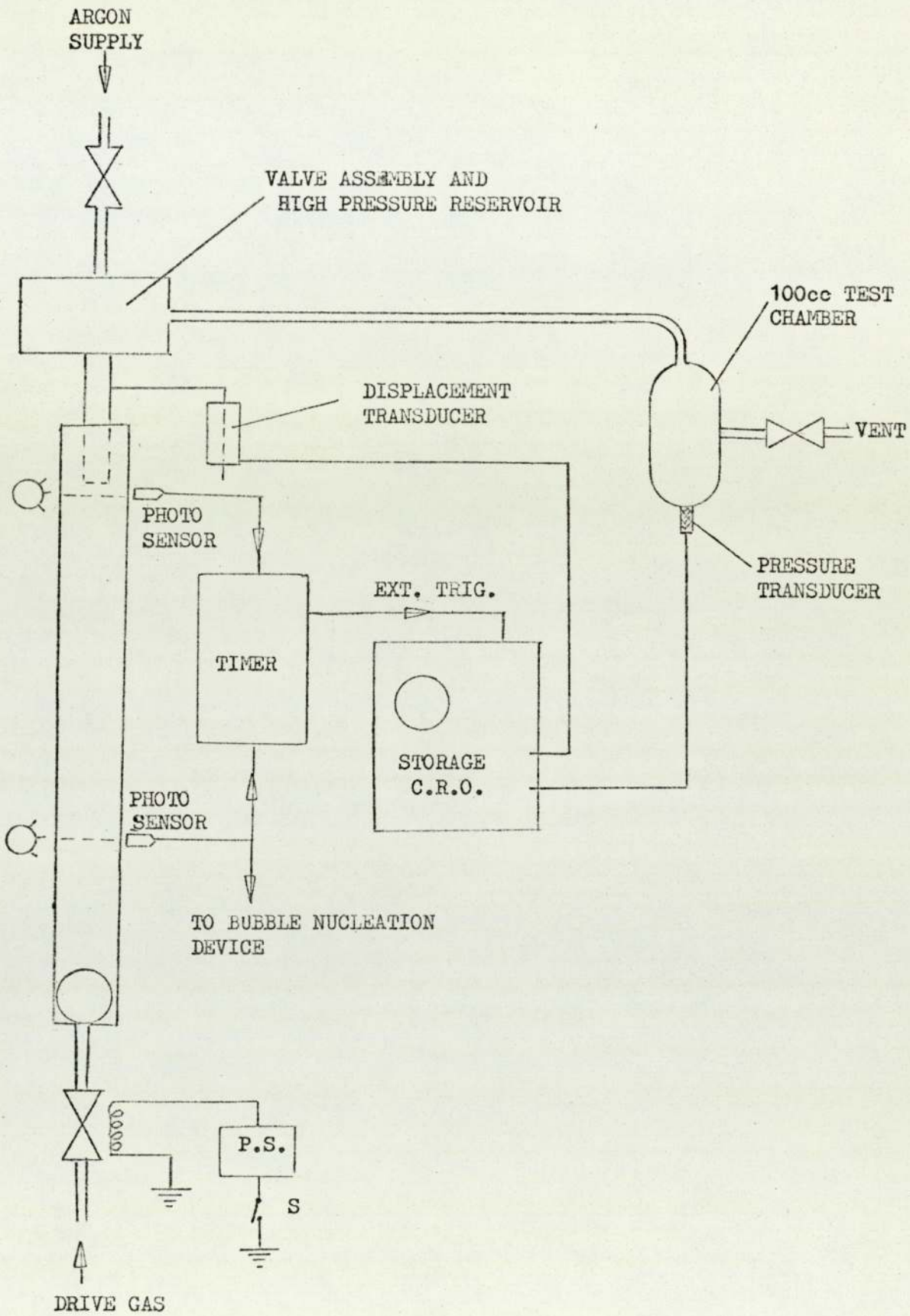


Fig. 8.3. Initial design of system for introducing a step increase in pressure to cause bubble to collapse.

ing the ball speed at the moment of impact and the mass of the ball and plunger. According to the principle of the conservation of momentum, it can be written approximately

$$V_p \simeq \frac{m_B}{M_p+m_B} V_B$$

where $V_p$ is the plunger speed, $V_B$ the ball speed, $m_B$ and $M_p$ are the mass of the ball and plunger respectively. $V_B$ varies with the pressure of the drive gas. It will be noted that unlike the case of a solenoid actuator, the velocity of the plunger is acquired almost instantaneously by the impulse of the projectile.

### 8.3.1 Valve Trials

The high-speed valve is vital to the safety of the system and extensive tests have been carried out to establish its performance and reliability. Fig. 8.3 shows the test arrangement to measure the ball speed, the opening speed of the valve and the rise time of the pressure signal of the high-pressure argon gas released into the 100cc test chamber.

In order to measure the speed of the ball projectile, the flight time of the ball was measured by means of two fast response photo-sensors, 30cm apart and mounted onto the side of the flight tube, one at the top close to the valve and the other a few centimetres above the resting place of the ball. The photo-sensors will also be used for the combined operation of the bubble nucleation device and the valve. Each photo-sensor is illuminated by a narrow beam of light emitted by a 12 V lamp through two holes across the flight tube, as shown in Fig. 8.3. The moving ball cuts the two beams of light and therefore two signals are generated by the two photo-sensors. The time interval between the two signals is measured and recorded by an electronic digital timer.

The flight time variation due to change in the pressure of the drive

gas is presented by the graph in Fig. 8.4. For low pressures of up to 8psi the ball does not reach the other end of the flight tube and thus does not open the valve. The flight time for pressures above 8psi decreases with pressure. During the measurement it was found that the flight time for pressures of more than 15psi was consistent with a maximum variation of 0.4msec. At a range of more than 15psi the flight time was less than 40msec. Due to the combined operation of the bubble nucleation and collapse devices, the flight time should be long enough to span the response time of the bubble nucleation device and the bubble growth time. It was estimated that a flight time of not less than 25msec is adequate for the operation.

Using the graph in Fig. 8.4, the average speed of the ball projectile along the last 30cm can be calculated for various pressures of the drive gas. This is represented by one of the graphs shown in Fig. 8.5. The second graph in this figure shows the valve speed at the moment of impact. This speed was measured by using a displacement transducer, type LVDT, as shown in Fig. 8.3. From Fig. 8.4 it is concluded that an increase in pressure of the drive gas above 22psi no longer increases the valve speed. Thus the pressure of the drive gas was limited to 22psi, the pressure at which the maximum valve speed (2mm/msec) is achieved immediately after impact.

In order to ensure that the valve was capable of producing the required fast pressure increase, the valve was joined to a test chamber with a volume equal to the volume of the gas blanket in the pool, ie approximately 100cc. The valve can be linked to the chamber by a length of pipe. The pipe line produces a delay time between the valve action and the pressure signal received in the chamber, due to the transit of the pressure wave at the speed of sound. It also causes the gas system, in the pipe and the chamber, to oscillate[55]. This oscillation is a

function of the chamber volume and the pipe length . Due to the high temperature involved in the sodium pool and the required safety precautions a short pipe line between the valve and the pool is impractical. The minimum length possible for the pipe is approximately 70cm.

The output of the pressure transducer mounted on the test chamber and the output of the displacement transducer attached to the valve plunger were recorded on a storage oscilloscope. Fig. 8.6 shows the typical signals received for valve movement and pressure increase in the chamber. In each photograph in this figure the upper signal is the output of the displacement transducer and the lower signal the output of the pressure transducer. The pressure of the drive gas (air supply) was 20psi.

The signals in Fig. 8.6(a) were obtained when the reservoir was charged with 300psi argon gas and show that 15psi increase in the pressure of the 100cc chamber was achieved in less than 1msec. Similar signals appear again in Fig. 8.6(b) when the initial pressure of the reservoir is 150psi. As is expected, the final pressure in the chamber is proportional to the initial pressure of the reservoir. The low frequency oscillations in the pressure signal are the gas system oscillations. The high frequency noise at the beginning of the pressure signal is due to the mechanical shock caused by the impact of the steel ball inside the flight tube and received by the pressure transducer through the pipe body. The mechanical shock noise was reduced considerably when a rubber tube was fixed at the joint between the pipe and the valve, compare the signals in Figs. 8.6a and b. In Fig. 8.6b it is also clear that there is a delay time of approximately 2msec between the commencement of the valve movement and the pressure increase in the chamber.

From the results obtained in this initial test, it is concluded that the rise time of the pressure signal depends on the opening time of the valve

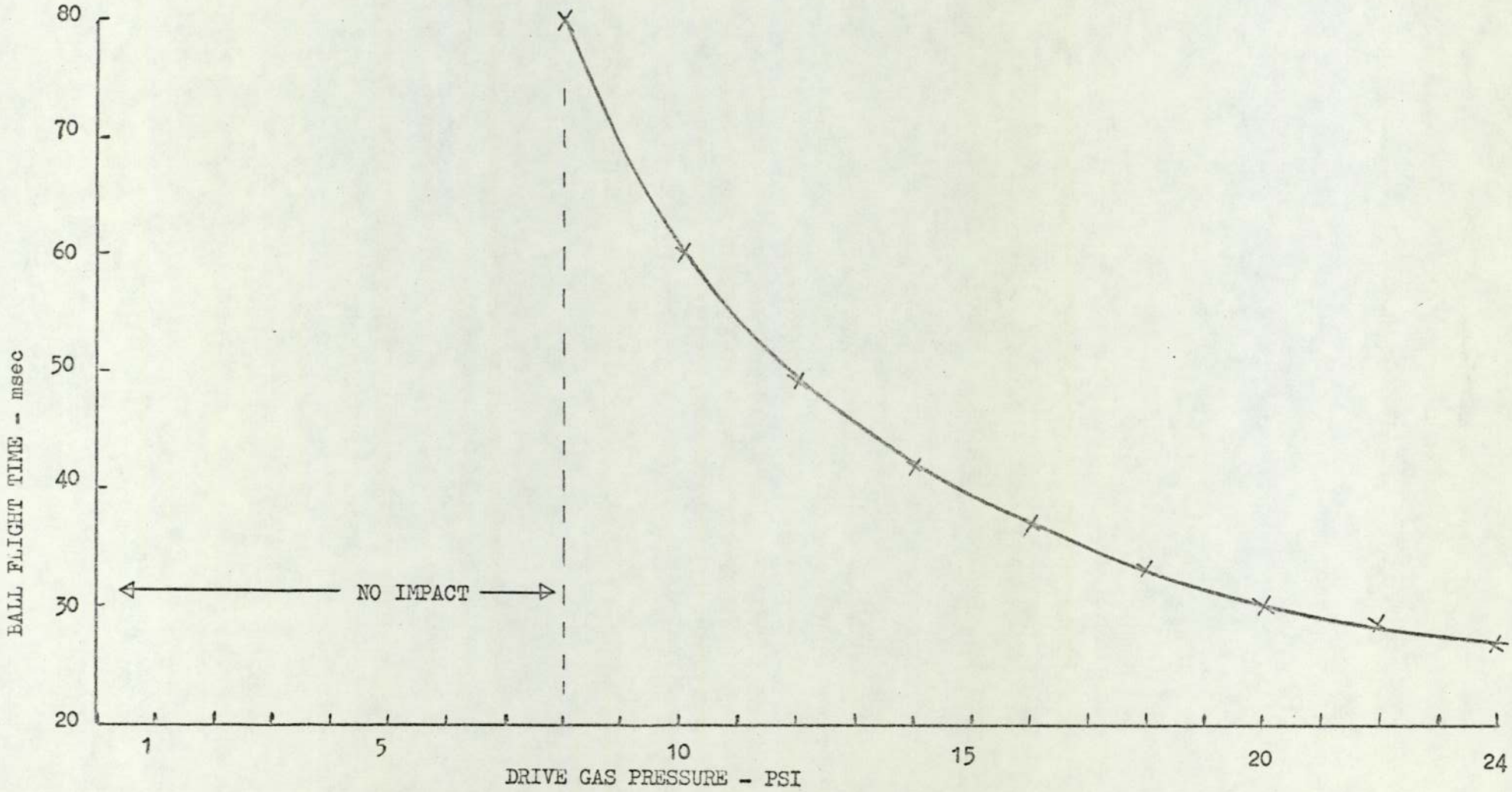


Fig. 8.4. Flight time of ball projectile versus drive gas pressure

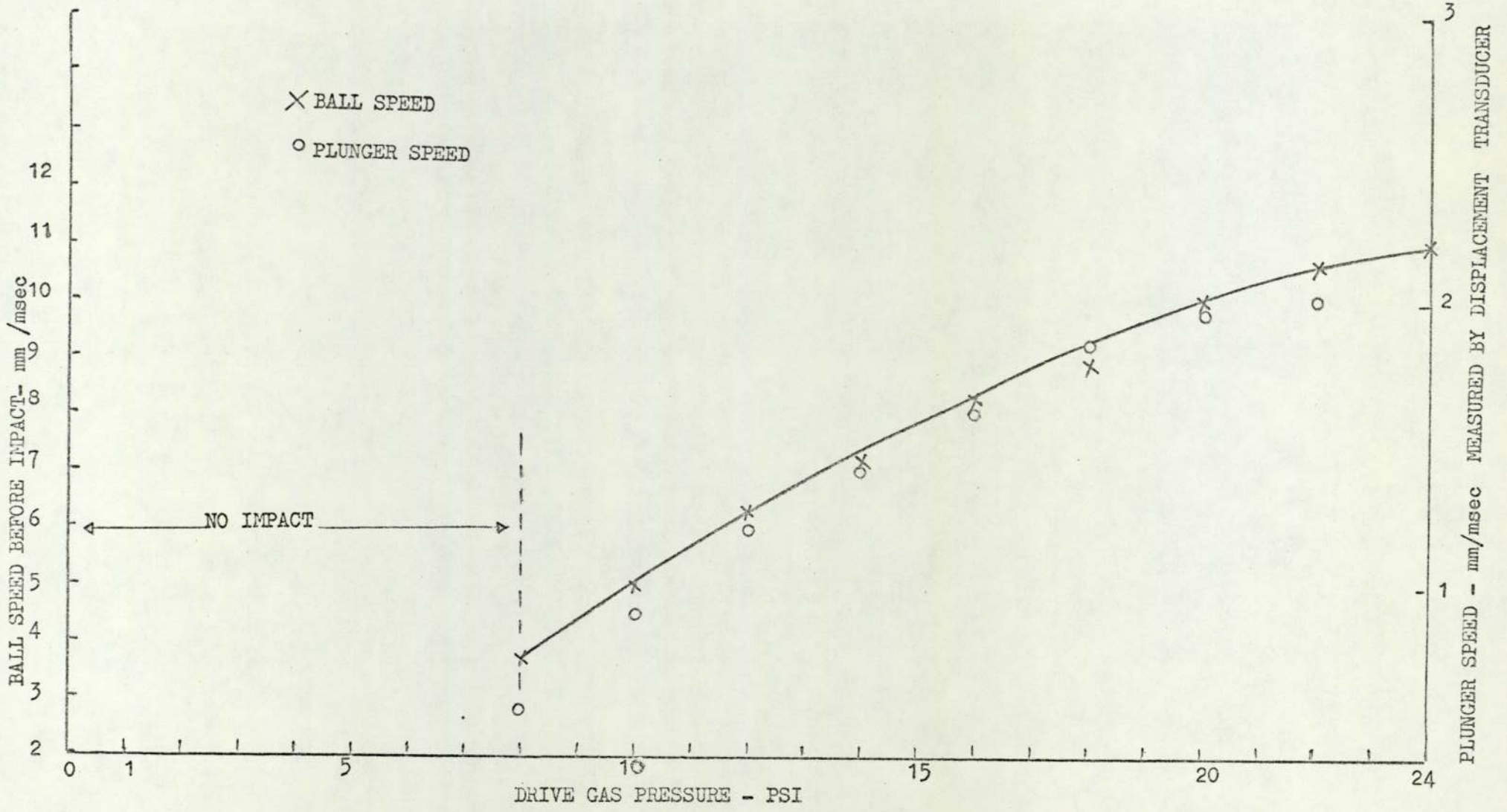


Fig. 8.5. Ball projectile speed before impact versus drive gas pressure.

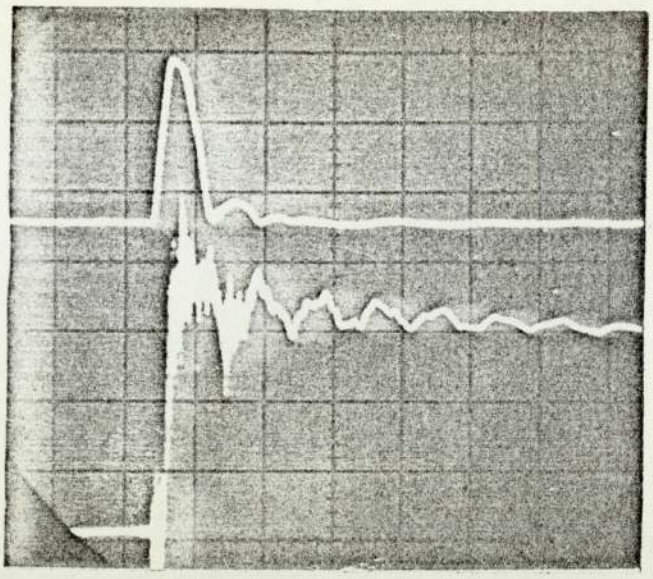

(a) Upper trace: 2mm/CM
Lower trace: 3 PSI/CM
initial pressure in
reservoir: 300 PSI.

10 msec/CM

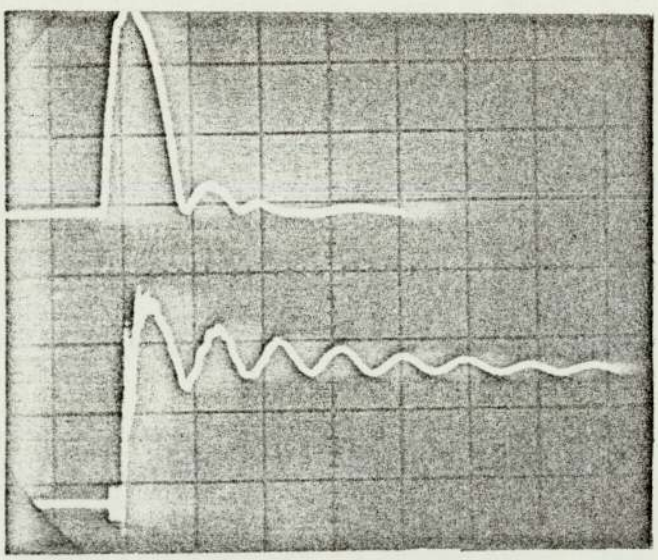

(b) Initial pressure in
reservoir: 150 PSI.

10 msec/CM

Fig. 8.6. Signals showing characteristics of motion of high-speed valve, obtained by LVDT displacement transducer, and of rapid pressure rise in a 100cc test chamber, using a Kistler pressure transducer, type 7001. Upper trace: valve motion; lower trace: pressure signal.

for the first 1mm displacement. Thus, the rise time of the pressure increase can only be improved by increasing the valve speed. The one millisecond achieved in the initial design was subsequently improved to 0.3msec by reducing the mass of the plunger assembly.

## 8.4 OPERATIONAL SEQUENCE OF SYSTEM

Fig. 8.7 shows the schematic diagram of the apparatus used for the nucleation and collapse of a single vapour bubble in the pool and for the bubble size measurement. The electronic units used to control the system and to measure the rate of growth and collapse are represented by the block diagrams.

As shown, the high-pressure reservoir of the high-speed valve is linked to the top of the pool by a long pipe of 70cm. The gas expansion pressure wave is detected by a pressure transducer mounted at the top of the pool. The bubble nucleation rod is energised by a signal received from photo-sensor A of the high-speed valve through an electronic delay unit. The flight time of the ball projectile is recorded on an electronic digital timer which receives two signals from the two photo-sensors of the valve, as was explained in Section 8.3.

The bubble size during growth and collapse will be measured in two directions by two ultrasonic monitors consisting of the two transducers attached to the base and the side of the pool.

The sequence of the whole operation is explained with the aid of the waveforms diagram in Fig. 8.8. Each signal has a number which corresponds to a numbered point on the block diagram in Fig. 8.7. The operation starts with signal (1) which is generated by the valve trigger unit (1) once switch S is closed. Signal (1) energises the magnetic valve A and the drive gas shoots the ball-bearing of the high-speed valve along the flight tube. Photo-sensors A and B generate two signals (2) and (3) as

the ball projectile cuts across the beams of light A and B.

The length of signal (4) represents the flight time recorded by the electronic timer and the magnetic tape recorder.

Signal (5) is generated by the electronic delay unit, which is designed to produce a given delay between pulse (2) and pulse (6). Pulse (6) is the drive-pulse for the solenoid of the bubble nucleation rod. The rod displacement is similar to signal (7). The response time of the solenoid-actuated rod is also clear from the solenoid current signal (8).

Initial experimental results show that the designed high-speed valve generates a ramp function of pressure similar to signal (9), see section 8.3.1. It was also found that the rapid pressure rise in the pool occurs with approximately 2 msec delay after signal (3), due to the transit of the pressure pulse along the pipe line.

Signal (10) shows that the bubble growth commences once the solenoid-actuated rod is fully retracted after time $t_R$. The bubble grows in size up to the moment of the fast rising pressure signal in the pool. For each test it is necessary to measure the exact $t_R$ of the nucleation rod by observing the solenoid current signal (8). It is clear that the growth time of the bubble can be selected and controlled by delay signal (5) which is adjusted according to the flight time of the ball projectile in the high-speed valve.

The output of the ultrasonic monitor is recorded on the storage C.R.O. for each test. Signals (4), (8), (9) and (10) are recorded on the magnetic tape-recorder to enable a comparison of the actual and predicted bubble growths to be made. The results can be reproduced at low speed on a multi-channel X-Y recorder.

Details of the circuits to control the operational sequence are given in Fig. 8.9. The signals produced by the two photo-sensors (type BPY13) are amplified using fast switching transistors. The purpose of the logic circuits is to detect the two signals when the ball projectile moves upwards. The clock pulse starts with the first signal and stops with the second; the flight time is then recorded on the digital counter.

For each measurement, switches $S_A$ and $S_B$ are first closed at position (1) in order that the delay time required can be preadjusted. When the switches are at position (2) the solenoid is actuated at the end of the predetermined delay time.

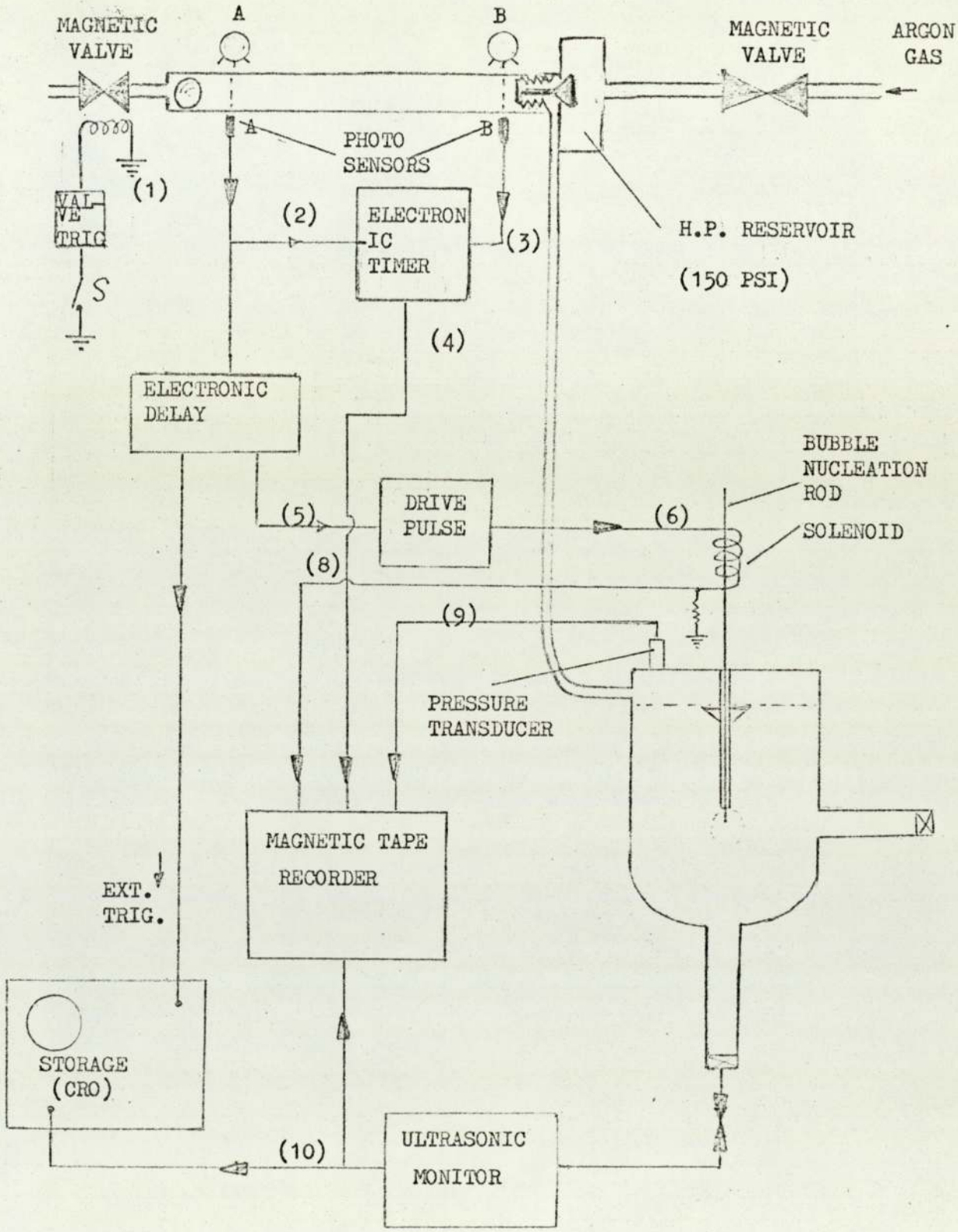


Fig. 8.7. Control system for measurement of bubble growth and collapse rate. The numbers refer to the waveforms shown in Fig. 8.8.

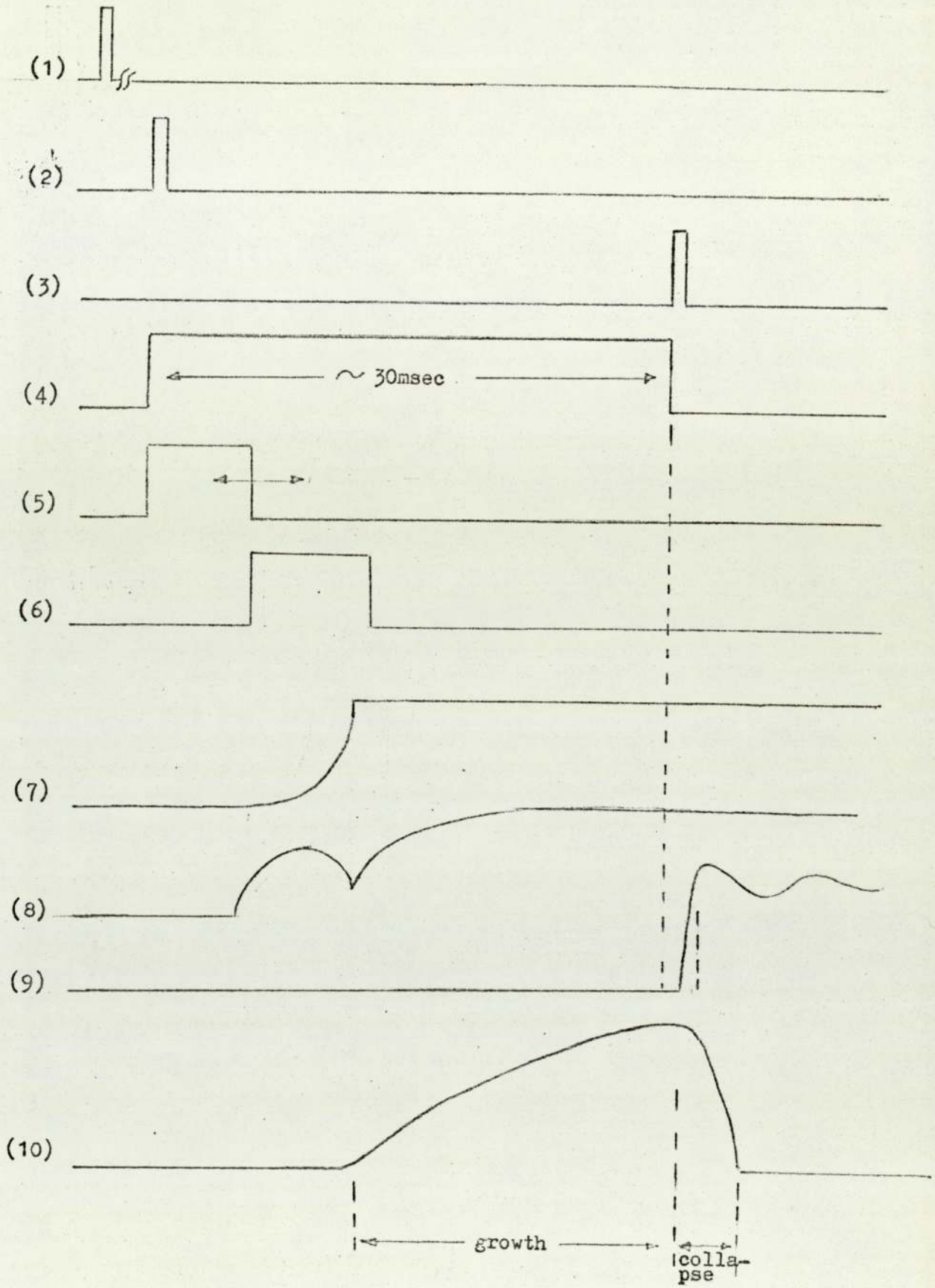


Fig. 8.8. Waveform diagram of operational sequence of system for bubble growth and collapse.

Fig. 8.8. The projectile sets off at the onset of the air trigger (1). It interrupts the first light beam, initiating a signal (2), which, after delay (5), triggers the solenoid, forming the bubble. By the time the projectile reaches the gas inlet valve, the bubble growth is virtually complete (10) and the increase in pressure in the reservoir (9) terminates the sequence, collapsing the bubble.

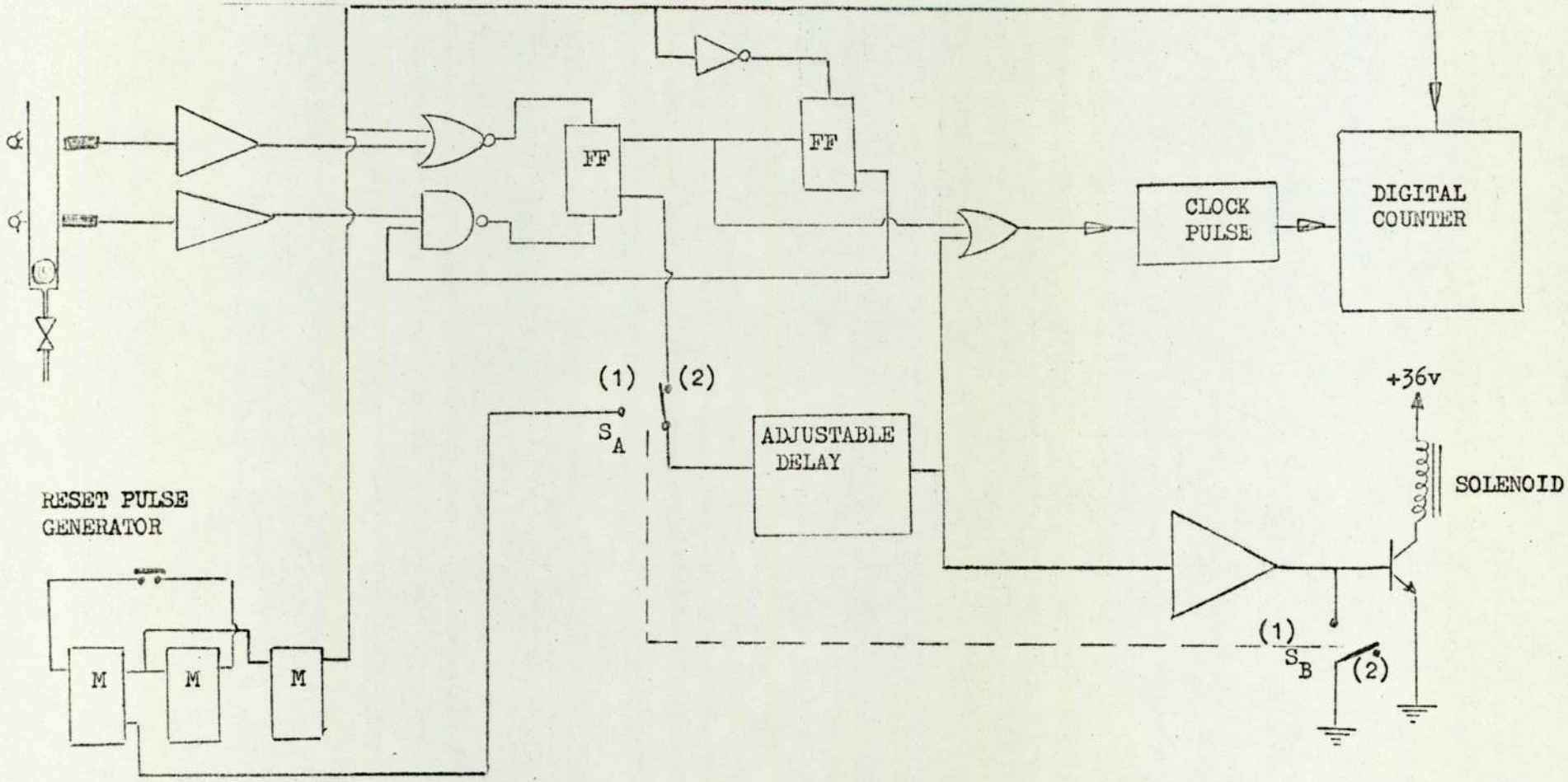


Fig. 8.9. Electronic system to control time interval of combined operational sequence of high speed valve and solenoid. Switches $S_A$ and $S_B$ are in position (1) for adjusting delay pulse, in position (2) for measuring flight time of ball projectile.

# CHAPTER 9

## CONCLUSION

The feasibility of detecting a fast-growing vapour bubble in sodium by an ultrasonic pulse echo method has been explored with the aid of analogue liquids and simulated vapour bubbles, and strong indications of the likelihood of success have been obtained.

No actual experience has been gained with liquid sodium itself since the building and commissioning of the sodium boiler, involving severe technological problems and strict safety requirements, together with an elaborate instrumentation system, have extended beyond the time available for this present project.

Ultrasound frequencies in the region of 5 MHz have been shown to be suitable; these offer high resolution with tolerable bulk attenuation in the liquids considered. Ceramic piezoelectric materials of the lead zirconate titanate type were found to be satisfactory as ultrasonic transducers for this purpose; limitations in their use however were due in part to the problems of coupling to the liquid mass. Direct contact with the liquid metal was not permissible because of a strong corrosive action upon the ceramic and a stainless steel diaphragm was interposed. This forms part of the container wall.

Coupling the ceramic to the diaphragm was achieved by means of a coupling paste, which has an upper limit to its working temperature of 280°C, actually lower than the Curie temperature of the ceramics available (350°C to 490°C). Other forms of bonding, in particular brazing, would have been employed if these ceramics could have withstood the temperatures of the bonding processes. It is likely that, in the reasonably near future, crystalline lithium niobate, which has a Curie temperature in

the region of 1200°C, will be used to advantage; present studies however have revealed extreme difficulty in bonding it to the diaphragm.

Nevertheless, the present problems have been overcome by using a temperature-controlled thermal buffer in the form of a liquid-metal-filled tube between the transducer and the vapour bubble region. The outer end of the tube is sealed by the diaphragm; some care in the choice of diaphragm thickness is needed in order to minimise its effect on echo signal duration.

The temperature span within the buffer tube was from about 280°C at the transducer up to a maximum of 900°C in the pool. It was established that, if the tube was vertical with the cooler regions at the base, the temperature gradient could be stabilised along the direction of the sound beam. This ensured that the medium itself was stable, and permitted transmission of sound without variations in amplitude and transit time.

It was demonstrated that adequate coupling between the transducer and the liquid mass could be obtained when the diaphragm surface was wetted by the liquid. Experiments with Woods metal and tin have shown that, if the liquid temperature is raised to some 50°C above the melting point, wetting of the diaphragm occurs naturally within a reasonable time.

The electronic system, which processes the returning echoes from a multitude of stationary targets within the pool, is able to discriminate between bubble echoes and spurious echoes well enough to track a bubble larger than about 0.5 mm in diameter, and sufficiently rapidly to follow the fast movement of a vapour bubble surface. Analogue experiments with air bubbles in water confirmed that the system would be sufficiently sensitive for the anticipated work with sodium vapour bubbles and would be capable of achieving at least five observations per millisecond.

A bubble nucleation device was constructed for use in the sodium pool. It operates by rapid withdrawal of a protruding rod into a concealing tube; a cavity forms in the liquid at the point of withdrawal, and when the liquid is sufficiently superheated a vapour bubble grows from this point. After a predetermined time, the growing bubble will be collapsed by a pressure ramp applied to the liquid surface. A high-speed valve was designed for this purpose.

Nucleation and collapse are controlled and synchronised by a manually-triggered electronic timing system, and the required growth time can be adjusted at will.

Besides the intended function of the ultrasonic system, three further applications have become apparent during the project.

A strong echo is obtained from the liquid surface, as viewed from underneath, and the transit time of the echo is an accurate measure of the liquid depth. The gas space above the liquid can therefore be directly inferred from this transit time, and predictions of gas-space pressure after the bubble collapse mechanism has operated can be made. This feature has already been incorporated in the pool boiler.

At the onset of bulk boiling, which is likely to occur under conditions of superheat, echoes from fixed targets, such as the nucleation rod, fluctuate in amplitude because of the partial obstruction of the sound beam by the several newly-formed bubbles. The present electronic processor interprets these fluctuations as changes in transit time (this is a function of the discriminator circuit), which the observer then identifies as being due to boiling.

A further benefit of using the buffer tube was that velocities could be measured in regions of high temperature. The transit time difference between staggered targets in the isothermal region defines the sound

velocity. Values were obtained for Woods metal up to 400°C and tin up to 900°C.

High temperature working with Woods metal and, particularly, tin has demonstrated that the transducer and buffer tube can accommodate the conditions likely to be experienced with sodium.

## REFERENCES


1. Fauske, H.K. "Liquid metal boiling in relation to liquid metal fast breeder reactor safety design", Chem. Eng. Prog. Symposium, Series No. 92, Vol. 65, 38, 1969.
2. Kottowski, H.M. and Spiller, K.H. "Sodium superheat boiling" Euratom Report EUR 4842E, 1971.
3. Lord Rayleigh. Phil. Mag. (1917), Vol. 34, 94.
4. Florschuetz, L.W. and Chao, B.T. Journal of Heat Transfer, Vol. 87, 209, 1965.
5. Plesset, K.S. and Zwick, S.A. Journal of Applied Physics, Vol. 23, 95, 1952.
6. Wittke, D.D. and Chao, B.T. Journal of Heat Transfer, 17, 1967.
7. Board, S.J. and Duffy, R.B. "Spherical vapour bubble growth in superheated liquids" Chemical Engineering Science, Vol. 26, 263, 1971.
8. Hawtin, P. et al. "On the collapse of water vapour cavities in a bubble analogue apparatus". Chemical Engineering Science, Vol. 25, 1197, 1970.
9. Judd, A.M. "Analysis of the transient boiling of liquid metals" Brit. J. Applied Physics (J. Phys. D), ser. 2, 2, 1969.
10. Dalle Donne, K. and Ferranti, M.P. Int. J. Heat Mass Transfer, Vol. 18, 477, 1975.
11. Wentz, L.B. et al. "X-ray measurement of void dynamics in boiling liquid metals" Nuclear Applications, Vol. 4, 347, 1968.
12. Chen, J.C. et al. "Probe for detection of voids in liquid metals". The Rev. of Sci. Inst., Vol. 39, No. 11, 1710, 1968.
13. Duffey, R.B. and Hall, R.S. "An ultrasonic technique for measuring the transient movements of a liquid-vapour interface". (J. Phys. E), Series 2, Vol. 2, p. 193, J. Sci. Instrum., 1969

14. Bell, J.F.W. "Ultrasonic thermometry using resonance techniques" 5th Symposium on Temperature, Washington, 1971.

15. Woodward, B. and Stephens, R.W.B. "Some aspects of boiling detection in sodium reactors by means of a mechanical waveguide" Ultrasonics, 1971.

16. Rohrbacher, H. and Bartholomay, R. "Ultrasonic measurement technique in sodium systems" IRE-Report No. 98/73, 1973.

17. Holtz, R.E. and Singer, R.M. "Incipient pool boiling of sodium" Al. Ch. E. J., Vol. 14, No. 4, 654, 1968.

18. Schlectendahl, E.G. Nukleonik 10, 270-274, 1967.

19. Board, S.J. and Kimpton, A.D. "Spherical vapour bubble collapse" Chem. Eng. Sci., Vol. 29, 363, 1974.

20. Bevir, M.K. "The effects of noncondensible gas on bubble collapse" FRS BWG/N (73) 38.

21. Judd, A.M. "The dynamics of sodium vapour bubbles" AEEW-M 792, 1966.

22. Adlam, J.H. and Dullforce, T.A. "Spark-generated steam bubbles" CLM-R134, 1974.

23. Lauterborn, W. "Optical cavitation" Underwater Acoustics Symposium, Birmingham Univeristy, 1974.

24. Ralph, J.C. Private communication, AERE Harwell, Chem. Eng. Division, 1973.

25. Kerr, D.E. "Propagation of short radio waves" Radn. Lab. Ser. 13, 1st edn., Fig. 6.1, p. 453, 1951.

26. Lee Kin Tat and Stephens, R.W.B. "Ultasonic propagation in liquid metals and alloys" Ultrasonics Symposium Proceedings, IEE, 1972.

27. Kim, M.G. et al. "Ultrasonic measurement in liquid alkali metals". J. Acoust. Soc. Amer., Vol. 49, No. 3 (Pt. 2), 1971.

28. Yunker, W.H. "Standard FFTF values for the physical and thermophysical properties of sodium". WHAN-D-3, 1970.

29. ANL-7850. "Chemical Engineering Division research highlights, 1971.

30. McSkimin, H.J. "Velocity of sound in distilled water", J. Acoust. Soc. Amer., Vol. 37, p. 325, 1965.

31. Bevir, M.K., Kazemeini, M.H. and Ralph, J.C. "The growth and collapse of single vapour bubbles in sodium", Paper presented to Liquid Metal Boiling Working Group of Euratom, Risley UK, 1975.

32. Stephens, R.W.B. "Piezoelectricity and the growth of ultrasonics", Journal de Physique, Colloque C6, Vol. 33, 1972.

33. Blitz, J. "Fundamentals of ultrasonics", Butterworths, 1963.

34. Broomfield, G.H. Private communication, AERE Harwell, Metallurgy Division, 1975.

35. Poole, D.H. "An Improved multichannel ultrasonic technique for measuring the transient movements of a liquid vapour interface", CEGB Report RD/B/NI 415, 1969.

36. Beyer, R.T. "Physical ultrasonics", Academic P, 1969.

37. Morse, P.M. and Ingard, K.U. "Theoretical acoustics", 419, 1968.

38. Krautkrämer, J. and Krautkrämer, H. "Ultrasonic testing of materials", pp. 70, 75, 23, 1969.

39. Hislop, J.D. "Flaw size evaluation in immersed ultrasonic testing", Non-destructive Testing, 1969.

40. Haslett, R.W.G. "Physics applied to echo sounding for fish", Ultrasonics, 11-12 (1964); Underwater acoustics, edited by R.W.B.Stephens, 1970.

41. King, R.W.P. and Wu, T.T. "The scattering and diffraction of waves", Oxford University Press, London, 1959.

42. Wells, P.N.T. "Physical principles of ultrasonic diagnosis", pp 80, 97, 1969.

43. Rumsey, J.C.V. "Interpretation of ultrasonic echo amplitude", Brit. J. Appl. Phys., Vol. 12, 25, 1961.

44. Yu, E. Nevskii. "Pulsed excitation of transducers", Soviet Physics Acoustics, Vol. 16, No. 2, 1970.

45. Kossoff, G. "The effects of backing and matching on the performance of piezoelectric ceramic transducers" IEEE Transactions of Sonics and Ultrasonics, Vol. Su -13, No. 1, 1966.

46. Spitzer, L, Jr. "Acoustic properties of gas bubbles in a liquid" Office of Scientific Research and Development National Defense Research Committee, 1943.

47. Gazey, B.K. "A comparison of acoustical and optical imaging systems in turbid waters" Proceedings of the conference on electronic engineering in Ocean Technology, IERE, 1970.

48. Bell, J.F.W. et al. "Digital oscillators" Int. J. Electronics, 1973.

49. Myers, G.H. et al. "A miniature pulser-preamplifier for ultrasonic transducers" Ultrasonics 10, 87, 1972.

50. Kazemeini, M.H. and Ralph, J.C. "Development of an ultrasonic technique for the measurement of single vapour bubble dynamics in sodium", AERE R7840.

51. Heasell, E.L. and Lamb, J. Proc. Phys. Soc. 77, 870, 1960.

52. Gitis, M.B. and Mikhailov, I.G. "Velocity of sound and compressibility of certain liquid metals: Soviet Physics Acoustics, Vol. 11, No. 4, 1966.

53. Clarke, R.H. "Transmission of underwater sound through internal waves and turbulence" Underwater Acoustics Symposium, University of Birmingham, 1974.

54. Newbold, F.J. Private communication, AERE Harwell, Chem. Eng. Division, 1973.

55. Hougen et al. "Dynamics of pneumatic transmission lines" Control Eng., 114, 1963.

56. Krautkrämer, J. "Determination of the size of defects by the ultrasonic impulse echo method", Brit. J. Appl. Phys., Vol 10, 1959.

57. Gooberman, G.L. "Ultrasonics", The English University Press, London, 1968.

58. Lyon, N.L. "Liquid-Metal Handbook", Oak Ridge National Laboratory, 1952

59. Roberts, D.N. "Some physical property measurements of a Bi-Pb-Cd-Sn eutectic in the molten state", AERE R-8350.

60. Bastien, P. "Difficulties in the ultrasonic evaluation of defect size", Non-destructive Testing, pp. 147-151, 1968.